Dynamics of magnetically driven plasma jets: An instability of an instability, gas cloud impacts, shocks, and other deformations

Thesis by

Auna Louise Moser

In Partial Fulfillment of the Requirements

for the Degree of

Doctor of Philosophy

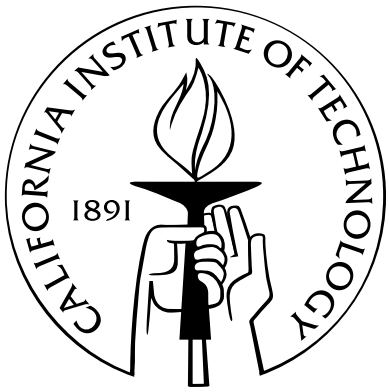

California Institute of Technology

Pasadena, California

2012

(Defended April 10, 2012)

Acknowledgements

I would like to thank my parents Mary and Bill and my sister Alison; for their continual love and support, and for a lifetime of math and science discussions around the dinner table.

I have been fortunate enough to have many outstanding teachers. In addition to my Caltech professors, I would like to thank my high school physics teacher, George Stimson, and my undergraduate mathematics professor, Prof. Steven Agronsky. Both have legions of devoted students, and I'm pleased to count myself among them.

I would like to thank both my candidacy committee—Prof. Roy Gould, Prof. Rob Phillips, Prof. Joann Stock, and Prof. Paul Bellan—and my thesis committee—Prof. Roy Gould, Prof. Lynne Hillenbrand, Prof. Joe Shepherd, and Prof. Paul Bellan—for their insight and valuable feedback.

I have learned so much from all my groupmates, past and present: postdocs Setthivoine You and Shreekrishna Tripathi, and graduate students Steven Pracko, Gunsu Yun, Deepak Kumar, Rory Perkins, Eve Stenson, Mark Kendall, Bao Ha, Vernon Chaplin, Xiang Zhai and Zachary Tobin. I would like to give special thanks to Sett, who first taught me how to run the experiment and is always available for physics discussions and giving advice; Deepak, from whom I learned so much about the experiment and who always made me laugh; and Rory, who is both an excellent experimentalist and theorist and who entertained even my dumbest questions with patience.

Our group is also lucky to have electrical engineer Dave Felt. In addition to designing and building electronics for the lab, Dave always made time, whether it be to explain a design, to help troubleshoot a circuit, or to lend a hand in construction.

Connie Rodriguez, Eleonora Vorobieff and Christy Jenstad kept Applied Physics running smoothly; I suspect that the entire department might actually unravel without their efforts.

The assistance of Mike Gerfen in central engineering services and the accurate and quick work of Joe Haggerty and the GALCIT machine shop most certainly shortened my tenure as a graduate student, for which I am very grateful.

I would also like to thank the lunch crew: Tom, Raviv, Chris, and Matt. Lunches with them were always a highlight of my day, even if some of our ideas were better than others.

My advisor Paul Bellan took me on as an untested graduate student with no training in plasma physics

and a mostly unrelated educational background. I am so appreciative of his support, his patience, and his expertise. His constant encouragement and insight helped me to overcome my lab- and self-created obstacles. I hope that he feels that the gamble he took on me paid off.

And finally I would like to thank Jacob West. I feel so lucky to have found him.

Abstract

The Caltech experiment described here produces plasmas relevant to both astrophysical and fusion energy studies. A disk-shaped set of electrodes mounted on the inside of a meter-scale vacuum chamber provides the energy to break a neutral gas, provided at the electrodes only, down into a plasma. The plasma starts as eight loops, and then self-organizes into a single magnetically driven collimated plasma jet. This thesis explores the dynamic evolution of that plasma jet and how changes made to the jet power source or environment alter the evolution. The most significant finding is the discovery that a series of instabilities can lead to magnetic reconnection. The jet undergoes a first, primary instability, called the kink instability. The exponential growth of kink amplitude provides an acceleration that drives a smaller scale, secondary instability, called the Rayleigh–Taylor instability. The Rayleigh–Taylor instability can drop the diameter of the plasma to a small enough scale to allow magnetic reconnection. A second set of experiments explores the range of collision interactions between the plasma jet and a cloud of neutral gas in its path. A final set of experiments shows the dependence of jet radius on a time-changing current. A new power supply that led to the observation of some of these new dynamics is also described.

Contents

Chapter 1

Background

Plasma is a state of matter in which the constituent atoms are ionized: atoms are stripped of their electrons to form a fluid made up of freely moving ions and electrons. Although it is an oversimplification, we can broadly describe the states of matter according to how the atoms in each state interact. Interaction between atoms is primarily via strong chemical bonds in a solid, primarily via weak chemical bonds in a liquid, primarily via collisions in a gas, and via a combination of collisions and electromagnetic fields in a plasma. Plasmas are prevalent in nature; it is commonplace to estimate that plasma makes up about 99% of all visible matter in the universe [16, 21]. What we consider the normal states of matter—solid, liquid, and gas—are in fact quite exotic.

Because the vast majority of visible matter is in a plasma state, plasma physics underlies the dynamics of most space and astrophysical systems, from stellar dynamos to coronal mass ejections, and from supernovae to relativistic jets. In addition to distant astrophysical plasmas, familiar examples of plasmas include the auroras, lightning, and even fluorescent lights. Plasmas have applications in fusion energy, spacecraft propulsion, laboratory material processing, and the study of astrophysics.

Plasmas are generally characterized by three parameters: particle density n, measured in particles per cubic meter (m^{-3}); magnetic field strength B, measured in Tesla (T); and temperature T, measured in electron-Volts (eV). Figure 1.1 shows the relative densities and temperatures of various plasmas. The plasmas produced in the Caltech experiment have densities of $\sim 10^{21-22}$ m^{-3}, which is dense compared to most other laboratory plasmas, with the exception of those in inertial fusion experiments ($n \sim 10^{31}$ m^{-3}). This is significantly denser than many astrophysical plasmas: the solar corona has a density of $n \sim 10^{15}$ m^{-3} and much of the interstellar medium has a density of $n \sim 10^{7}$ m^{-3}. For comparison, Earth atmosphere has a density of $n \sim 10^{23}$ m^{-3}. The magnetic field strengths are ~ 0.1 T, which is lower than most fusion plasmas and falls in the middle of the vast range of astrophysical field strengths. For reference, the magnetic field strength of the Earth is about 50 μT, while a small rare-earth magnet will usually be about 1 T. The temperatures of our plasmas are 1–2 eV; although 1 eV corresponds to about 11000 K, this is still a modest

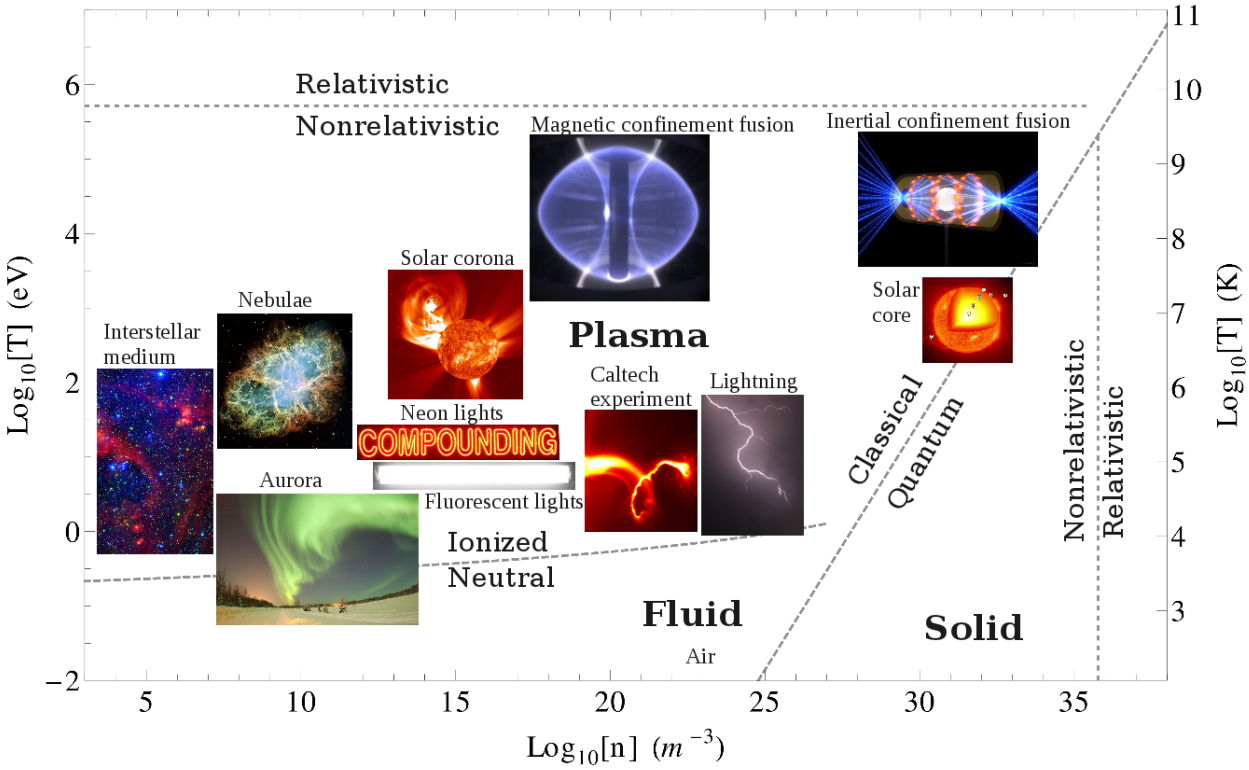

Figure 1.1: Various plasmas and their position in density-temperature space. The dashed lines show various important transitions, calculated for hydrogen: the ionized/neutral boundary at the bottom corresponds to 1% of the hydrogen atoms being ionized (determined using the Saha equation), the classical/quantum boundary at the right indicates the transition to electron degeneracy (where electrons stop behaving like classical particles), the far-right relativistic/nonrelativistic boundary the transition to relativistic degeneracy, and the upper relativistic/nonrelativistic boundary corresponds to $kT = m_e c^2$, but in fact electron-positron pair production happens at lower temperature. Photo credits: aurora, United States Air Force photo by Senior Airman Joshua Strang; star formation in the DR21 region, NASA/JPL-Caltech/A. Marston (ESTEC/ESA); Crab Nebula, NASA/ESA/J. Hester and A. Loll (Arizona State University); solar corona overlaid with solar disk, SOHO (ESA & NASA); MAST tokamak, Culham Centre for Fusion Energy; NIF pellet and hohlraum, Lawrence Livermore National Laboratory; lightning, Sean Waugh NOAA/NSSL

temperature for a plasma, with many space plasmas being 10–100 eV and fusion plasmas being 10^4 eV. This density-temperature information is summarized in Fig. 1.1.

1.1 Overview

Rather than a chronological arrangement, this thesis is organized to allow the reader to read about the most interesting experimental results first and to follow up on the details of the experimental hardware if desired.

This introduction and background chapter provides the motivation and develops the framework and language necessary to discuss the plasma experiments. The next three chapters will present the results from three separate sets of experiments that explore different aspects of the plasma jet evolution. Chapter 2 reports a newly discovered behavior: a large-scale magnetohydrodynamic system reaching the small length scales necessary for magnetic reconnection via a series of instabilities. Chapter 3 presents results of collision experiments in which the plasma jet collides with a cloud of neutral gas, including shocks and magnetic deformation. Chapter 4 shows that straight plasma jets undergo a quasi-two-dimensional "breathing" behavior in response to a fluctuating current amplitude. These experimental results are briefly summarized in Chapter 6.

The addition of a new power supply led to the experimental results in Chapters 2 and 4. Interested readers will find details of the new power supply design and construction in Chapter 5. (Uninterested readers may skip this chapter and proceed, unjudged, to Chapter 6.) Readers especially interested in experimental hardware may also see the appendices: Appendix A details hardware used to produce and diagnose plasmas in the Caltech experiment, Appendix B describes fast ion gauge measurements of neutral gas density, and Appendix C presents the derivation of an exact calibration matrix for the magnetic probe arrays.

1.2 Magnetohydrodynamic (MHD) theory

Because plasma is composed of charged particles, unlike the more familiar neutral particles of solid, liquid, and gas, the particles in a plasma interact not only via collisions, but also via electric and magnetic fields. Electric and magnetic fields affect the motion of charged particles and moving charged particles generate fields; thus, the equations governing these interactions can become very complicated. Three primary models describe plasma dynamics, listed here from most to least detailed: Vlasov theory tracks particle velocity distribution functions, two-fluid theory separates the motion of the positively charged ions and the negatively charged electrons, and magnetohydrodynamics (MHD) treats the plasma as a single electrically conducting fluid. All three models are valuable tools in different plasma regimes. Magnetohydrodynamics describes many plasma phenomena, despite its simplicity, and will be the primary tool used in the following chapters.

For a plasma to be well described by MHD it must be non-relativistic (velocities are much less than

the speed of light), the system length scale must be larger than the Debye length $\lambda_D = \sqrt{\epsilon_0 kT/nq^2}$ (the distance over which a plasma will act to screen a charged particle), and the time scale must be longer than the electron and ion cyclotron periods $\tau_{e(i)} = 2\pi m_{e(i)}/qB$ (the time it takes the charged particles to complete an orbit in a magnetic field).

As its name suggests, magnetohydrodynamics combines Navier-Stokes equations, which describe fluid dynamics, and Maxwell's equations, which describe electromagnetism, to form a closed set of equations. These MHD equations are [5]:

$$\text{Continuity equation:} \qquad \frac{\partial \rho}{\partial t} + \nabla \cdot (\rho \mathbf{v}) = 0 \tag{1.1}$$

$$\text{Equation of motion:} \qquad \rho \frac{d\mathbf{v}}{dt} = \rho \left(\frac{\partial}{\partial t} + \mathbf{v} \cdot \nabla \right) \mathbf{v} = \mathbf{J} \times \mathbf{B} - \nabla \mathbb{P} \tag{1.2}$$

$$\text{Energy equation:} \qquad \frac{P}{\rho^\gamma} = constant \tag{1.3}$$

$$\text{Ohm's law:} \qquad \mathbf{E} + \mathbf{v} \times \mathbf{B} = \eta \mathbf{J} \tag{1.4}$$

$$\text{Faraday's law:} \qquad \nabla \times \mathbf{E} = -\frac{\partial \mathbf{B}}{\partial t} \tag{1.5}$$

$$\text{Ampère's law:} \qquad \nabla \times \mathbf{B} = \mu_0 \mathbf{J}. \tag{1.6}$$

Here the standard $\mathbf{E}$, $\mathbf{B}$, and $\mathbf{J}$ denote the electric field, magnetic field, and current density vectors; ρ, $\mathbf{v}$, and $\mathbb{P}$ denote the plasma mass density, velocity vector, and pressure tensor. The adiabatic index γ depends on the gas and the type of process under consideration; for a monatomic gas undergoing an adiabatic process, $\gamma = 5/3$.

An ideal plasma is a perfect conductor, that is, it has zero electrical resistivity, $\eta = 0$. For a highly conductive plasma, $\eta\mathbf{J}$ is negligible and we can approximate the plasma as ideal. We can then use ideal MHD Ohm's law:

$$\mathbf{E} + \mathbf{v} \times \mathbf{B} = 0. \tag{1.7}$$

One interesting result of ideal MHD is that magnetic flux is "frozen-in" to the frame of the moving plasma. This means that in most cases a moving plasma tends to drag its magnetic field lines along with it.

To see this, we begin with the definition of magnetic flux through a surface $\mathbf{S}(t)$:

$$\Phi(t) = \int_{S(t)} \mathbf{B}(\mathbf{x}, t) \cdot d\mathbf{s}. \tag{1.8}$$

If the surface moves with the plasma, the rate of change of the magnetic flux through the moving surface

is

$$\frac{d\Phi}{dt} = \lim_{\delta t \to 0} \left(\frac{\int_{S(t+\delta t)} \mathbf{B}(\mathbf{x}, t+\delta t) \cdot d\mathbf{s} - \int_{S(t)} \mathbf{B}(\mathbf{x}, t) \cdot d\mathbf{s}}{\delta t} \right).$$

Rather than perform this formal calculation, we will present a more intuitive picture, as given in Kulsrud [31].

The magnetic flux is a function of both the strength of the magnetic field and the area of the surface through which the flux is defined. We can see that the total change in flux will be the sum of two effects: (1) the change in flux due to the magnetic field changing in time, and (2) the change in magnetic flux due to the surface area changing as it moves with the plasma. Let us consider these two changes separately.

First we consider effect (1): the change in flux due to the magnetic field changing in time. From the definition of magnetic flux (Eq. (1.8)) we see that this change will be

$$\frac{\partial \Phi(t)}{\partial t}\Big|_S = \int_S \frac{\partial \mathbf{B}(\mathbf{x}, t)}{\partial t} \cdot d\mathbf{s}. \tag{1.9}$$

The differential can move inside the integrand, because in this step we are assuming that the surface is not changing. Inserting the expression for the electric field in an ideal plasma, $\mathbf{E} = -\mathbf{v} \times \mathbf{B}$ from ideal Ohm's law (Eq. (1.7)), into Faraday's law (Eq. (1.5)) gives an expression for the time-changing magnetic field

$$\frac{\partial \mathbf{B}}{\partial t} = \nabla \times (\mathbf{v} \times \mathbf{B}). \tag{1.10}$$

Substituting Eq. (1.10) into Eq. (1.9) and then using Stokes' theorem expresses the surface integral as a contour integral:

$$\begin{aligned} \frac{\partial \Phi(t)}{\partial t}\Big|_S &= \int_S \frac{\partial \mathbf{B}(\mathbf{x}, t)}{\partial t} \cdot d\mathbf{s} \\ &= \int_S \nabla \times (\mathbf{v} \times \mathbf{B}) \cdot d\mathbf{s} \\ &= \oint_C (\mathbf{v} \times \mathbf{B}) \cdot d\mathbf{l} \end{aligned} \tag{1.11}$$

where C is the boundary of the surface S.

Now we consider effect (2): the change in flux due to the change in the surface as the surface moves with the plasma. To calculate this change, we can imagine the volume created by connecting the surface at time t with the surface at a slightly later time $t + \delta t$. These two surfaces will be connected by a ribbon-like surface with a width equal to the velocity of the moving surface multiplied by the time elapsed, $\mathbf{v}\delta t$ (Fig. 1.2). The change in flux as the surface shifts from its shape and position at time t to its shape and position at time $t + \delta t$ will be the total magnetic flux through this ribbon surface (which has differential area $d\mathbf{A} = \mathbf{v}\delta t \times d\mathbf{l}$)

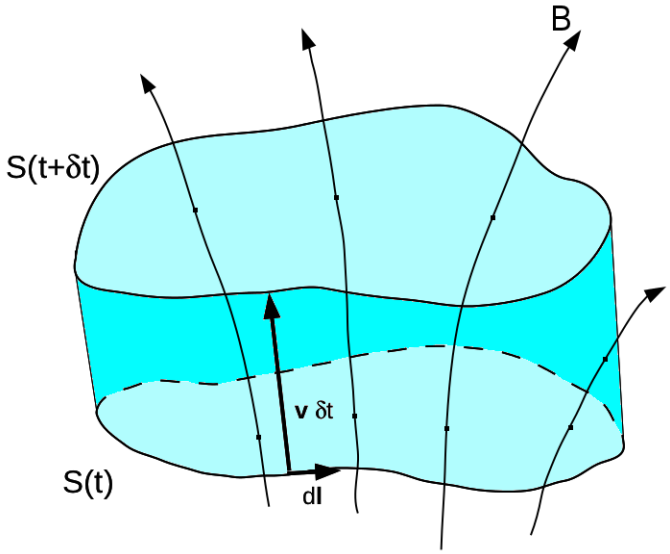

Figure 1.2: A surface traveling with the plasma as seen at time t, $S(t)$, and as seen δt later, $S(t+\delta t)$, are connected by the ribbon-like surface shown in blue. The change in magnetic flux due to the changing area of the surface will be the amount of magnetic flux through the ribbon. In the case shown above, the only magnetic flux piercing the ribbon is the far right magnetic field vector.

divided by δt:

$$\begin{aligned}\frac{\partial\Phi(t)}{\partial t}\Big|_{\mathbf{B}} &= \frac{\oint_C \mathbf{B}\cdot(\mathbf{v}\delta t\times d\mathbf{l})}{\delta t}\\ &= \oint_C (\mathbf{B}\times\mathbf{v})\cdot d\mathbf{l}\\ &= -\oint_C (\mathbf{v}\times\mathbf{B})\cdot d\mathbf{l}.\end{aligned} \tag{1.12}$$

Combining effect (1), Eq. (1.11), and effect (2), Eq. (1.12), we get

$$\frac{d\Phi(t)}{dt} = \frac{\partial\Phi(t)}{\partial t}\Big|_{\mathbf{B}} + \frac{\partial\Phi(t)}{\partial t}\Big|_{S} = \oint_C (\mathbf{v}\times\mathbf{B})\cdot d\mathbf{l} - \oint_C (\mathbf{v}\times\mathbf{B})\cdot d\mathbf{l} = 0. \tag{1.13}$$

The contributions of the two effects cancel, telling us that the flux is constant in the frame of the moving plasma. Hence we say that the magnetic flux is "frozen-in" to the plasma.

1.3 Force-free plasma and applications to fusion and astrophysics

A plasma is said to be "force-free" if no $\mathbf{J}\times\mathbf{B}$ force acts upon it. For it to be true that $\mathbf{J}\times\mathbf{B}=0$, $\mathbf{J}$ and $\mathbf{B}$ must be parallel. This requirement can also be expressed $\mathbf{J}=a\mathbf{B}$, for some value a. Combining this with

Ampère's law, $\nabla \times \mathbf{B} = \mu_0 \mathbf{J}$, gives us the force-free plasma equation:

$$\nabla \times \mathbf{B} = \alpha \mathbf{B}, \tag{1.14}$$

where the value of the constant $\alpha = a\mu_0$ is determined by system parameters.

1.3.1 Woltjer–Taylor relaxation

Woltjer–Taylor relaxation is a process in which a plasma self-organizes, or "relaxes", into a minimum energy state while conserving a quantity called magnetic helicity. The resulting minimum energy state is called a Taylor state. Taylor states are force-free and so are described by the force-free equation, Eq. (1.14) above, with a spatially uniform α determined by system parameters.

A system's total magnetic energy W is defined as the integral of the magnetic energy density over the system volume:

$$W = \int \frac{B^2}{2\mu_0} dV. \tag{1.15}$$

Magnetic energy is conserved in an ideal plasma.

Magnetic helicity gives a measure of the amount of twist, writhe, or linkedness in a volume of plasma. For example: a single, magnetized, untwisted loop of plasma would have zero helicity; two such loops of plasma linked would have the same amount of helicity as a loop of plasma with two twists in it; and plasma in a complicated corkscrew shape would have high helicity. For a magnetic vector potential $\mathbf{A}$ and its associated magnetic field $\mathbf{B} = \nabla \times \mathbf{A}$, magnetic helicity K in a volume is defined as:

$$K = \int \mathbf{A} \cdot \mathbf{B} dV. \tag{1.16}$$

Magnetic helicity is also conserved in an ideal plasma.

While an ideal plasma conserves both magnetic energy and magnetic helicity, a slightly non-ideal plasma dissipates both. Such a plasma can dissipate energy faster than it dissipates helicity, meaning that we can consider the plasma helicity to remain constant on the time scale over which the energy dissipates. The process in which a plasma self-organizes into a minimum energy configuration while maintaining constant helicity is called Woltjer–Taylor relaxation, and the final configuration of the relaxation process is usually called a Taylor state. A given system's final Taylor state is determined by the system's magnetic energy, magnetic helicity, and the boundary conditions.

Woltjer–Taylor relaxation is an example of magnetic self-organization. Self-organization is of fundamental importance in plasma systems. As will be described in the next few sections, the process of Woltjer–Taylor relaxation governs dynamics in systems as seemingly unrelated as small-scale fusion experiments and galaxy-

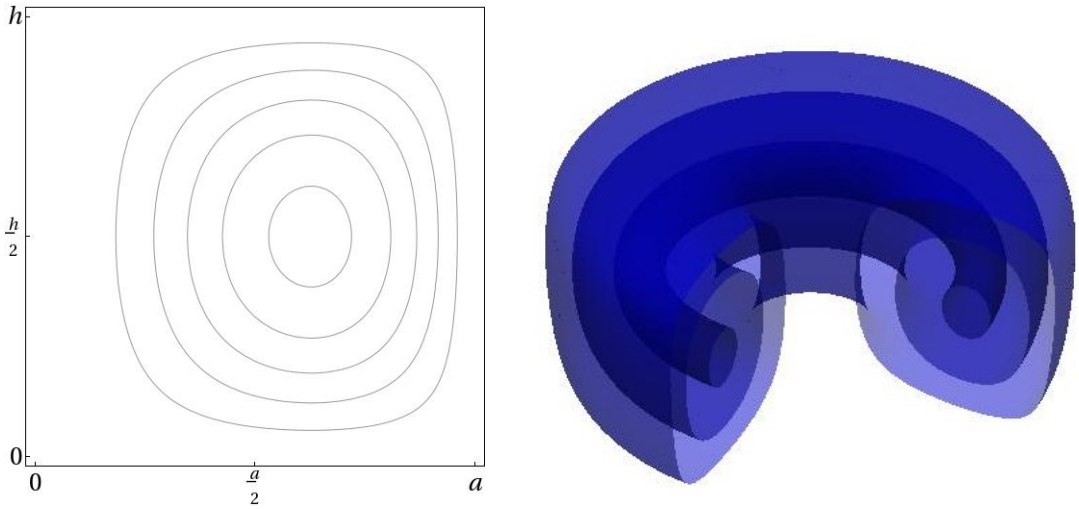

(a) Surfaces of constant poloidal flux (b) Contours of constant poloidal flux

Figure 1.3: Poloidal field structure in spheromaks. (a) Lines show contours of constant poloidal magnetic flux for a spheromak in a cylinder with radius a equal to height h. (b) Surfaces of constant poloidal flux are nested tori.

scale radio-emitting lobes.

1.3.2 Spheromaks

For a simply connected volume (that is, one topologically equivalent to a sphere, rather than a torus) with the boundary condition that no magnetic flux escapes the volume, $\mathbf{B} \cdot d\mathbf{s} = 0$, the Taylor state is called a spheromak.

A spheromak is axisymmetric with cylindrical symmetry. Though the volume is simply connected, important plasma structures within that volume are topologically equivalent to a torus. Taking advantage of the cylindrical symmetry, it is often convenient to define two directions when discussing features: toroidal, which is in the ϕ direction, and poloidal, which combines the r and z directions. A spheromak has a toroidal magnetic field that drops to zero at the boundary and surfaces of constant poloidal magnetic flux which are nested tori, as shown in Fig. 1.3.

Spheromaks may have fusion energy applications. Fusion requires containing hot and dense matter for a long enough time to allow two different types of atoms (usually deuterium and tritium) to combine to form a new atom (helium) and thereby release energy. The two primary plasma containment methods are magnetic confinement and inertial confinement. Magnetic confinement, the most common application of which is the tokamak, uses magnetic fields to create a "magnetic bottle" to hold the fusion plasma. In inertial confinement, imploding matter compresses and heats an inner plasma to fusion-enabling temperature and pressure; the fusion reaction happens quickly and the plasma is so dense that it does not have time to

escape and is effectively contained by its own inertia.

Spheromaks may be valuable as an alternative magnetic confinement method for fusion. A spheromak uses a simply connected chamber and the magnetic geometry requires no external magnetic field coils. This means that a spheromak fusion device could be smaller and simpler (and hence less expensive and easier to build) than many other confinement methods.

One interesting aspect of spheromaks is that, while Woltjer–Taylor relaxation theory specifies the necessary boundary and initial conditions and predicts the final state, the dynamics of spheromak formation remain somewhat mysterious. This makes spheromak formation a productive area of study.

1.3.3 Jets and radio lobes as Taylor relaxed states

Jets and outflows are ubiquitous in astrophysical systems [50], appearing on length scales from less than a light year in young stellar objects (YSO) [48, 53] to millions of light years long in active galactic nuclei (AGN) [62, 8]. The sheer range of scales hints at a general and robust formation and sustainment process [40, 51]. However, the mechanisms that launch, collimate and power these structures are still debated, as are details of their magnetic geometry and interactions with surrounding media.

Polar jets tend to form in accretion disk systems. Astrophysical systems that launch jets have a few common factors: a massive central body, an associated disk of material held in orbit by the central body's gravity, and a nominally poloidal magnetic field [51]. In AGN, the magnetic field threads the disk; in smaller stellar-scale disks, the magnetic field links the central body and the disk (see, for example, Fig. 1.6a). As material in the accretion disk loses angular momentum and falls inwards, much of the material will accrete onto the central body. Some fraction of the disk material that falls in will be ejected in high velocity bipolar jets along the disk's axis of rotation. The nature of the system is such that that the jet velocity must exceed the escape velocity of the central body's gravitational field. This means that jet velocity increases with increasing central body mass, with black hole disk systems launching highly relativistic jets.

Theories of jet formation range from magnetic field-dominated dynamics [44, 41] to pure hydrodynamics [10, 47]. One theory emphasizing the role of the magnetic field uses deformation of the magnetic field to launch the jet [9]. The theory holds that material in the accretion disk differentially rotates, for example the material moves in Kepler orbits around the central body, $v \sim \sqrt{2GM}/r$, so that velocity is different for different values of r. As the disk differentially rotates, magnetic field lines threading the disk and locked to the rotating material twist up, deforming an initially poloidal field into a helical field structure. Centrifugal force launches material along the angled poloidal field lines, away from the disk and along the axis of symmetry. The toroidal component of the magnetic field acts to collimate the jet. The jets may be purely hydrodynamical far from the source, with the distance-diminished magnetic field playing very little role, but most modern theories propose that the magnetic field plays an important role in at least the near-source

Figure 1.4: Centaurus A, an example of a galaxy with disk and associated astrophysical jets. Image is a composite of a visible light background overlaid with X-ray (orange) and submillimeter (blue) data. Image credit: ESO/WFI (Optical); MPIfR/ESO/APEX/A. Weiss et al. (Submillimeter); NASA/CXC/CfA/R.Kraft et al. (X-ray)

section of the jet [46, 43, 19].

Königl and Choudhuri [29] proposed that these jets are an example of a force-free equilibrium, and force-free models continue to hold favor [42, 45]. Others have drawn comparisons between the radio lobes these jets create, jet-hollowed out cavities in the surrounding media that emit in the radio frequency, and the spheromak Taylor relaxed state [64].

1.4 Overview of experiment

The Caltech experiment produces plasmas relevant to both spheromak studies and studies of astrophysical jets. Here, magnetically driven plasma jets precede spheromak formation, and the evolution of these jet structures can give insight into the two systems.

1.4.1 Apparatus

The design of the Caltech experimental apparatus allows for maximum visibility and diagnostic access to the plasma formation region by deforming the cylindrical concentric electrodes typical of spheromak experiments into the simplest possible geometry that satisfies the necessary boundary conditions: a coplanar, concentric

disk and annulus electrodes (see Fig. 1.5). In addition the Caltech experiment has no flux-conserver, that is, no conducting wall bounds the volume that the plasma grows to fill. The plasma is instead bounded by closed poloidal field lines. The experiment generates a spheromak plasma that evolves in a low-background-pressure vacuum chamber, with the wall far away.

The planar electrodes and evolution into vacuum provide diagnostic access to the plasma formation region uncommon in past spheromak experiments; the electrode geometry and minimal wall-effects also make the experiment an effective platform for studying the astrophysical phenomenon described in Section 1.3.3, namely, accretion disk polar jets. As shown in Fig. 1.6, the geometry of the electrodes mimics that of an accretion disk: planar, with a radial electric field and a dipole magnetic field linking the outer disk and its center. Gas inlets in the inner and outer electrode allow the disk to act as the material source, as in accretion disk jets, and the lack of gas backfill and flux conserver means that the laboratory jet forms and propagates out into a region of lower pressure, as in the astrophysical case.

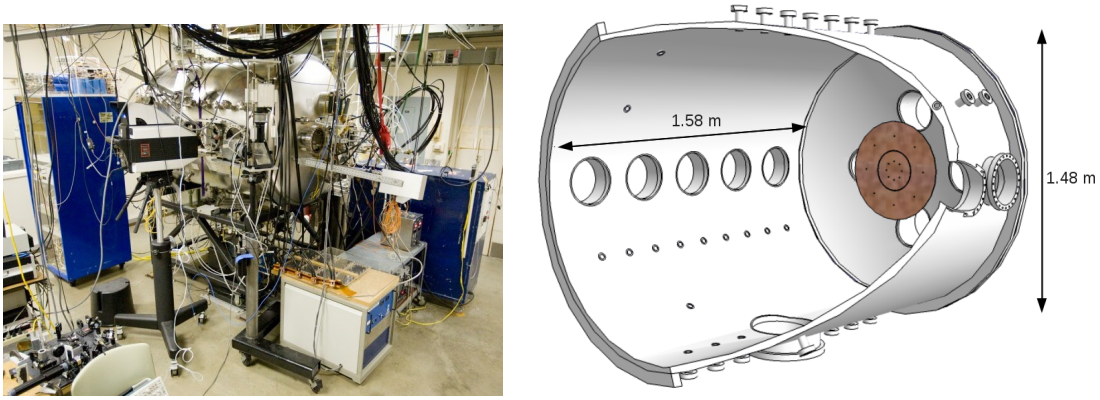

(a) (b)

Figure 1.5: Overview of the Caltech experimental apparatus. (a) Photo of the experimental apparatus, showing the stainless steel vacuum chamber in its natural habitat, with several power supplies and the Imacon fast framing camera. (b) A cut-through diagram of the experimental vacuum chamber, showing a view of the inner cathode and outer electrode mounted on one end dome. Numerous ports and windows allow diagnostic access.

1.4.2 Steps in plasma formation

A typical experiment timeline, with plasma breakdown at $t = 0$, is as follows: $t = -10$ ms, background magnetic field coil power supply fires; $t = -2$ ms, outer electrode fast gas valves fire; $t = -1$ ms, inner electrode fast gas valves fire; $t \sim -2$ to $t \sim -1$ μs, the main power supply applies a voltage across the electrodes; $t = 0$, the gas breaks down into plasma and triggers a round of diagnostics; $t = 0$ to $t = 10$–60 μs, plasma develops and data is acquired. The time between application of high voltage and the time of gas breakdown into plasma can vary by a few microseconds. The light from plasma breakdown triggers

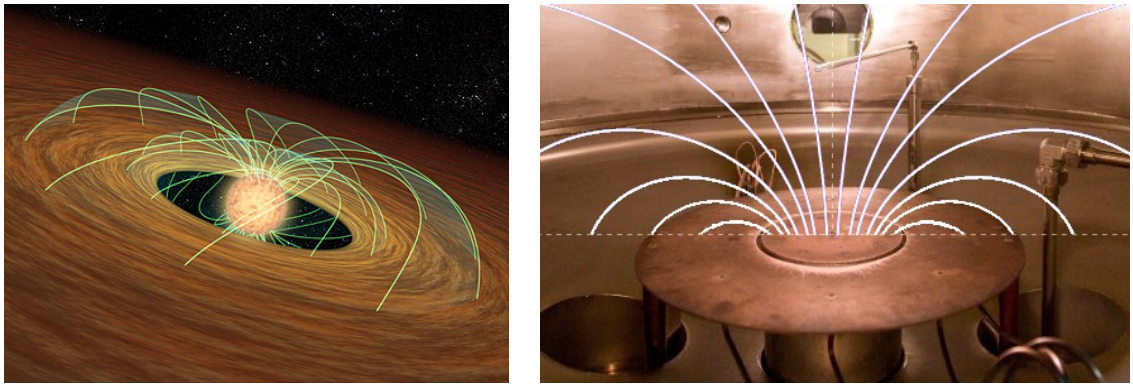

(a) Accretion disk geometry (b) Caltech experiment geometry

Figure 1.6: (a) Artist's conception of magnetic field lines linking a central object and its accretion disk. Image credit: NASA/JPLCaltech/R. Hurt (SSC). (b) The Caltech experiment electrodes, image here rotated for comparison. White lines indicate the background magnetic field, gas inlets provide material. Photo credit: Dave Bullock

diagnostics to avoid problems associated with the uncertainty in time of breakdown.

An overview of the diagnostic equipment locations and geometry is shown in Fig. 1.7. The diagnostic suite includes a fast camera; magnetic probe arrays that each measure the three-dimensional magnetic vector at twenty locations; a 12-channel spectroscopic array that can give ionization, temperature, density, and velocity data; an interferometer that gives density; extreme ultraviolet (EUV) diodes; and a capacitively coupled probe that measures electrostatic fluctuations. The z-axis magnetic probe array and capacitively coupled probe are recent additions, constructed and installed for the purposes of this thesis research. Details of diagnostic equipment are given in Appendix A.

At breakdown, the plasma forms in a radially symmetric arrangement consisting of 8 arches, one for each pair of inner and outer gas inlets, Fig. 1.8. The breakdown path is determined by the gas density according to Paschen breakdown criteria [4], and lies nearly along the imposed background magnetic field lines. The background field is locked into the plasma via flux conservation, as described in Section 1.2. The electrodes are electrically connected by these 8 current-carrying, plasma-filled flux tubes. An ~ 100 kA peak current flows from the outer electrode to the inner electrode; parallel currents on the inner limb of each arch compress the inner portion of the arches into a single central column as the increasing toroidal magnetic pressure between the arches and the electrodes expands the plasma loops. The result is a magnetically driven plasma with a central collimated jet structure. The magnetized plasma jet expands into the chamber at approximately $v_A = B_\phi/\sqrt{\rho\mu_0}$, the poloidal magnetic field Alfvèn velocity, [34] which is ~ 50 km/s for a hydrogen jet.

The current-carrying plasma jet is susceptible to current-driven instabilities. The plasma column undergoes the current-driven ideal MHD kink instability consistent with the Kruskal–Shafranov criterion [28],

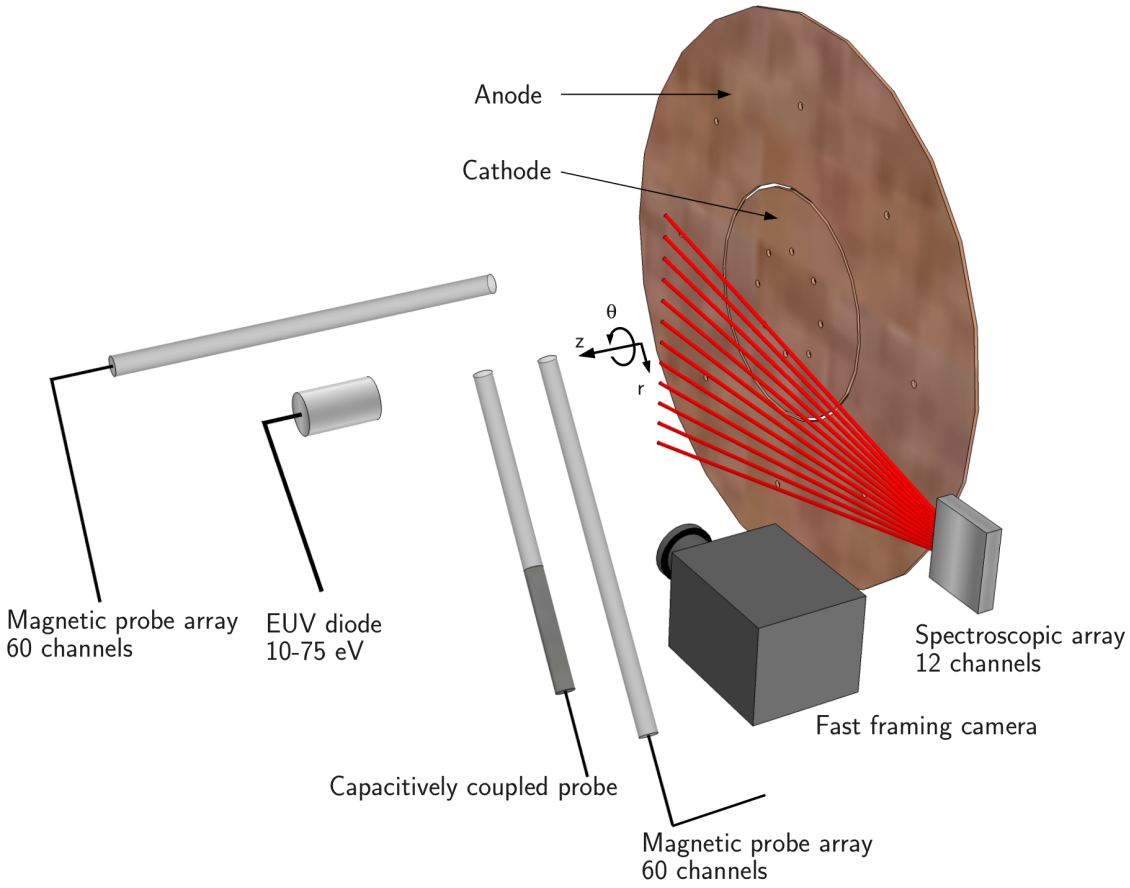

Figure 1.7: An overview of the experiment diagnostics. (Not to scale)

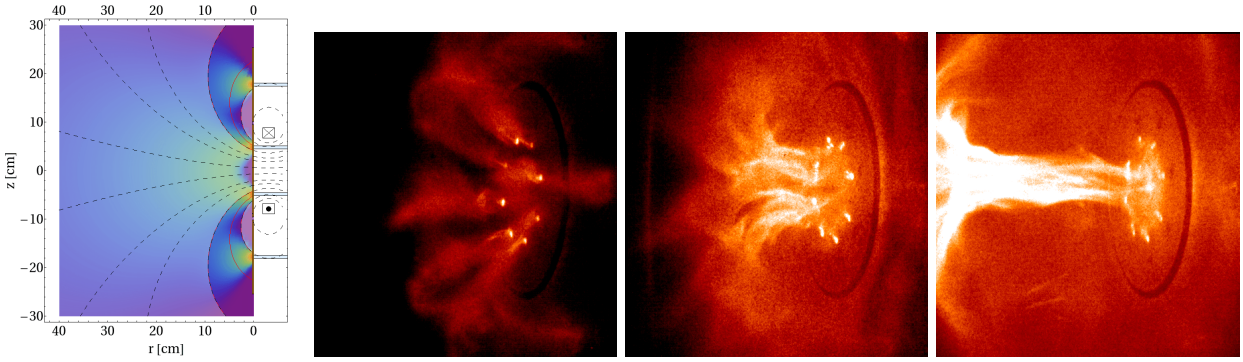

Figure 1.8: Steps in plasma formation. First, neutral gas (in the case shown here, hydrogen) is injected at 16 locations; 8 on the anode and 8 on the cathode. The plot shows a cut-through of the electrodes; the color indicates scaled neutral gas density and dotted lines show the background magnetic field created by the coil mounted behind the electrodes. When high voltage is applied across the electrodes, the neutral gas breaks down into plasma, approximately along the magnetic field lines. Parallel currents in the 8 arched loops draws the inner limb of each loop together in the center, forming a central column or jet. Magnetic pressure drives the jet into the vacuum chamber at approximately 50 km/s.

which states that a column of radius a and length ℓ will be unstable for

$$q(a) = \frac{2\pi a B_z(a)}{\ell B_\phi(a)} < 1. \tag{1.17}$$

The value q is also called the safety factor.

This criterion can be re-expressed in terms of Caltech experimental parameters. Though the value of B_z is not actually constant as a function of r, we can approximate the relationship between the magnetic flux through the inner electrode, Ψ_{ie}, and the value of B_z at the column radius as $\Psi_{ie} \approx \pi a^2 B_z(a)$. If we assume that the entire current measured at the electrodes, I_{ie}, is flowing through the column within radius a, then $B_\phi(a) = \mu_0 I_{ie}/2\pi a$. Together these tell us that the jet will be unstable for

$$\alpha_{ie} > \frac{4\pi}{\ell} \qquad \text{with} \quad \alpha_{ie} = \mu_0 I_{ie}/\Psi_{ie}. \tag{1.18}$$

In our experiment, $\alpha_{ie} = \mu_0 I_{ie}/\Psi_{ie}$ serves as the boundary condition for the plasma that is undergoing relaxation; the value of α_{ie} determines the final relaxed state of the plasma. This α_{ie} is the α of Woltjer–Taylor relaxation evaluated at the experiment boundary, which can be seen by integrating the force-free equation (Eq. (1.14)) over the inner electrode of radius R:

$$\begin{aligned}
\alpha \mathbf{B} &= \nabla \times \mathbf{B} \\
\int_{ie} \alpha \mathbf{B} \cdot d\mathbf{A} &= \int_{ie} \nabla \times \mathbf{B} \cdot d\mathbf{A} \\
\alpha \Psi_{ie} &= \oint_{ie} \mathbf{B} \cdot d\mathbf{l} \\
\alpha \Psi_{ie} &= B_\phi(R) 2\pi R \\
\alpha \Psi_{ie} &= \frac{\mu_0 I_{ie}}{2\pi R} 2\pi R \\
\alpha &= \frac{\mu_0 I_{ie}}{\Psi_{ie}} = \alpha_{ie}.
\end{aligned}$$

As described in Section 1.4.2, the value of α_{ie} determines plasma jet stability in our experiment.

When the plasma reaches a length that satisfies Eq. (1.18), it begins to kink. The formerly straight column becomes helical, with the handedness of the helical structure acting to increase B_z along the central axis [28]; in our current experimental apparatus, this is a right-handed helix.

As we can see from the form of Eq. (1.18), a larger Ψ_{ie}—which corresponds to a higher background poloidal magnetic field—stabilizes the jet against the kink instability. A large Ψ_{ie} yields a straight, stable jet that remains attached to the electrode. For a lower background poloidal magnetic field, the plasma pinches down to a very small radius and breaks off from the electrode. Figure 1.9 shows these three modes in order of increasing background poloidal field strength: detached, kinked, and straight.

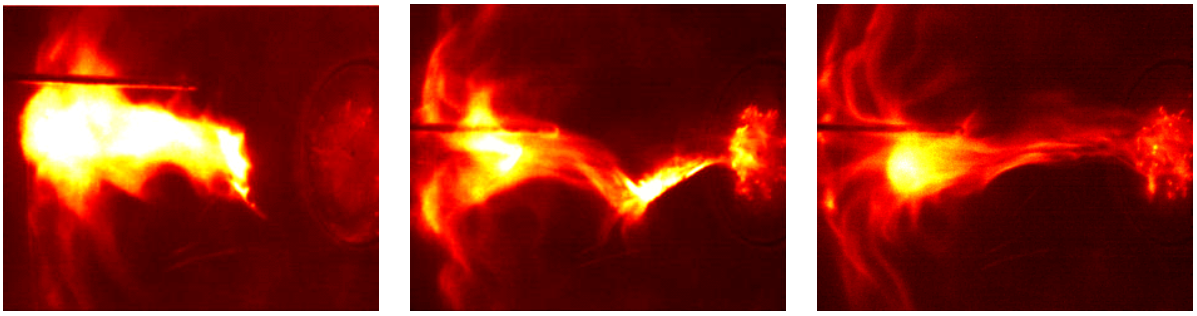

(a) Detached plasma (b) Kinked plasma (c) Straight plasma

Figure 1.9: The three experimental regimes. All 3 images are from hydrogen experiments with the capacitor bank charged to 5 kV, giving a peak current of $I_{peak} \sim 90$ kA. The far-left image shows a detached plasma, $\Psi_{ie} = 0.54$ mWb. The center image shows a kinked plasma, $\Psi_{ie} = 1.62$ mWb. The right image shows a straight plasma, $\Psi_{ie} = 2.17$ mWb.

1.5 Laboratory astrophysics

By their nature, astrophysical measurements are usually remote and often static. We can rarely make direct measurements in the systems of interest and many phenomena evolve on such a long time scale that it is difficult to study their long-term dynamic evolution. By creating astrophysically relevant plasmas in a laboratory environment, we can provide an additional source of insight into astrophysical systems. This can be done both by isolating and studying physical mechanisms of general significance, and also by creating models of specific astrophysical systems in the laboratory making use of scaling laws.

1.5.1 Scaling laws

For a laboratory-scale system to model an astrophysical-scale system, there must be a congruency in the equations governing system evolution. If the dynamical systems are described by scale-independent equations, equations which do not have an explicit dependence on system dimensions, then we can find scaling transformations to relate similar systems. Such scaling transformations are common in physics and engineering. The equations of fluid dynamics are scale-independent, which allows for the familiar examples of wind-tunnel tests of model cars and airplanes before production of full-scale vehicles. The equations of MHD are also scale-independent, allowing us to model the astrophysical systems they describe in the laboratory.

To study an astrophysically relevant MHD system in the laboratory, we must first ensure that our laboratory experiment has the same beginning geometry and boundary conditions as the astrophysical system of interest. Then, the systems will evolve similarly if the astrophysical system variables (subscript a) and the laboratory variables (subscript l) satisfy the transformations [57]:

$$\mathbf{r}_a = c_1\,\mathbf{r}_l \qquad \rho_a = c_2\,\rho_l \qquad P_a = c_3\,P_l$$
$$\mathbf{B}_a = \sqrt{c_3}\,\mathbf{B}_l \qquad \mathbf{v}_a = \sqrt{\frac{c_3}{c_2}}\,\mathbf{v}_l \qquad t_a = c_1\sqrt{\frac{c_2}{c_3}}\,t_l.$$

The scaling laws allow us to compare the evolution of systems with widely differing parameters. As an example, let us consider the Caltech jet experiment and the Imperial College jet experiment. There are a few significant differences between the two experiments. One is that the Caltech experiment jet moves into a region with a density $\sim 10^{-7}$ of the jet density, whereas the Imperial College experiment moves into a background plasma with a density $\sim 10^{-2}$ of the jet density. Another is that the Caltech experiment includes a poloidal background magnetic field, critical for spheromak formation and important in the analogy to the poloidal field threading the accretion disk in an astrophysical system. However, for comparison purposes we can run the Caltech experiment without the background poloidal magnetic field so that the magnetic field in the experiment comes only from the jet current, as in the Imperial College jet experiment.

The Imperial College experiment creates plasma jets using a planar, radially symmetric wire array, and the Caltech experiment creates jets using a set of coplanar, radially symmetric electrodes (for more details of the plasma formation process, see Section 1.4). Both experiments use concentric inner and outer electrodes and both provide plasma material from the disk region; thus, the geometry of the electric field and source of material in the two experiments satisfy the similarity requirement.

The table below gives jet properties for an argon jet on the Caltech experiment, and for a tungsten jet on the Imperial College experiment.

Parameter	Caltech jet	Imperial College jet [37]
r (m)	0.1	0.002
v (km/s)	15	200
n_i (m^{-3})	10^{22}	10^{25}
$Z=n_e/n_i$	1-2	20
T (eV)	1.5	120
ρ (kg/m^3)	6.8×10^{-4}	3.1
P (Pa)	2.4×10^3	1.9×10^8
B (T)	0.2	50

We can use the values in this chart along with the relations above to find the scaling values c_1, c_2, and c_3. This gives:

$$c_1 = \frac{r_{CIT}}{r_{IC}} = 50 \qquad c_2 = \frac{\rho_{CIT}}{\rho_{IC}} = 2.2 \times 10^{-4} \qquad c_3 = \frac{P_{CIT}}{P_{IC}} = 1.3 \times 10^{-5}.$$

The actual ratio of magnetic field strengths is $B_{CIT}/B_{IC} = 4 \times 10^{-3}$, close to the required $\sqrt{c_3} = 3.5 \times 10^{-3}$, and the actual velocity ratio is $v_{CIT}/v_{IC} = 0.075$, which is less than—but on the order of—the required $\sqrt{c_3/c_2} = 0.24$. The two experiments satisfy both the requirement of similar geometry and the scaling laws, so if they also satisfy initial condition requirements, theory predicts that the evolution should give similar structures for $t_{CIT}/t_{IC} = c_1\sqrt{c_3/c_2} = 210$.

Figure 1.10 compares time-series images of an Imperial College jet experiment and a Caltech jet experiment. The magnetic cavity in the Imperial College experiment starts to form at about $t = 220$ ns. The magnetic cavity in the Caltech experiment forms at plasma breakdown, $t = 0$. The cavity in the Caltech experiment has a slightly more inflated shape than that in the Imperial College experiment but is similar enough to allow use of these two instances as our initial states. At $t = 277$ ns, 57 ns after cavity formation, the Imperial College jet has reached a length of 12 mm and starts to pinch off from the electrode. At 9 μs after breakdown, the Caltech experiment jet reaches a length of 16 cm and starts to pinch off from the electrode. This gives a time relation of $t_{CIT}/t_{IC} = (9 \times 10^{-6})/(57 \times 10^{-9}) = 160$, which is fairly close to the value of $t_{CIT}/t_{IC} = 210$ predicted by the scaling laws above. We see that despite densities and temperatures that differ by orders of magnitude, the dynamics of these two systems are similar.

As in the case of these two different-scale laboratory experiments, comparisons can be made between laboratory experiments and astrophysical systems. As mentioned previously, jets form over an enormous range of scales. Many of these jets are relativistic, and so although laboratory experiments may give general insight into their dynamics, a direct model would require relativistic MHD laboratory systems. For smaller-scale jets, like those in young stellar objects (YSO), we can make more direct comparisons. These jets are still large enough to have significant variation in parameters, and for many values we have only a rough estimate. The values in the table below are compiled from multiple papers [23, 25] and are intended to give only a very rough idea of astrophysical scale values. Caltech jet values are for hydrogen jets.

Parameter	Caltech jet	YSO jet
ℓ (m)	0.3	10^{15}
v (km/s)	50	300
T (eV)	1.5	0.7
ρ (kg/m^3)	2×10^{-6}	2×10^{-17}
P (Pa)	160	10^{-9}
B (T)	0.2	5×10^{-7}

Again, we can use these values to find the scaling values c_1, c_2, and c_3. This gives:

$$c_1 = \frac{r_{YSO}}{r_{CIT}} = 5 \times 10^{15} \qquad c_2 = \frac{\rho_{YSO}}{\rho_{CIT}} = 9 \times 10^{-6} \qquad c_3 = \frac{P_{YSO}}{P_{CIT}} = 10^{-12}.$$

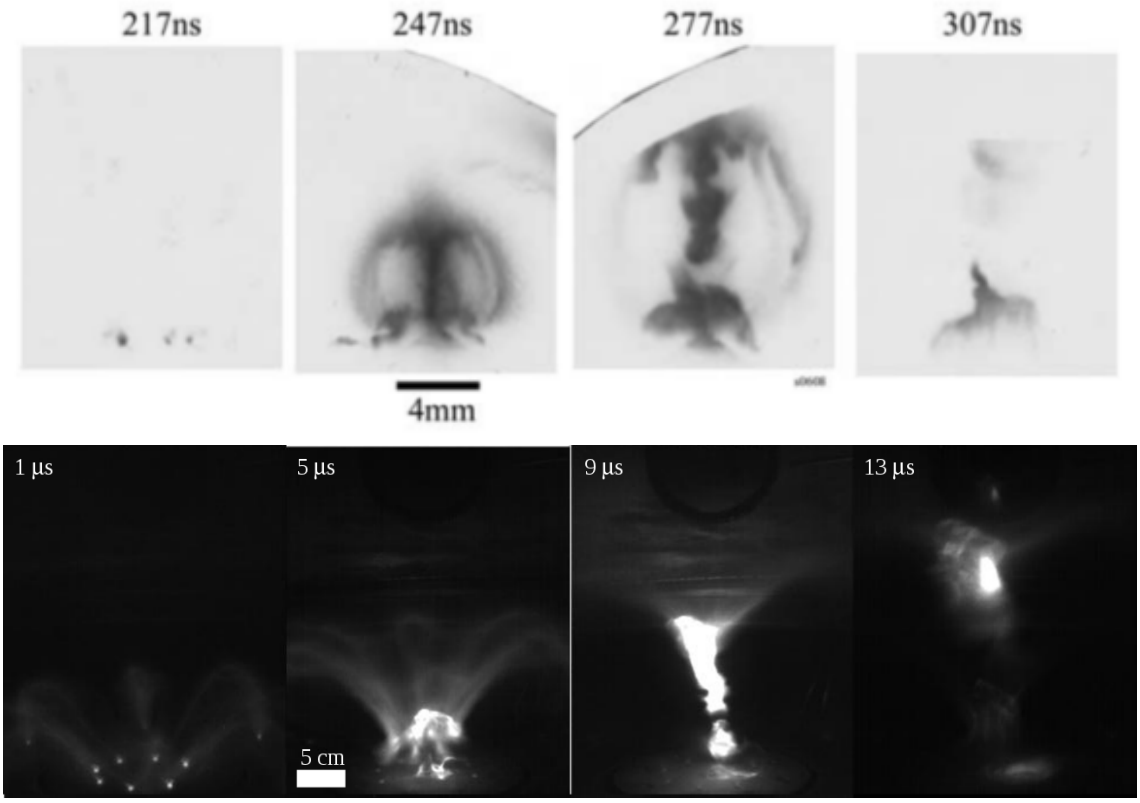

Figure 1.10: Selected images from the Imperial College jet experiment (top) and the Caltech jet experiment (bottom) showing similar evolution. Imperial College images from Lebedev, 2005 [37]

The actual ratio of magnetic field strengths is $B_{YSO}/B_{CIT} = 3 \times 10^{-6}$, close to the required $\sqrt{c_3} = 10^{-6}$, and the actual velocity ratio is $v_{YSO}/v_{CIT} = 6$, which is about an order of magnitude higher than the required $\sqrt{c_3/c_2} = 0.7$. Even so, considering the scale discrepancies in the two systems and the fact that many of the YSO values chosen actually come from a range of several orders of magnitude, these scaling laws are fairly well satisfied. According to the final scaling relationship, $t_{YSO}/t_{CIT} = c_1\sqrt{c_2/c_3} = 7 \times 10^{10}$. This means that dynamics that take place over the course of 10 μs in the laboratory jet correspond to thousands of years of evolution of the YSO systems.

Chapter 2

Instability cascade resulting in magnetic reconnection

Magnetic reconnection is a process whereby magnetic field lines break and then reconnect to form a new topology. This process requires diffusion of field across plasma; a continuing mystery [65] is why observed reconnection rates in both space and laboratory plasmas are typically orders of magnitude faster than can be accounted for using the most obvious diffusion-enabling mechanism: classical electrical resistivity. Current thinking [13, 65] holds that the field diffusion underlying observed magnetic reconnection results from some combination of wave-particle kinetic interactions and Hall term physics that are beyond the scope of ideal MHD. These non-MHD processes become important on the ion skin depth c/ω_{pi} or the ion Larmor radius r_{Li} scales, which are "microscopic" compared to the ideal MHD scale.

Shibata and Tanuma proposed that a macroscopic two-dimensional MHD system could access microscale physics via a sequence of repetitive tearing and thinning of a current sheet into two-dimensional magnetized plasma structures [60]. Relatedly, recent numerical simulations of magnetic reconnection have indicated that magnetic reconnection could involve development of fine structure over a range of scales [15]. One laboratory experiment [18] showed a transition from slow to fast magnetic reconnection when the current channels reached a microscopic scale. If these microscale non-MHD processes are indeed the enabling mechanisms for observed reconnection, the question arises: how can a macroscopic MHD system couple to the required non-MHD microscopic scales?

This chapter describes a cascade of instabilities from a distinct, macroscopic-scale MHD instability to a distinct, microscopic-scale (c/ω_{pi}) instability associated with magnetic reconnection. The observations resolve the fully three-dimensional dynamics and reveal details underlying the impulsive behavior.

2.1 Introduction to magnetic reconnection

In ideal MHD, the magnetic field is frozen-in to the plasma, which means that, as described in Section 1.2, the magnetic field lines do not diffuse across the plasma. It is a fact of nature that plasma structures and their associated magnetic fields must be able to change topology; this topology change requires that magnetic field lines break and then reconnect to form new field lines, a process called magnetic reconnection. Magnetic reconnection requires that the magnetic field lines diffuse across plasma. How can we reconcile this with the MHD model of a frozen-in field?

The microscopic details of magnetic reconnection continue to be a topic of active study. As we understand it, the plasma will continue to be well-described by the equations of ideal MHD except in a very thin layer at the location of the field reconnection. In this small region, the field must be able to diffuse across the plasma. A cartoon of the reconnection process in the case of two merging current loops is shown in Fig. 2.1.

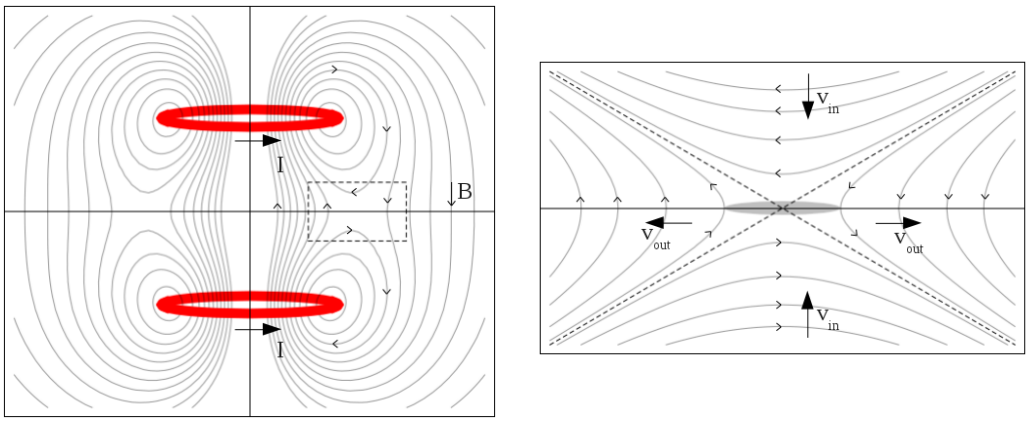

(a) Two current loops and associated fields

(b) Close-up view of region indicated by dashed line box in (a)

Figure 2.1: A cartoon of magnetic reconnection in the case of two merging current loops. (a) The current loops (red) produce magnetic field (grey lines) that must reconnect as the two loops approach each other. The reconnection happens in a very thin layer within the region indicated by the dashed line box. (b) A zoomed-in view of the reconnection region shows the thin layer in which reconnection takes place. This region is called the x-point.

The simplest diffusion-enabling mechanism is electrical resistivity, as the assumption of zero resistivity leads to frozen-in flux. In most laboratory and astrophysical plasmas, however, using the actual plasma resistivity predicts a reconnection rate orders of magnitude lower than the rates observed in these systems. Take the case of a coronal mass ejection (CME), in which material disconnects from the surface of the sun and is hurled into space. Here the resistivity is about $10^{-6}\ \Omega\,\mathrm{m}$, which would lead to predictions of a reconnection time on the order of weeks to months for the 10^6 m scale. However, in observations, the reconnection in CMEs only takes seconds to minutes.

One way to avoid the issue of microscopic physics altogether is to invoke an "anomalous resistivity".

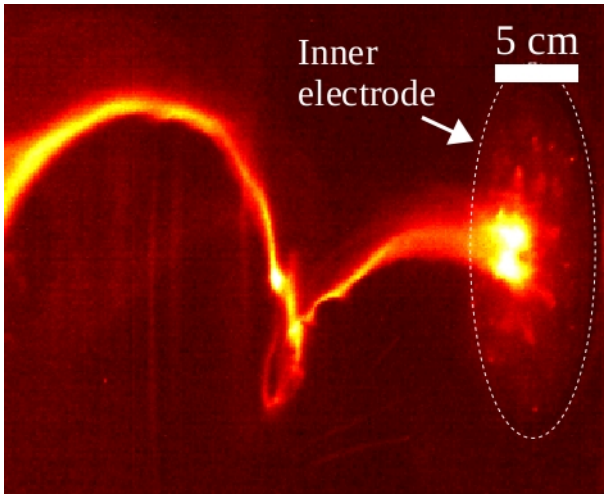

Figure 2.2: An argon plasma jet showing the three-dimensional helical structure of the kink instability. The helix is right-handed, that is, the portion of the filament on the left-hand side of the image is in the foreground, and the portion of the filament connected to the electrode on the right-hand side of the image is in the background. In this case the plasma filament shows the beginning of fine structure associated with the Rayleigh–Taylor instability. Shot #11037; image intensity is logarithmically scaled and false colored.

This method involves using a higher resistivity value than that of the actual resistivity of the plasma, which produces the desired reconnection rates but does not address the question of the small-scale processes responsible for diffusion.

Most modern theories credit a combination of small-scale processes for producing the necessary diffusion. The main processes are wave-particle kinetic interactions (plasma waves coupling to and accelerating particles to high energies) and Hall term physics or two-fluid effects (the decoupling of motion of the electrons and ions rather than electrons and ions behaving as a single conducting fluid as in MHD). Both of these processes are beyond the scope of ideal MHD and become important on the ion skin depth c/ω_{pi} or the ion Larmor radius r_{Li} scales.

2.2 Exponential kink amplitude growth and Rayleigh–Taylor instability onset

As described in Section 1.4.2 of the previous chapter, the magnetically driven jet in the Caltech experiment undergoes a kink instability when $\alpha = \mu_0 I/\Psi > 4\pi/\ell$, consistent with the Kruskal–Shafronov kink instability criterion. A fast camera image showing the three-dimensional structure of the kink instability is shown in Fig. 2.2. The experiments used nitrogen, argon, or hydrogen plasma and in all three the kink amplitude growth rate was observed to have two distinct behaviors: either a linear or an exponential growth (see

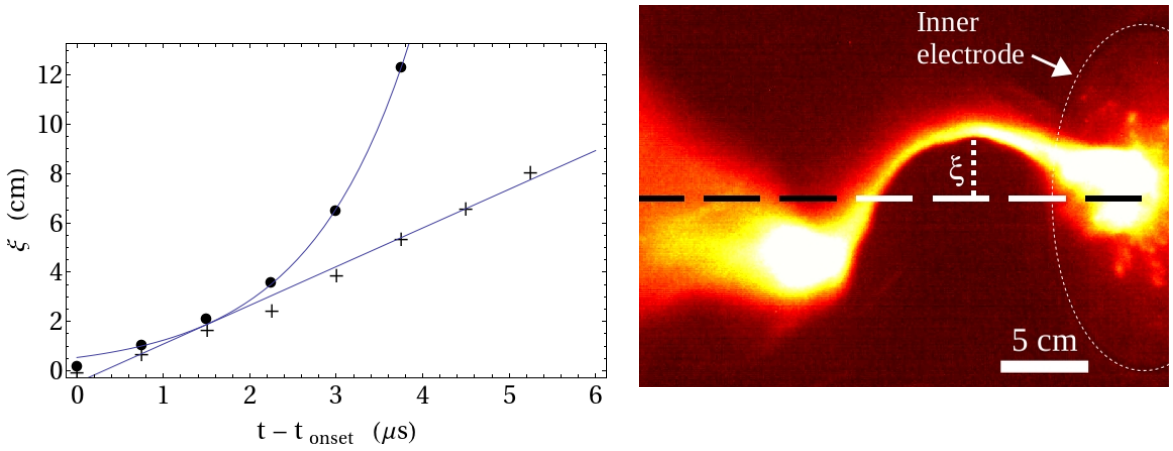

(a) (b)

Figure 2.3: Kink amplitude growth rate. (a) Comparison of exponential kink growth rate and linear kink growth rate as measured from fast camera images. Circles indicate kink amplitude ξ with exponential growth $\sim \exp(\gamma_{kink} t)$ with $\gamma_{kink} = 8.3 \times 10^5$ s^{-1}, shot #10934. Crosses indicate kink amplitude with linear growth $\sim t$, shot #10930. Lines show best fit to data. (b) Example of measurement of amplitude ξ in shot #10934

Fig. 2.3.)

In the exponential growth case (see Fig. 2.4), a segment of the kinked jet quickly transitions to a thin filament, which then becomes very bright while developing a sharp, distinctive periodic fine structure that appears preferentially on the trailing side of the radially outward-accelerating filament. A few microseconds after this thin filament forms, it breaks up.

The growth rate, location, and spatial periodicity of this fine structure are consistent with the Rayleigh–Taylor instability in a magnetized plasma [14]. The Rayleigh–Taylor instability is a well-known pressure-driven instability that develops in a gravitational field at the interface where a heavy fluid with density ρ_2 rests atop a lighter fluid with density ρ_1. In the simplest, non-magnetized case, a disturbance develops at the fluid interface and as the heavy top fluid moves downward, it is replaced with upward-moving lighter fluid (Fig. 2.5). This exchange releases potential energy, as the potential energy of the light fluid due to the gravitational field is less than that of the heavy fluid it replaces. The Rayleigh–Taylor instability is an incompressible instability: the fluids are interchanged without compressing or expanding. The initially small ripple at the interface will grow exponentially in time, forming large "fingers" of interspersed material. The Rayleigh–Taylor instability is common in astrophysical situations, underlying the elongated finger-like structures visible in supernova remnants [26], as seen in Fig. 2.6.

The formation and evolution of Rayleigh–Taylor instability in a magnetized plasma depends on the geometry of the magnetic field relative to the interface between the two fluids. In the case of a magnetic field perpendicular to this surface, the Rayleigh–Taylor proceeds as in the unmagnetized fluid case with no effect from the magnetic field for large wavelength disturbances. For a magnetic field parallel to the fluid

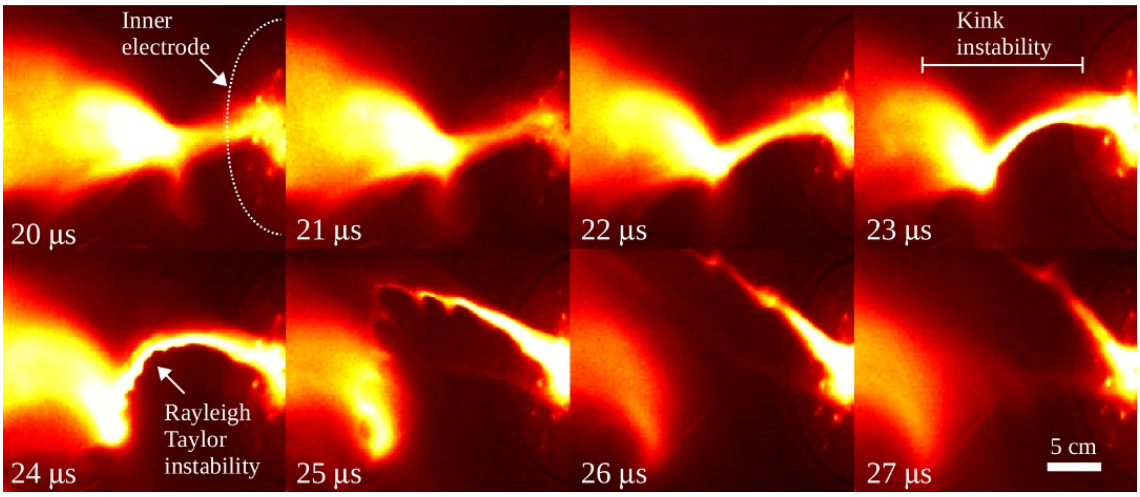

Figure 2.4: Fast camera images of an argon plasma jet undergoing exponentially growing kink instability, developing a Rayleigh–Taylor instability and reconnecting. All images from shot #11225; image intensity is logarithmically scaled and false colored.

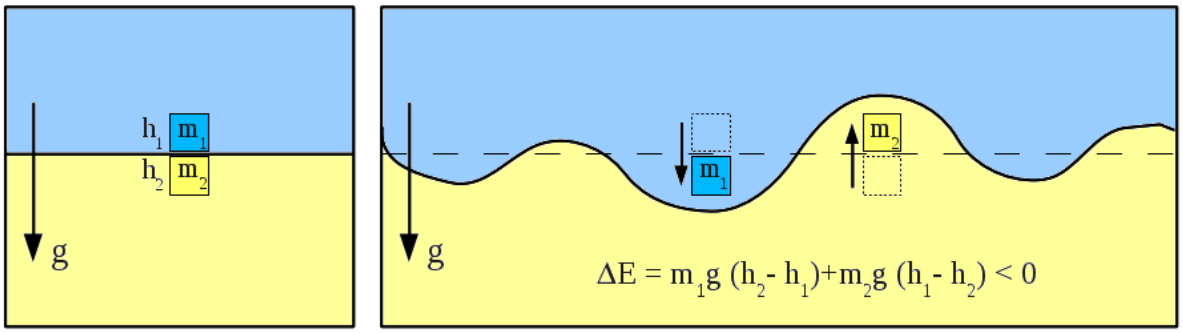

Figure 2.5: Sketch of the Rayleigh–Taylor instability

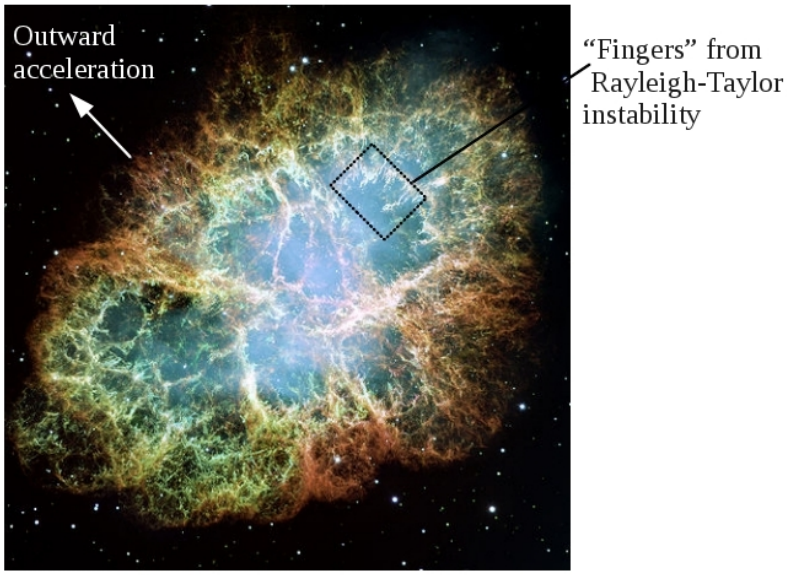

Figure 2.6: The Crab Nebula shows finger-like structures from Rayleigh–Taylor instabilities as the material expands outwards [26]. This is a composite image from the Hubble Space Telescope. Image credit: NASA, ESA, J. Hester and A. Loll (Arizona State University)

interface, the Rayleigh–Taylor instability will simply interchange the magnetic field lines of the two fluids if the disturbance is perpendicular to the field ($\mathbf{k} \cdot \mathbf{B} = 0$, as described below) and will undergo an undulatory instability. If $\mathbf{k} \cdot \mathbf{B} \neq 0$, the disturbance is at an angle with respect to the magnetic field and the tension of the magnetic field lines stabilizes the Rayleigh–Taylor instability.

In our experiment, the acceleration of the exponentially growing kink segment constitutes the effective gravitational acceleration g_{eff}; to an observer in the frame of the accelerating filament at the location of the periodic structure (on the inward side of the outward accelerating filament, i.e., the trailing side), the filament would appear to be a heavy fluid sitting on top of the trailing low-density plasma immediately exterior to the filament. This is also the case for the supernova remnant; the acceleration of the exploding material provides an effective gravity that drives the Rayleigh–Taylor instabilities seen in Fig. 2.6.

The exponential growth rate of a Rayleigh–Taylor instability in a magnetized plasma is [14]

$$\gamma^2 = gk \left(\frac{\rho_2 - \rho_1}{\rho_2 + \rho_1} - \frac{2 \left(\mathbf{k} \cdot \mathbf{B} \right)^2}{\mu_0 \left(\rho_2 + \rho_1 \right) gk} \right). \tag{2.1}$$

The fastest growing mode of the Rayleigh–Taylor instability has $\mathbf{k} \cdot \mathbf{B} = 0$ (where $\mathbf{k}$ is the instability wavevector and $\mathbf{B}$ is the magnetic field vector). We can see this mathematically in Eq. (2.1), where the $\mathbf{k} \cdot \mathbf{B}$ term acts as a stabilizing term in the growth rate. We can also understand it from a physical point of view: the fastest growing mode will be a mode with a geometry such that it does no work in deforming

the magnetic field, and so the wavevector, which points in the direction of the disturbance phase, will be orthogonal to the magnetic field vector. The property $\mathbf{k}\cdot\mathbf{B} = 0$ will be useful again later in the interpretation of the experiment.

If we use our assumption that $\mathbf{k}\cdot\mathbf{B} = 0$ and assume that the plasma density inside the filament is much greater than the density immediately outside the filament, $\rho_2 \gg \rho_1$, then the growth rate for the fastest growing mode in an effective gravity g_{eff} is

$$\gamma \simeq \sqrt{g_{eff}k}, \tag{2.2}$$

where $k = 2\pi/\lambda$ is the mode wavenumber. For the case shown in Fig. 2.4, the measured transverse acceleration of the filament when the periodic fine structure first appears is $g \simeq 4\times10^{10}$ m/s^2. The axial wavelength, as measured from the fast camera images, is $\lambda_z \simeq 2$ cm (see Fig. 2.4), which implies a wavenumber $k \simeq 300$ m$^{-1.}$ These measurements give a calculated Rayleigh–Taylor growth rate $\gamma_{RT} \simeq 3\times10^6$ s^{-1}.

For comparison, the growth rate can be estimated directly from fast camera images (Fig. 2.4). The fine structure amplitude is $\simeq 0.5$ cm when it first appears at $t = 24$ μs and grows to $\simeq 1.5$ cm in 1 μs. This corresponds to an observed growth rate of $\gamma_{RT} \simeq 1\times10^6$ s^{-1}, in good agreement with the calculated growth rate. This agreement between calculated and observed growth rates, as well as the observation that the instability is located on the trailing side of the transversely accelerated filament, supports the conclusion that the fine scale instability is Rayleigh–Taylor.

2.3 Magnetic reconnection

When the thin filament breaks up due to the Rayleigh–Taylor instability, the portion of the jet beyond the breakup region retains its magnetic structure and separates from the remaining jet base (see Fig. 2.7). The kinked column is a magnetized structure that undergoes an obvious topology change; this clearly demonstrates a magnetic reconnection. Furthermore, as discussed below, data from extreme-ultraviolet (EUV) diodes, a capacitively coupled probe, and the magnetic probe array also support the conclusion that magnetic reconnection is occurring.

Photodiodes sensitive to the $10-75$ eV energy range measure a burst of EUV radiation emission coincident with the filament breakup. Figure 2.8 compares data from a plasma shot in which the kink grows linearly, without either developing a Rayleigh–Taylor instability or reconnecting, to a plasma shot in which the kink amplitude grows exponentially, develops a Rayleigh–Taylor instability, and breaks. Both sets of data show a similar peak early on, corresponding to the time when the 8 individual spider leg arches are merging together to form a single central jet. In the linearly growing kink case, emission levels stay low for the remainder of the shot duration; however, in the exponentially growing case, a second strong peak in emission coincides with

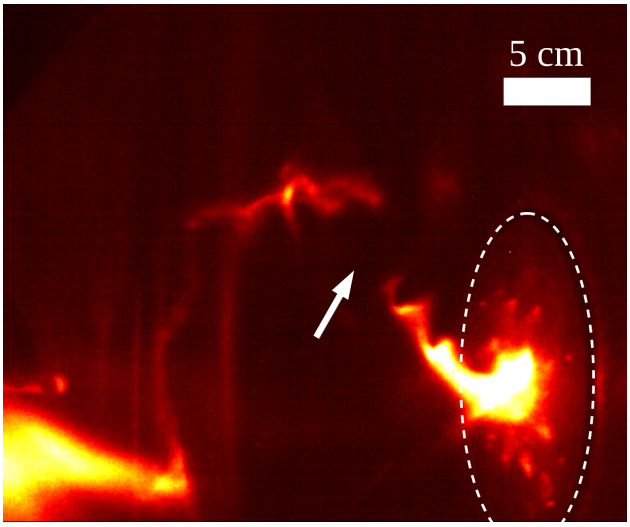

Figure 2.7: An argon plasma jet reconnecting after the kink instability and Rayleigh–Taylor instability. The filament in the center of the frame accelerates upward and continues to move in that direction after the filament snaps; the portion of the filament still connected to the electrode on the right-hand side of the image accelerates downward. The Rayleigh–Taylor instability is on the trailing side of both the upward and downward accelerating portions. Shot #11131; image intensity is logarithmically scaled and false colored.

the filament breakup. High-energy radiation has been shown to be associated with magnetic reconnection in the past, with solar flares producing up to GeV particles and strong X-rays [38].

A capacitively coupled probe placed in the plasma jet between the electrodes and the filament measures an order-of-magnitude increase in emissions coincident with the filament breakup (see Fig. 2.9a). We can demonstrate that the excitations are in the frequency range of whistler waves, which have been shown to be associated with magnetic reconnection [20].

Plasmas support a huge number of different types of waves, broadly broken down into two types: hot and cold plasma waves. Contrary to their names, this division is based not on the temperature of the plasma, but on whether the wave behavior is sensitive to the temperature or is independent of the temperature, respectively. We will mostly concern ourselves with waves in which the wave behavior is independent of temperature. For these so-called "cold" plasma waves, the plasma temperature can be set to zero in calculations without affecting the outcome.

To understand how a wave propagates in a medium, we must understand the dispersion relation of the wave. A dispersion relation relates the wavenumber, k, and the angular frequency, ω, of a wave. A simple example is the dispersion relation for light (an electromagnetic wave) in vacuum: $\omega = ck$, where c is the speed of light. From the dispersion relation of various cold plasma waves we can calculate the group velocity and phase velocity of the wave; the dispersion relation also indicates which frequencies of the wave will and will not propagate, and resonance frequencies at which the wave can couple to particles to transfer energy.

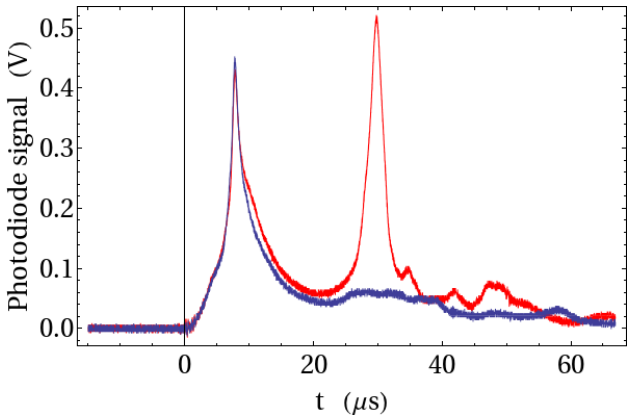

Figure 2.8: Photodiode data show a burst of EUV radiation at the time of reconnection. The red trace, shot #11042, is from an exponentially growing kink that undergoes a Rayleigh–Taylor instability and reconnects. The red trace shows a peak in emission centered at about 30 μs, the corresponding fast camera image shows fine structure at 30 μs and that the plasma has reconnected by 32 μs. The blue trace, shot #11044, is from a linearly growing kink, for comparison.

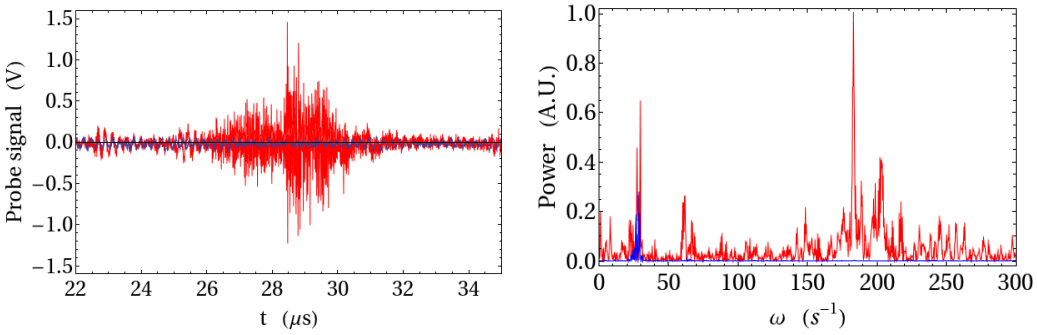

(a) Capactively coupled probe data

(b) Fast Fourier transform of data

Figure 2.9: (a) Capacitively coupled probe data show greatly enhanced excitations at the time of reconnection. The red trace, shot #11214, is from an exponentially growing kink that undergoes a Rayleigh–Taylor instability and reconnects. The signal is strongest at about 29 μs; the corresponding fast camera images show fine structure beginning to form at 28 μs, growing at 29 μs, and that the plasma has reconnected by 30 μs. The blue trace, shot #11201, is from a linearly growing kink, for comparison. (b) A fast Fourier transform (FFT) of the same capacitively coupled probe data shows which frequencies dominate the signal. The red trace shows a peak in the power spectrum centered at about 180 s^{-1}. The argon plasma has a density of 10^{22} m^{-3}, and in shot #11214 a magnetic probe array measured the magnetic field to be $B = 0.25$ T; these values put this frequency of oscillation in the whistler wave regime.

Because the general dispersion relation for cold plasma waves is so complicated, it can be helpful to visualize the propagation in another way. One way to better understand how a wave will propagate is to make a polar plot of wave phase velocity ω/k (or scaled wave phase velocity ω/kc) as a function of θ, where θ is the angle between the wavevector $\mathbf{k}$ and the magnetic field vector $\mathbf{B}$. These plots, called Freidricks diagrams, show the wave normal surface. The advantage of these plots is that they help to visualize the relatively few qualitatively different types of wave normal surfaces, and the limited number of ways that they can be combined.

The space of possible combinations of wave front geometries can be divided into qualitatively different types; this is accomplished in a diagram called the Clemmow–Mullaly–Allis (CMA) diagram, which is shown in Fig. 2.10. Each region of the CMA diagram corresponds to a qualitatively different Freidricks diagram. The CMA diagram uses characteristic frequencies of the plasma in defining the axes. The electron(ion) plasma frequency $\omega_{pe(i)} = \sqrt{n_{e(i)}q^2/\epsilon_0 m_{e(i)}}$ is the frequency at which electrons displaced slightly from the ions will oscillate under the restoring Coulomb force. The electron cyclotron frequency $\omega_{ce(i)} = qB/m_{e(i)}$ is the frequency at which the electrons(ions) orbit the magnetic field lines. The CMA diagram plots $(\omega_{pe}^2+\omega_{pi}^2)/\omega^2$ on the horizontal axis and ω_{ce}^2/ω^2 on the vertical axis. The boundaries between different types of wave normal surfaces divide up the space, and are determined by wave resonance and cutoff values. A resonance is where the wavelength (and the radius of the wave normal surface) goes to zero. A cutoff is where the wave normal surface radius approaches infinity, and corresponds to wave reflection. For a set frequency, moving horizontally on the CMA diagram corresponds to increasing density and moving vertically corresponds to increasing magnetic field strength; each point on the CMA diagram corresponds to a unique density n and magnetic field B.

Because we know the magnetic field strength and density in our plasma, the theory of cold plasma waves in a magnetized plasma allows us to determine the type of wave mode to which our measured frequency corresponds by locating the corresponding region on the CMA diagram. We can take the fast Fourier transform (FFT) of the capacitively coupled probe data shown in Fig. 2.9a to determine the frequency ω. The FFT of the data reveals a peak in the frequency power spectrum at about $f = 30$ MHz or $\omega = 180 \times 10^6$ s^{-1} (Fig. 2.9b).

Combining the measured frequency, $\omega = 180 \times 10^6$ s^{-1}, with a magnetic field strength value of $B = 0.25$ T measured by the magnetic probe array for this same plasma shot, we can bound our position on the ω_{ce}^2/ω^2 axis of the CMA diagram:

$$1 < \underbrace{5.8 \times 10^4}_{\frac{\omega_{ce}^2}{\omega^2}} < \underbrace{5.6 \times 10^9}_{\frac{m_i^2}{m_e^2}}.$$

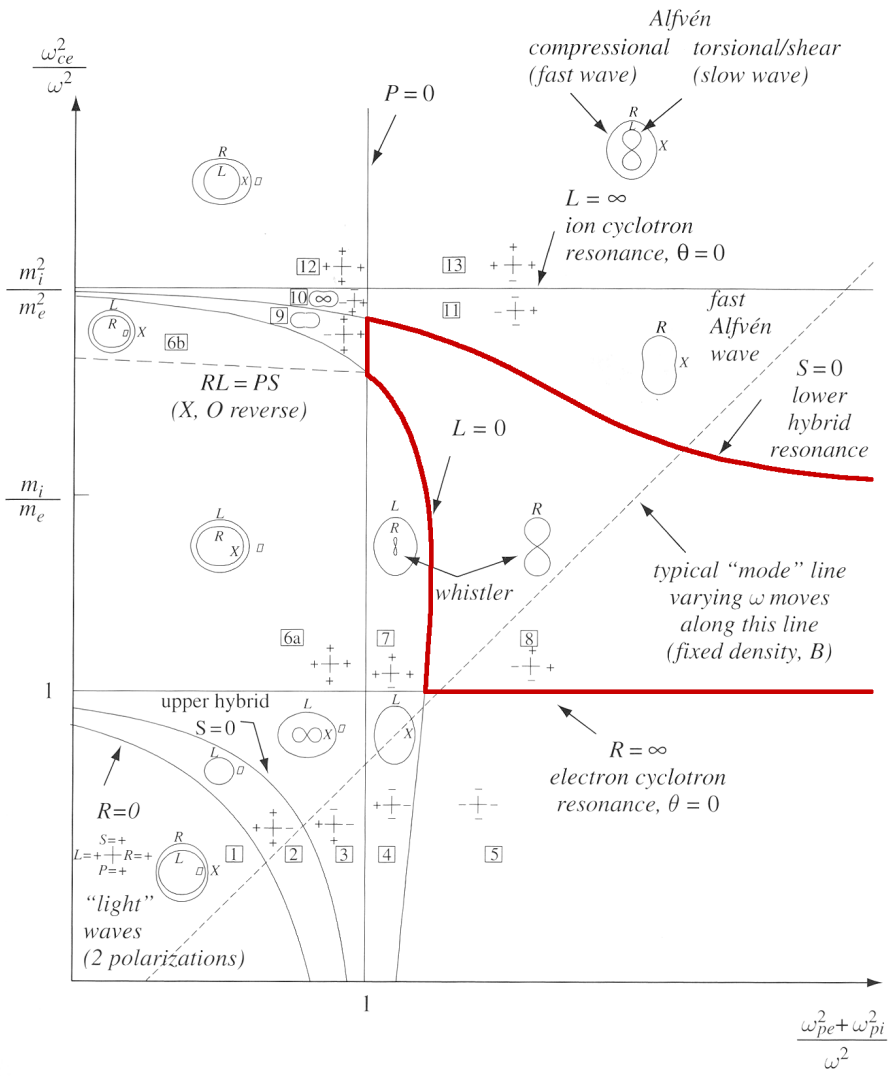

Figure 2.10: The CMA diagram is a visual representation of the wave modes sustained in a cold magnetized plasma. Boundaries between regions correspond to wave cutoff and resonances. A small Freidricks diagrams in each region shows wave front topology for the wave type in that region and the sign of L, R, S, and P are indicated as "+" or "−" for each region. The excitations measured can be placed in the appropriate region by using known values to calculate L, R, S, P. When performed for shot #11214 this method indicates $L < 0$, $R >$, $S > 0$, and $P < 0$. This corresponds to whistler waves, the region shown bounded in red. CMA diagram is taken from Bellan, 2006 [5].

We can also locate our position on the $(\omega_{pe}^2 + \omega_{pi}^2)/\omega^2$ axis:

$$1 < \underbrace{9.8 \times 10^8}_{\frac{\omega_{pe}^2+\omega_{pi}^2}{\omega^2}}.$$

This constrains us to either whistler waves or fast Alfvén waves. In the specific plasma shot shown in Fig. 2.9a and Fig. 2.9b, shot #11214, we can further constrain our location on the CMA diagram by calculating the dielectric tensor values, S, D, and P and their associated values $L = S - D$ and $R = S + D$. These values determine the cutoffs and resonances that bound the regions, and so their calculation will place the measured frequency in a single region of the CMA diagram.

The dielectric tensor $\mathbb{K}$ is

$$\mathbb{K} = \begin{pmatrix} S & -iD & 0 \\ iD & S & 0 \\ 0 & 0 & P \end{pmatrix}$$

with the tensor elements defined as,

$$S = 1 - \sum_{\sigma=i,e} \frac{\omega_{p\sigma}^2}{\omega^2 - \omega_{c\sigma}^2}, \quad D = \sum_{\sigma=i,e} \frac{\omega_{c\sigma}}{\omega} \frac{\omega_{p\sigma}^2}{\omega^2 - \omega_{c\sigma}^2}, \quad P = 1 - \sum_{\sigma=i,e} \frac{\omega_{p\sigma}^2}{\omega^2}.$$

The values S, P, L, and R determine the bounded region of interest on the CMA diagram. For our experimental values, we calculate:

$$\omega_{pi} = \sqrt{\frac{q_i^2 n_i}{\epsilon_0 m_i}} = 2.1 \times 10^{10} \qquad \omega_{ci} = \frac{q_i B}{m_i} = 5.9 \times 10^5$$
$$\omega_{pe} = \sqrt{\frac{q_e^2 n_e}{\epsilon_0 m_e}} = 5.6 \times 10^{12} \qquad \omega_{ce} = \frac{q_e B}{m_e} = -4.4 \times 10^{10}.$$

We can use these values to calculate the tensor elements:

$$S = 1 - \frac{\omega_{pe}^2}{\omega^2 - \omega_{ce}^2} - \frac{\omega_{pi}^2}{\omega^2 - \omega_{ci}^2} = 3.7 \times 10^3, \tag{2.3}$$

$$D = \frac{\omega_{ce}}{\omega} \frac{\omega_{pe}^2}{\omega^2 - \omega_{ce}^2} + \frac{\omega_{ci}}{\omega} \frac{\omega_{pi}^2}{\omega^2 - \omega_{ci}^2} = 4.0 \times 10^6, \tag{2.4}$$

$$P = 1 - \frac{\omega_{pe}^2}{\omega^2} - \frac{\omega_{pi}^2}{\omega^2} = -9.6 \times 10^8. \tag{2.5}$$

This gives us

$$L = S - D = 3.7 \times 10^3 - 4.0 \times 10^6 = -4.0 \times 10^6 \tag{2.6}$$

$$R = S + D = 3.7 \times 10^3 + 4.0 \times 10^6 = 4.0 \times 10^6. \tag{2.7}$$

Equations (2.3), (2.5), (2.6), and (2.7) tell us that $S > 0$, $P < 0$, $L < 0$, and $R > 0$. This bounds the region of the measured excitations on the CMA diagram (Fig. 2.10) and reveals the excitations to be in the whistler wave frequency range.

An x-point, as shown in Fig. 2.1, is the hallmark of magnetic reconnection. In addition to the EUV radiation and whistler waves, an x-point that appears in the magnetic probe data provides further evidence of magnetic reconnection. The x-point appears coincident in time with the formation of fine structure in the plasma column, as shown in Fig. 2.11. When the probe is placed at $z = 15.5$ cm from the electrode surface, the approximate z location of the breaking-apart filament, an x-point is observed at the time of the breaking-off. No such x-point is observed at this location in experiments in which the kink forms but there is no breakup of a fine-structure filament. The x-point in these data involves the assumption of axisymmetry, which is obviously not the case for a kink that is whipping around in three dimensions and then breaking up in one segment. For this reason, the appearance of an x-point alone would not be enough to indicate magnetic reconnection, but it furthers the case for reconnection made by the combination of visible images, EUV, and whistler wave data.

2.4 Non-MHD scale

The MHD-scale kink instability followed by thinning and small-scale Rayleigh–Taylor instability demonstrates a nonlinear cascade from macro- to microscales that leads to magnetic reconnection. We can verify that the reconnecting plasma is indeed in the microscale non-MHD range by recalling that ideal MHD is based on the presumption that $v_d/v_A \ll 1$, where $v_d = J/nq$ is the electron drift velocity associated with a current density J and $v_A = B/\sqrt{\mu_0 n m_i}$ is the Alfvén velocity. When v_d/v_A becomes of order unity, the assumptions underlying ideal MHD fail because kinetic effects (i.e., wave-particle interaction) and Hall terms (i.e., decoupling of electron perpendicular motion from ion perpendicular motion) become important.

This criterion can be expressed as

$$\frac{v_d}{v_A} = \frac{J}{nq}\frac{\sqrt{\mu_0 n m_i}}{B} \ll 1. \tag{2.8}$$

To get an expression for the components of $\mathbf{B}$, we can use our previous assumption that $\mathbf{k} \cdot \mathbf{B} = 0$. Using

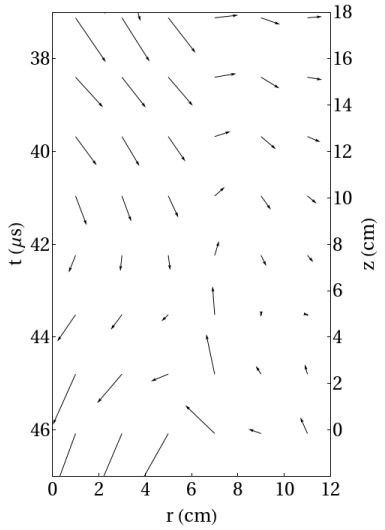

(a) Magnetic vectors in the $r - z$ plane, with reconnection

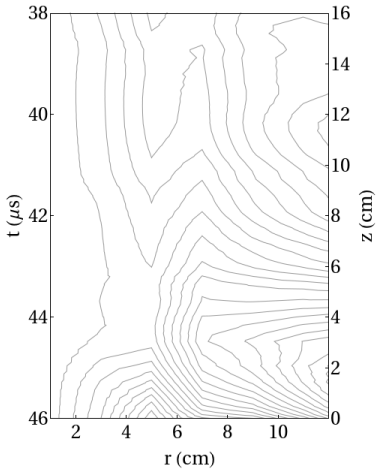

(b) Magnetic flux contours, with reconnection

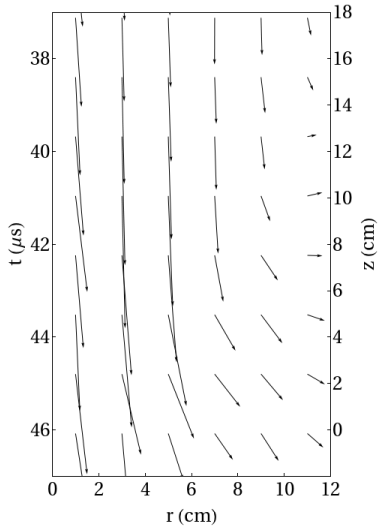

(c) Magnetic vectors in the $r - z$ plane, no reconnection

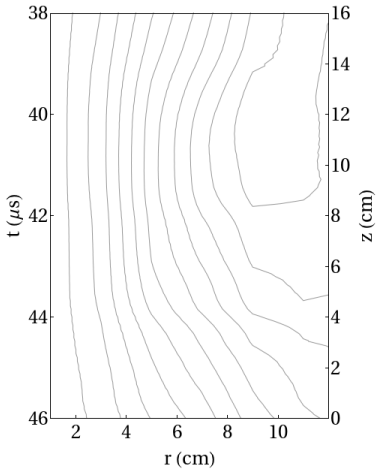

(d) Magnetic flux contours, no reconnection

Figure 2.11: Magnetic probe array data show an x-point in the case of a breaking filament. (a) Magnetic field vectors in the $r - z$ plane as the magnetic structure passes the r-axis magnetic probe array. The horizontal axis shows the radial position (probe channels start at $r = 1$ cm and spaced 2 cm apart). The vertical axis shows time, and the aspect ratio of the plot corresponds approximately to the spatial scale, assuming a velocity of 20 km/s in the z direction. (b) In a system with cylindrical symmetry, a plot of flux contours is equivalent to a plot of magnetic field lines. This plot shows flux contours, but because there is no cylindrical symmetry, this is shown only to highlight the structure visible in (a). (c) and (d) The same plots, for the case with no Rayleigh–Taylor and no magnetic reconnection

cylindrical coordinates we define the wavevector of the disturbance

$$\mathbf{k} = k_\phi \hat{\phi} + k_z \hat{z} = \frac{m}{r}\hat{\phi} + \frac{2\pi}{\lambda_z}\hat{z} \tag{2.9}$$

where m is an integer and we have used symmetry arguments to set $k_r = 0$; similarly, we know that

$$\mathbf{B} = B_\phi \hat{\phi} + B_z \hat{z}. \tag{2.10}$$

This means that

$$\mathbf{k} \cdot \mathbf{B} = \frac{m}{r} B_\phi + \frac{2\pi}{\lambda_z} B_z = 0. \tag{2.11}$$

We see from our images (Fig. 2.4) that the Rayleigh–Taylor disturbance has the asymmetry about the z axis that implies an $m = \pm 1$ mode, and so this gives us

$$B_\phi = \frac{2\pi r}{\lambda_z} B_z. \tag{2.12}$$

We can use Ampére's law to get an equation relating J_z and B_z. We know that the current is in the z direction and so we can use just the z component of Ampére's law

$$\mu_0 J_z = \frac{1}{r}\frac{\partial}{\partial r}(r B_\phi) \tag{2.13}$$

in combination with Eq. (2.12) to obtain

$$\mu_0 J_z = \frac{1}{r}\frac{\partial}{\partial r}\left(\frac{2\pi r^2}{\lambda_z} B_z\right). \tag{2.14}$$

We assume that B_z is constant in the plasma column, and so Eq. (2.14) can be written

$$\mu_0 J_z = \frac{1}{r}\left(\frac{4\pi r}{\lambda_z} B_z\right) \tag{2.15}$$

$$\implies \frac{J_z}{B_z} = \frac{4\pi}{\mu_0 \lambda_z}. \tag{2.16}$$

Because we know that the current is in the z direction, $J = J_z$. From the camera images (Fig. 2.4) we measure the ratio of the filament radius to the Rayleigh–Taylor local axial wavelength is $r/\lambda_z = 0.06$ at $t = 25$ μs and so we know

$$B_\phi = 0.4 B_z \implies B = \sqrt{B_\phi^2 + B_z^2} \approx B_z. \tag{2.17}$$

We can rewrite Eq. (2.8) and then substitute in Eq. (2.16):

$$\begin{aligned}\frac{v_d}{v_A} &= \frac{J_z}{B_z}\frac{\sqrt{\mu_0 n m_i}}{nq} \\ &= \frac{4\pi}{\mu_0 \lambda_z}\frac{\sqrt{\mu_0 n m_i}}{nq} \\ &= \frac{4\pi}{\lambda_z}\frac{\sqrt{m_i \epsilon_0}}{\sqrt{n\mu_0\epsilon_0}q} \\ &= \frac{4\pi}{\lambda_z}\frac{c}{\omega_{pi}}. \end{aligned} \tag{2.18}$$

Stark density measurements of an Ar II line at $\lambda = 373.8$ nm give $n \approx 10^{22}$ m^{-3}. Using this to calculate c/ω_{pi}, and combining with the measured fine structure local axial wavelength $\lambda_z = 2$ cm, gives $v_d/v_A \simeq \mathcal{O}(1)$. Because ideal MHD presumes that $v_d/v_A \ll 1$, this shows that the observed Rayleigh–Taylor unstable filament is decidedly in the non-MHD regime at the time of magnetic reconnection.

Because the original kink instability was in the ideal MHD regime, the observations show a cascade from the ideal, macroscopic kink instability to a non-ideal, microscopic Rayleigh–Taylor instability that is associated with magnetic reconnection.

2.5 Experiments with different plasmas

All images and data presented in this section thus far have been argon plasma experiments, but we see the cascade from an ideal-MHD kink instability to a Rayleigh–Taylor instability in argon plasma, nitrogen plasma, and hydrogen plasma.

In contrast to its behavior in argon and nitrogen, the Rayleigh–Taylor instability in hydrogen fails to break the plasma filament. Although we still observe an exponentially growing kink and subsequent Rayleigh–Taylor instability in hydrogen, the ion skin depth, c/ω_{pi}, is substantially smaller than in argon or nitrogen, and the Rayleigh–Taylor instability fails to erode the plasma filament to a diameter less than this smaller depth, see Fig. 2.12. Thus, the hydrogen plasma diameter has not been reduced to the necessary microscale and no magnetic reconnection takes place. We have not yet determined why this is true. There is no reason that we have seen that would make the hydrogen plasmas unable to reach the microscale. There is sufficient time in the experiment, and the acceleration of the filament is $\sim 10^{10}$ m/s^2, as it is in the argon case.

Reconnection is observed in the nominal parameter regime of these experiments only when preceded by the Rayleigh–Taylor instability; this implies that the Rayleigh–Taylor instability is necessary for the observed reconnection to occur. However, the comparison between argon, nitrogen, and hydrogen plasmas shows that the mere existence of the Rayleigh–Taylor instability is not sufficient for reconnection; the Rayleigh–Taylor instability must become large enough to erode the filament diameter to less than the ion skin depth for

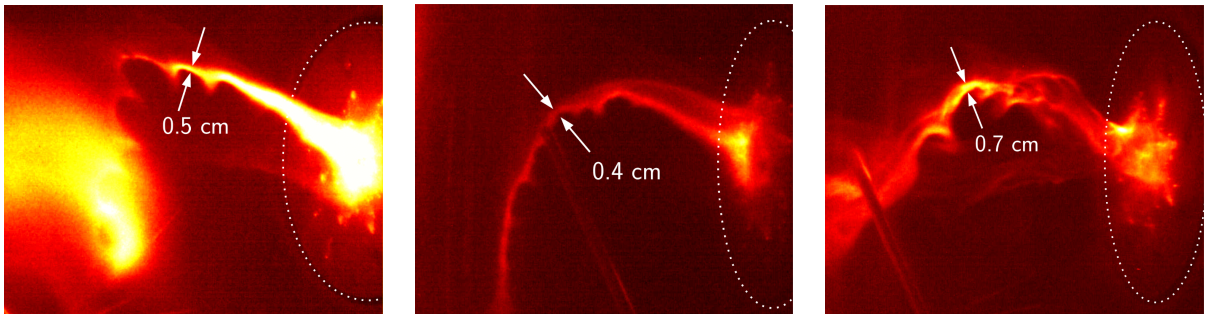

(a) Argon plasma (b) Nitrogen plasma (c) Hydrogen plasma

Figure 2.12: Examples of Rayleigh–Taylor fine structure on top of kink-unstable plasma jets. In the case of (a) argon and (b) nitrogen plasma jets, the Rayleigh–Taylor erodes the filament to the ion skin depth or below it. The ion skin depth is 1 cm in the argon plasma and 0.5 cm in nitrogen plasma. In the case of (c) hydrogen, the diameter of the filament does not reach the ion skin depth, 0.2 cm, and we do not observe magnetic reconnection.

magnetic reconnection to occur.

2.6 Relevance to solar loops

The essential components of this mechanism have been separately observed in nature. For example, in the solar corona current-carrying magnetic flux tubes confining plasma with density higher than ambient are common, kinking of such flux tubes is also common [63, 67], and Rayleigh–Taylor instabilities have been observed [7].

Given that we observe this mechanism in a range of laboratory experiments, we think it quite plausible that it will also occur in astrophysical systems with appropriate physical parameters. As a possible example, one solar observation [39] reported a $\sim 10^3$ m/s^2 lateral acceleration of a plasma-filled flux tube. Assuming such acceleration is typical, for a 10 Mm wide solar loop, a 0.4 Mm axial wavelength Rayleigh–Taylor disturbance with initial amplitude of 500 m would grow exponentially to the 10 Mm loop width in about 1 minute and so erode the current channel to a microscopic scale. Because the assumed 0.4 Mm instability wavelength is at the margin of existing resolution capabilities, measurements that simultaneously resolve the widely separated macro- and microscales would be challenging.

Chapter 3

Collision experiments

In astrophysical systems over a wide range of scales, collimated plasma jets travel at high velocity and collide with the surrounding medium. To better understand this interaction, we designed a laboratory experiment that places a localized cloud of neutral gas directly in the path of a plasma jet (Fig. 3.1) and studied the evolution of the jet-cloud system. Upon collision with the neutral cloud, the magnetized jet slows and deforms and the initially neutral cloud is ionized. The interaction is studied with several diagnostics: the fast framing camera (with and without optical filters), both the r-axis and z-axis magnetic probe arrays, and the 12-channel spectrometer. Collision experiments were performed with various combinations of hydrogen, argon, and nitrogen. The nature of the interaction depends on the plasma jet species and the neutral cloud species. There are two qualitatively different types of interaction presented in this chapter: Section 3.1 describes the evolution of a hydrogen plasma jet colliding with an argon or nitrogen neutral cloud, and Section 3.2 describes the evolution of a nitrogen or argon jet colliding with a hydrogen neutral cloud.

3.1 Density increase and magnetic field amplification in hydrogen jets

Hydrogen plasma jets in our experiment travel at ~ 50 km/s. Collision experiments in which a hydrogen plasma jet hits an initially neutral cloud of either argon or nitrogen show that when the plasma jet hits the neutral cloud the jet slows significantly and deforms. As the hydrogen jet front slows and thickens, the strength of the embedded magnetic field increases with increasing plasma density. The collision leaves the argon or nitrogen cloud completely ionized. Most of the measurements in this section are from argon neutral cloud experiments; argon and nitrogen neutral cloud experiments are qualitatively similar.

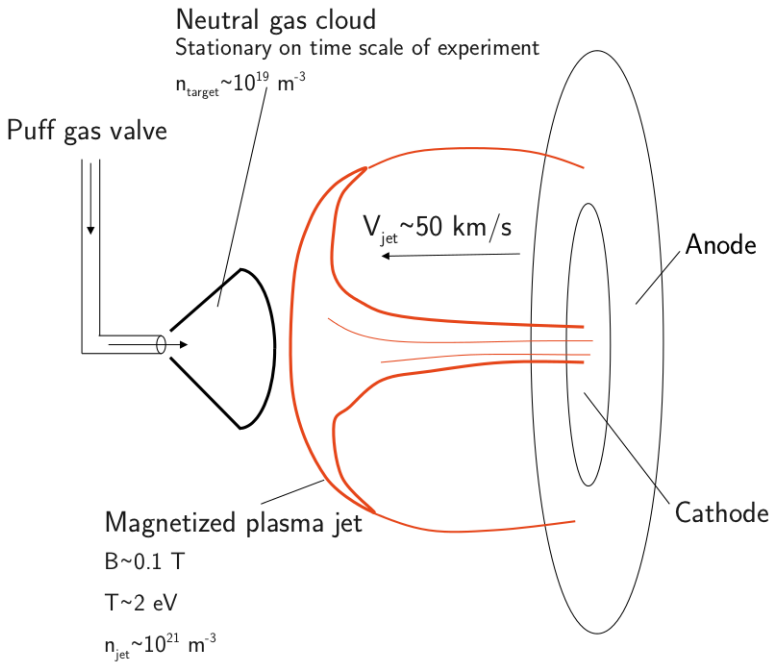

Figure 3.1: Simplified schematic of collision experiment geometry

3.1.1 Visible interaction

The interaction between the hydrogen plasma and the argon neutral cloud is clear in fast camera images of the collision (Fig. 3.2). The images indicate that the interaction between the plasma jet and neutral cloud starts at about 6 μs after plasma breakdown, when the plasma jet has reached a length of 25 cm. The jet slows significantly, losing about 75% of its velocity. The jet front visibly thickens as the plasma collides with the neutral cloud. As shown in Fig. 3.2, the plasma appears to pile up as it collides with the neutral gas cloud.

3.1.2 Spectroscopic measurements

The 12-channel spectroscopic array can be used to study the interaction region in detail. The spectroscopic lines of sight are aligned along the z-axis so that they span $z = 19$ cm to $z = 41$ cm, with the primary collision region from $z = 25$ cm to $z = 35$ cm. The spectroscopic measurement window is centered on the Balmer series H-β line at 486.13 nm and includes two argon ion (Ar II) lines at 484.78 and 487.99 nm (Fig. 3.3).

The H-β line is significantly wider due to a process known as Stark broadening. Stark broadening indicates electron density; the greater the broadening, the higher the density [66]. In Fig. 3.3, the Stark broadening indicates an electron density $n_e = 7.5 \times 10^{21}$. The full linear array of spectroscopic measurements is shown in Fig. 3.4. The data show H-β Stark broadening increasing with z, peaking in a region corresponding to

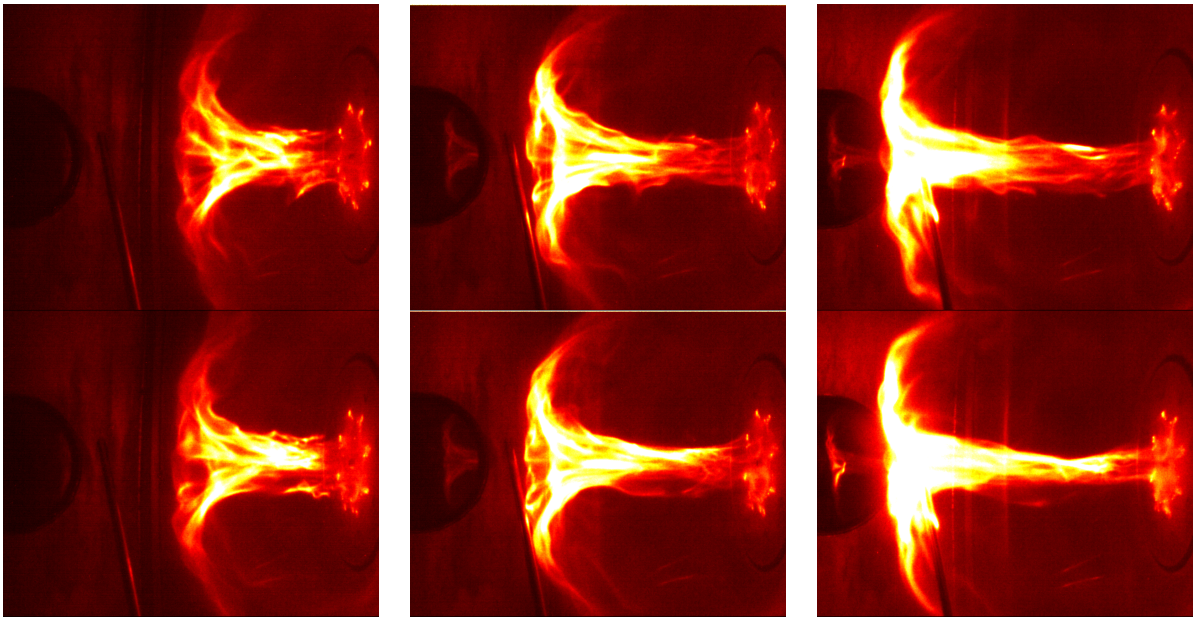

(a) $t = 4$ μs (b) $t = 5$ μs (c) $t = 6$ μs

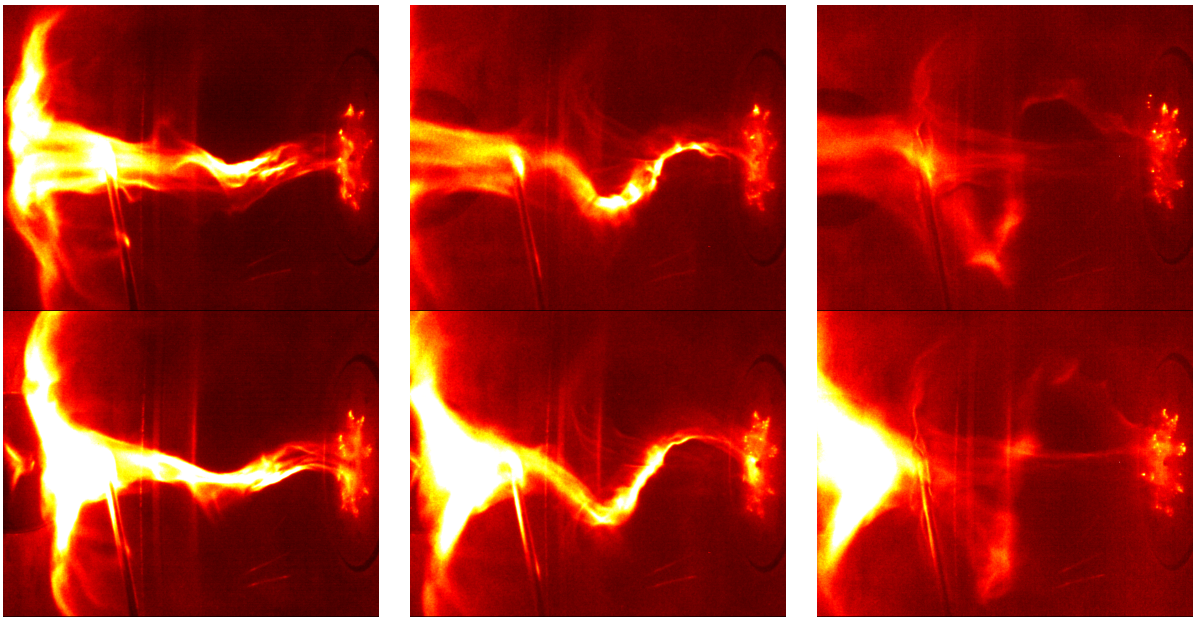

(d) $t = 7$ μs (e) $t = 8$ μs (f) $t = 9$ μs

Figure 3.2: Visible light images from the fast camera show the plasma jet front slowing as it interacts with the argon neutral cloud. Top image in each set is with no neutral cloud, bottom image is with an argon neutral cloud. First images show the jet fully formed but before interaction with the neutral cloud. Interaction is visible starting in the third set of images. Final images show the jet front slowed and thickened. The linear feature visible at the bottom of the frame is the r-axis magnetic probe array. Image is false-colored and intensity is scaled logarithmically for display clarity.

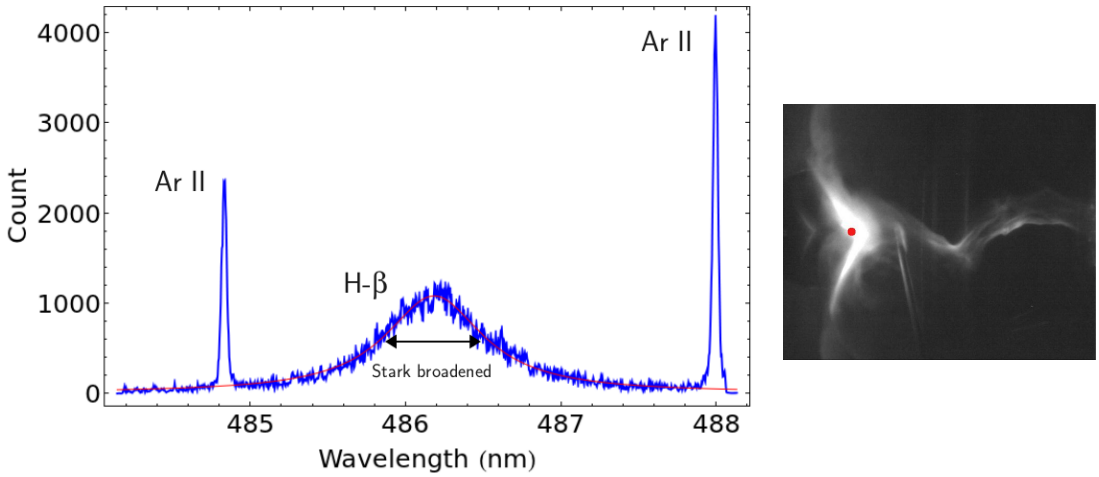

Figure 3.3: Spectroscopic data show Stark broadening of H-β lines and ionization of argon. Data are taken from a single channel of the 12-channel array, whose position is indicated by a red dot in the right-hand image. Measurement is centered on the H-β line at 486.13 nm. The window includes two Ar II lines at 484.78 and 487.99 nm.

the appearance of the thick front in the images and dropping off in the neutral gas region. A plot of the electron density as a function of z is shown in Fig. 3.5. These data are consistent with a picture of the plasma jet striking the initially neutral argon cloud, ionizing the argon, then slowing and piling up in the interaction region. Because the hydrogen plasma piles up when it hits the argon neutral gas, the hydrogen plasma maximum density is at lower z than the argon neutral gas. Just past the peaking of the jet density as measured by Stark broadening is the maximum intensity of the Ar II lines.

3.1.3 Magnetic measurements

Ideal MHD theory predicts that flux is frozen-in to the plasma; a magnetized plasma will act to keep magnetic flux invariant in the frame of the moving plasma (see discussion in Section 1.2). Ideal MHD describes a plasma with a negligibly small resistivity, that is, a plasma with a large magnetic Reynolds number $R_M = \mu_0 L v/\eta$, where L is the plasma length, v the velocity, and η the plasma resistivity. The thermal velocity for $T = 2$ eV and $n \sim 10^{21}$ m^{-3} gives an ion-electron collision frequency for the hydrogen plasma jet of 7×10^9 s^{-1} and an electron mean free path of $l_{mfp} \sim 10^{-2}$ cm. The plasma resistivity is $\eta \sim 3 \times 10^{-4}$ Ωm; with a characteristic length of 25 cm and velocity of 50 km/s,, this gives a magnetic Reynolds number $R_M \sim 50$. Because $R_M \gg 1$, the hydrogen jet can be treated as an ideal MHD plasma. Thus, we would expect an increase in magnetic field to accompany an increase in plasma density. Magnetic measurements confirm that the magnetic field increases in the region of increased plasma density, consistent with this prediction.

The first magnetic measurements were made with the r-axis magnetic probe array (MPA). The r-axis MPA can be moved in z to measure the field as a function of r at different z locations. We measured

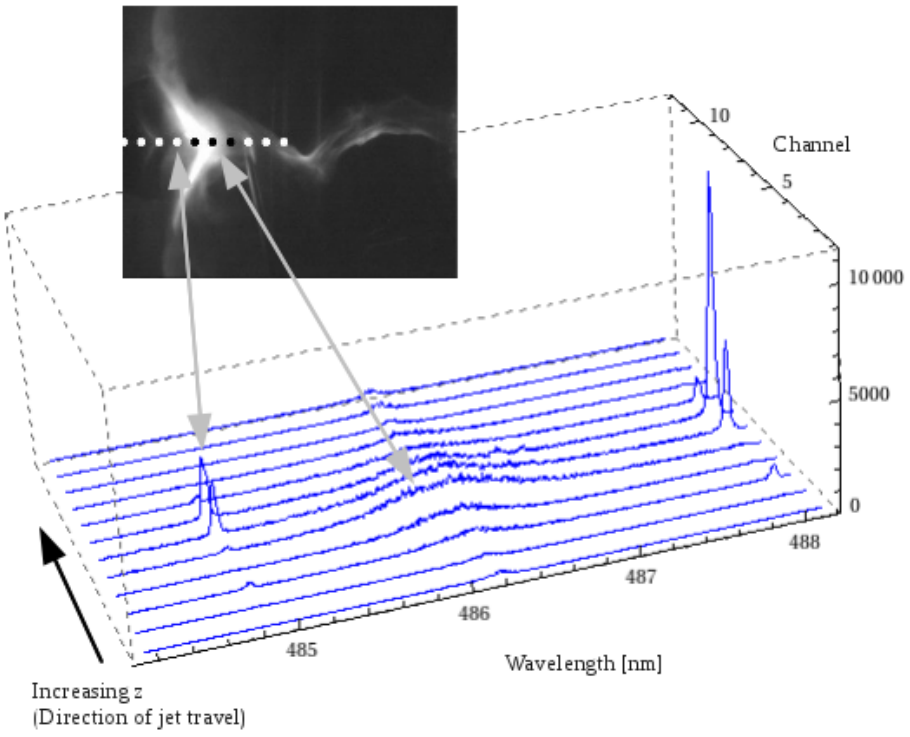

Figure 3.4: Spectroscopic data show Stark broadening of H-β lines and ionization of argon. Traces shown are from 12-channel array, time $t = 8$ μs with a 3 μs window. Inset fast camera image is from same experiment, time $t = 8$ μs. Stark broadening of H-β increases from low to high z; Ar II lines are brightest at high z.

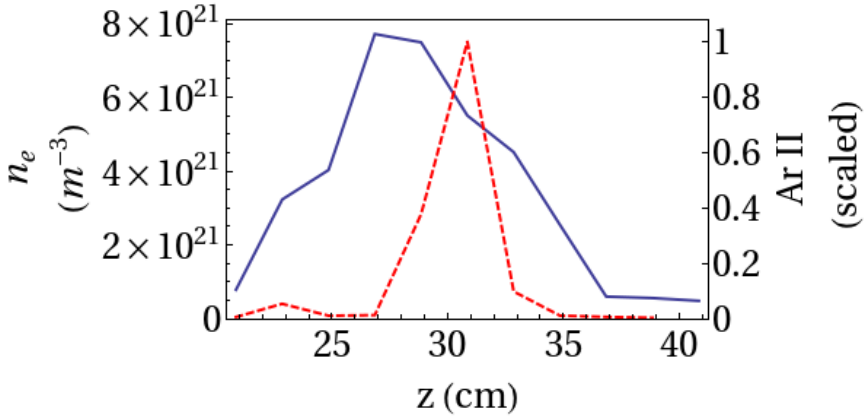

Figure 3.5: Plot showing density as a function of z. Calculated from Stark broadening of H-β in the spectroscopic measurements shown in Fig. 3.4. Red-dashed curve shows scaled intensity of Ar II line at 487.99 nm as a proxy for location of ionized argon. Note that the peak hydrogen density is before the peak argon brightness, as the plasma has piled up outside the neutral gas cloud.

magnetic field in both the neutral cloud region (high z) and in the plasma pile-up region (low z), as shown in Fig. 3.6a and b. Because there is some variability from shot to shot, we performed several experiments with and without a neutral cloud present at each location. Results from these experiments, Fig. 3.6c and d, show that the magnetic field peak value is lower in the neutral cloud region when compared to the case with no neutral cloud (left column in Fig. 3.6), and that the peak magnetic field is higher in the plasma pile-up region in front of the neutral cloud when compared to the field in the case with no neutral cloud (right column in Fig. 3.6).

Magnetic measurements were then made with the z-axis MPA to verify this effect over the course of a single plasma shot. These data confirm that deformation of the plasma jet involves a compression of both density and of embedded magnetic field (Fig. 3.7). We can compare the peak magnetic field strength for an experiment in which the plasma jet collides with a neutral argon cloud to the peak magnetic field strength for an experiment in which no neutral cloud is present (Fig. 3.8). At z values just before the neutral cloud, the peak field strength in the neutral cloud case is 2.5 times the peak value in the case with no neutral cloud. This region of increased magnetic field strength corresponds to the increased density in the plasma jet pile-up region observed in fast camera images. At large z (farther from the electrodes) the peak magnetic field strength drops below half the peak field in the no neutral gas case. This region of decreased magnetic field strength corresponds to the neutral cloud region. Thus, this shows that the plasma and its embedded magnetic field do not penetrate the neutral cloud because they have piled up in front of the neutral cloud.

Though the plasma jet is traveling at super-sonic velocities, there is no shock wave associated with the plasma pile-up. A shock forms where a flow transitions from super- to sub-sonic velocities (or, in the case of MHD shocks, super- to sub-Alfvénic) [31]. So there are two critical velocities to consider when determining whether a shock is present in the plasma jet: the ion sound speed $c_s = \sqrt{\gamma Z k T_e / m_i}$ and the Alfvén velocity $v_A = B/\sqrt{\rho \mu_0}$. Plasma jets in the Caltech experiment are slower than Alfvénic; the hydrogen jet travels at about the toroidal field Alfvén velocity and hence is not transitioning from above to below the Alfvén velocity when slowed by the neutral cloud. For a temperature of $T \sim$ 1–2 eV, the ion sound speed is $c_s \sim$ 10–14 km/s. The jet velocity drops from $\sim$ 50 km/s to $\sim$ 12 km/s; based on this observation and the calculated ion sound speed range, it is possible that the flow would be transitioning from super- to sub-sonic at the interaction region. However, MHD shock width (the distance over which the density, velocity, and other parameters change) is usually about $\delta = l_{mfp} v_T / \Delta V$, where l_{mfp} is the mean free path, v_T the thermal velocity, and ΔV the change in velocity across the shock [31]. In most cases this makes the change in parameters near-discontinuous. In this hydrogen jet, $l_{mfp} = 0.02$ cm, $v_T \sim 10^4$ m/s, and $\Delta V = 3.8 \times 10^4$ m/s, giving a shock thickness of $\delta \sim 5 \times 10^{-5}$ m. However, Fig. 3.5 shows that the density drops over several centimeters. Because there is not an observed discontinuity of the density or magnetic field at the boundary of the pile-up region, this boundary does not satisfy the conditions of a shock.

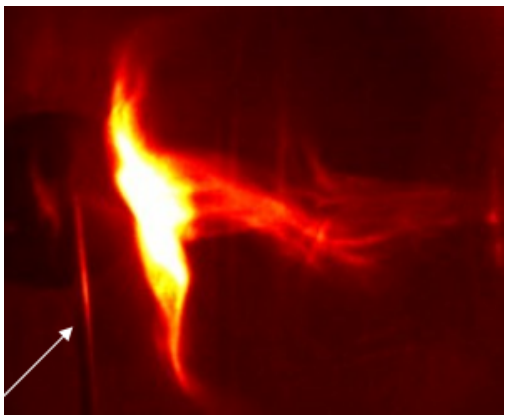

(a)

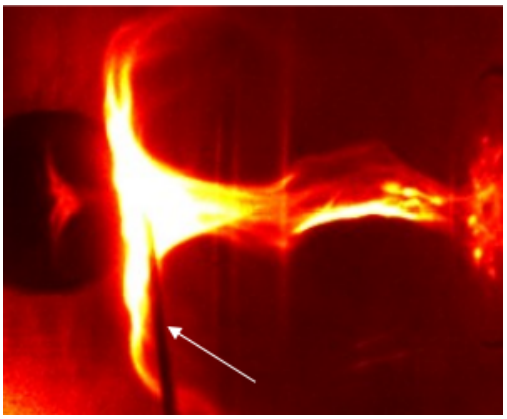

(b)

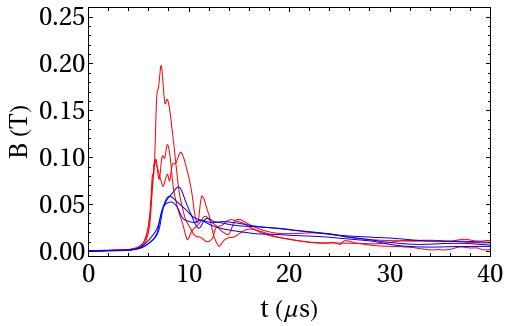

(c) MPA at 31 cm, in neutral gas cloud

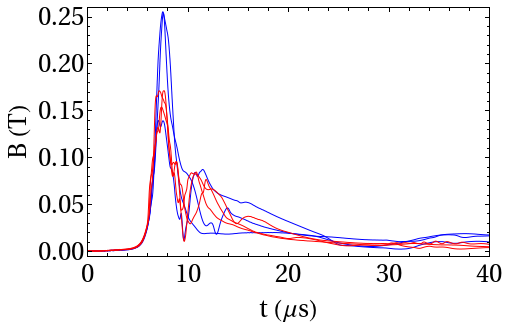

(d) MPA at 25 cm, in pile-up

Figure 3.6: Magnetic data comparing experiments with a neutral nitrogen target (blue) and experiments with no neutral target (red). The data show that the magnetic field "piles up" with the plasma. (a) Fast camera image showing the probe location for the neutral cloud region ($z = 31$ cm, $r = 9$ cm, shot #8268). (b) Fast camera image showing the probe location for the pile-up region ($z = 25$ cm, $r = 9$ cm, shot #8406). (c) Data from the neutral cloud region ($z = 31$ cm, as shown in (a)): Red traces show total magnetic field data for 3 experiments with a neutral nitrogen cloud (shots #8269, 8272, 8273) and blue traces show total magnetic field for 3 experiments with no neutral cloud (shots #8270, 8271, 8274). (d) Data from the pile-up region ($z = 25$ cm, as shown in (b)): Red traces show total magnetic field data for 3 experiments with a neutral nitrogen cloud (shots #8428, 8429, 8430) and blue traces show total magnetic field for 3 experiments with no neutral cloud (shots #8419, 8423, 8424). In these experiments, $V_{gun} = 5$ kV, $\Psi_{gun} = 1.35$ mWb.

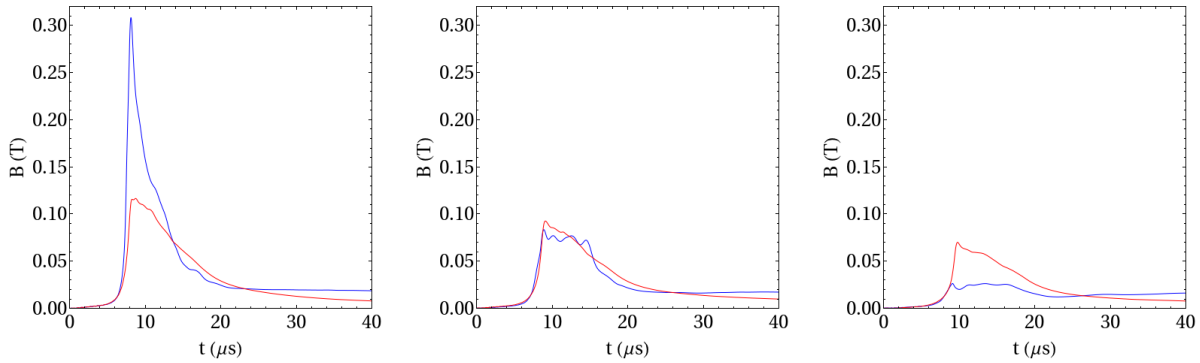

(a) $z = 31$ cm, pile-up region. (b) $z = 33$ cm (c) $z = 35$ cm, neutral cloud region.

Figure 3.7: Magnetic data comparing an experiment with a neutral argon target (blue, shot #10551) and an experiment with no neutral target (red, shot #10533). The three plots show the total magnetic field strength on the central axis at three different z locations; from left to right, $z = 31$, 33, and 35 cm. The left-most plot corresponds to the pile-up region, the right-most to the neutral cloud region. In these experiments $V_{gun} = 5$ kV, $\Psi_{gun} = 1.08$ mWb.

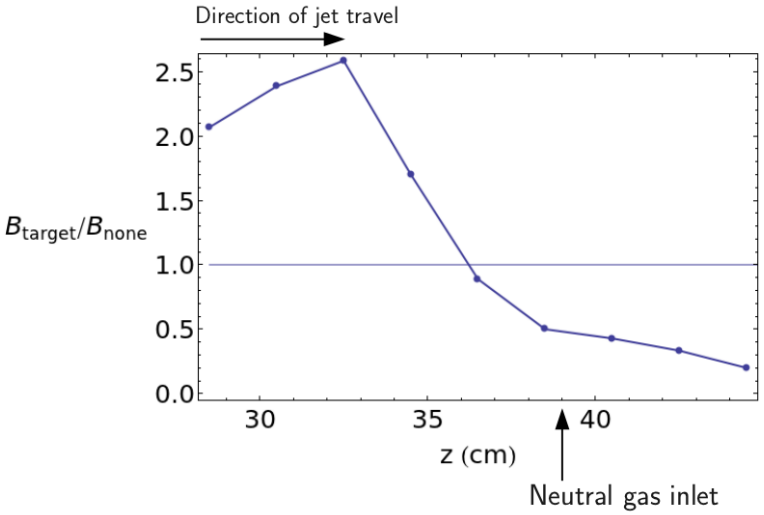

Figure 3.8: The ratio of the peak magnetic field in the neutral gas collision case to the peak magnetic field in the case with no neutral gas target as a function of position. This shows that in a collision experiment the magnetic field strength is amplified in the plasma pile-up region, drops over the interaction region, and is considerably lower in the neutral cloud region as compared to the magnetic field strength in no-collision experiments.

3.1.4 Momentum analysis

We can estimate the momentum change of the jet two ways, and also measure the total jet momentum directly using a ballistic pendulum. The two estimates yield similar values and are of the same order as the independent measurement.

We can use the fast camera image of the collision experiment to estimate that at time $t = 8.75$ μs (which we will consider the end of the collision interaction for these calculations) the lowest z value affected by the collision is $z = 24.5$ cm. This means that the jet material at lower z has not participated in the collision, and so its momentum does not need to be taken into account for this calculation. Fast camera images show that the jet has an initial velocity of ~ 50 km/s and that the velocity at $t = 8.75$ μs is ~ 17 km/s.

The first momentum calculation estimates jet volume affected by comparing a collision experiment and a non-collision experiment with the same settings. Because we know that only the jet past $z = 24.5$ cm has been affected, we can estimate the volume of the jet affected by the collision by measuring the dimensions of the non-collision experiment jet at this same time. The volume estimate can then be combined with the approximate density of the unaffected jet to determine momentum change.

The non-collision jet at $t = 10.75$ μs has a length of about 38 cm, with the front about 4 cm thick and 29 cm in diameter. The jet column is approximately 7.5 cm in diameter. We are only interested in the volume of the jet past $z = 24.5$ cm, which gives us a volume of

$$V = \pi(.0375)^2(.38 - .245 - .04) + \pi(.145)^2(.04) = 3 \times 10^{-3} \text{ m}^3.$$

Spectroscopic measurements give a plasma density of $n \sim 3 \times 10^{21}$ m^{-3}. Assuming that this entire volume slows to 17 km/s, this gives us a momentum change of

$$\Delta p_{jet} = M\Delta v = (3 \times 10^{-3})(3 \times 10^{21})(1.7 \times 10^{-27})(50 \times 10^3 - 17 \times 10^3) = 5 \times 10^{-4} \text{ kg m/s}. \quad (3.1)$$

The second momentum calculation estimates jet volume directly from the collision experiment and uses the spectroscopic measurements of density to calculate mass. We assume that all material in that volume has changed by the same velocity to calculate momentum change.

Again, only the jet material past $z = 24.5$ cm has been affected by the collision, and we measure the jet front to have reached $z = 29.5$ by $t = 8.75$ μs. The jet front is ~ 4 cm thick and we will approximate it as a disk despite its deformation. The small length of affected column has a diameter of ~ 7.5 cm. Stark broadening measurements (see Fig. 3.4) indicate that the density in the first 2 cm of the jet front is $\sim 7.5 \times 10^{21}$ m^{-3}, and then drops to $\sim 6 \times 10^{21}$ m^{-3} for the second 2 cm. The trailing column has a density

of $\sim 3.5 \times 10^{21}$ m^{-3}. This gives a total mass of

$$M = ((\pi(.145)^2(.02)(7.5 \times 10^{21})) + (\pi(.145)^2(.02)(6 \times 10^{21}) + (\pi(.0375)^2(.01)(3.5 \times 10^{21})))1.7 \times 10^{-27} = 3 \times 10^{-8} \text{ kg}.$$

Assuming that this entire mass slows to 17 km/s, this gives us a change in momentum of

$$\Delta p_{jet} = M\Delta v = (3 \times 10^{-8})(50 \times 10^3 - 17 \times 10^3)) = 1 \times 10^{-3} \text{ kg m/s}. \tag{3.2}$$

This is a factor of two larger than the first estimate (Eq. (3.1)), which is in reasonable agreement given the assumptions made in each estimate.

To verify that these values are within reason, we can compare them to measurements of total jet momentum. A ballistic pendulum designed and built by Summer Undergraduate Research Fellowship student Franz Sauer measured the momentum of a hydrogen plasma (with the setting used here, $V_{gun} = 5$ kV and $V_{bias} = 200$ V) jet to be $\sim 4 \times 10^{-4}$ kg m/s [58]. Both our estimates (Eqs. (3.1) and (3.2)) are larger than, but of the same order as, this measurement.

Now we compare this momentum change to the momentum change in the initially neutral gas target cloud. The neutral gas cloud is moving at the gas thermal velocity, which is orders of magnitude less than the velocity of the plasma jet. We can consider the neutral cloud to be stationary before the collision (and hence to have no momentum), and we assume that the gas swept up by the jet is traveling at the final jet velocity after the collision.

From fast ion gauge measurements (see Appendix B), we know that the density of the neutral gas cloud as a function of distance d from the gas inlet is $n(d) = 1.1 \times 10^{18} d^{-2}$. From fast camera images we see that the jet length is 20 cm at the beginning of the collision interaction, and has reached a length of 29.5 cm by the end of the collision interaction. To estimate the momentum transferred to the cloud we must calculate the number of neutral gas particles in the cloud in this region, so we assume a conical cloud with an opening angle of 45° and assume that density is constant at any given distance from the gas inlet within this cone (see Appendix B for more detail). To estimate the total number of particles swept up we center a spherical coordinate system at the gas inlet ($z = 39$ cm) and integrate $n(r)dV$ to get:

$$N = \int_0^{2\pi} d\phi \int_0^{\pi/4} \sin\theta d\theta \int_{.095}^{.19} r^2 1.09 \times 10^{18} r^{-2} dr = 1.9 \times 10^{17} \text{ particles}.$$

For argon atoms that have a final velocity of 17 km/s, this gives a momentum change of

$$\Delta p_{cloud} = Mv = (1.9 \times 10^{17})40(1.7 \times 10^{-27})17 \times 10^3 = 2 \times 10^{-4} \text{ kg m/s}.$$

This value is consistent with the estimated values of momentum change for the jet. A former disagreement of 2 orders of magnitude in these values led us to discover the incorrect neutral gas density value used previously, as discussed further in Appendix B.

3.2 Shock launched in neutral hydrogen cloud by argon jet

Collision experiments in which an argon plasma jet hits an initially neutral hydrogen cloud are less visually dramatic than the reverse case described above. The argon jet front maintains a significant fraction of its velocity and plows through the hydrogen, launching a shock wave into the target cloud.

3.2.1 Visible interaction

As in the case of the hydrogen jet hitting the argon cloud, we can use the fast camera images to estimate the argon jet's velocity loss (Fig. 3.9). The velocity change in this case is less than in the case of hydrogen plasma hitting argon (compare Figs. 3.9 and 3.2), but we can still measure a slowing of the jet front and observe that the jet loses about 25% of its initial velocity, slowing from 22 km/s to 16 km/s.

Optical filters can be used with the fast camera to separate the dynamics of the hydrogen and the argon. In unfiltered fast camera images we observe a region of faint light in front of the jet, with a brighter, distinct linear edge at its front. Use of a transmission filter, centered on the Balmer series H-α line at $\lambda = 656.3$ nm and with a bandwidth of 1.2 nm, allows us to view hydrogen emission only. By blocking out the emission from the bright argon plasma jet, we observe that this bright region and its bright leading edge are in fact excited neutral hydrogen. A composite image made with a background image of the unfiltered light and an overlaid image of hydrogen emission is shown in Fig. 3.10.

The bright linear structure launched by the jet front has a velocity of ~ 1.4 times the jet velocity, indicating a possible shock wave launched into the neutral cloud by the plasma jet.

To predict the shock speed, we can model the front of the plasma jet as a piston moving at a constant velocity v_j into an undisturbed gas. If v_j is greater than the speed of sound in the gas c_s, then the piston will launch a shock wave into the gas. The speed of sound c_s in the neutral hydrogen cloud is

$$c_s = \sqrt{\gamma \frac{P}{\rho}} = \sqrt{\gamma \frac{kT}{m_i}} = \sqrt{\left(\frac{7}{5}\right) \frac{\left(\frac{1}{40}\right) 1.6 \times 10^{-19}}{2(1.7 \times 10^{-27})}} = 1283 \text{ m/s},$$

where γ is the adiabatic index, $\gamma = 7/5$ for a diatomic ideal gas. The argon plasma jet front is traveling at $v_j \sim 16$ km/s, which is much greater than $c_s = 1.3$ km/s.

The Rankine–Hugoniot jump conditions describe the change in variables across a shock propagating with a normal parallel to the flow. They are found by integrating conservation equations across the shock

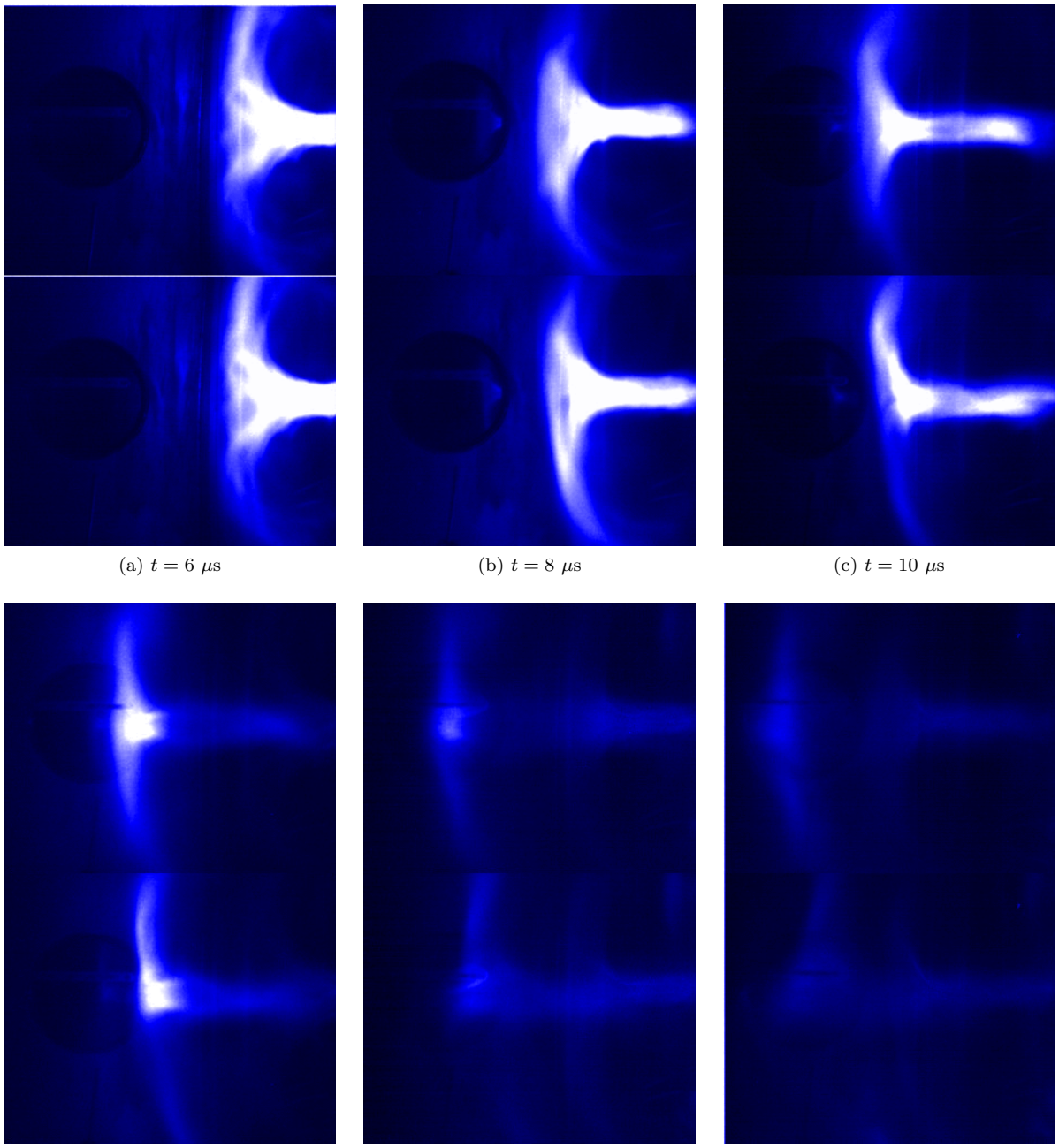

(a) $t = 6$ μs (b) $t = 8$ μs (c) $t = 10$ μs

(d) $t = 12$ μs (e) $t = 14$ μs (f) $t = 16$ μs

Figure 3.9: Visible light images from the fast camera show the argon plasma jet front slowing only minimally as it interacts with the hydrogen neutral cloud. Top image in each set is with no neutral cloud, bottom image in each set is with a hydrogen neutral cloud. The first images show the jet fully formed but before interaction with the neutral cloud, $t = 6$ μs. In the middle image the jet front has just encountered the neutral cloud, $t = 10$ μs. Bottom row images show the jet front slowed but with little to no visible thickening, final image $t = 16$ μs. The linear feature visible on the left is the z-axis magnetic probe array. Image is false-colored and intensity is scaled logarithmically for display clarity; some ghosting of earlier frames is visible in final two sets of images. Shot #10572 and 10577, $\Psi = 1.62$ mWb.

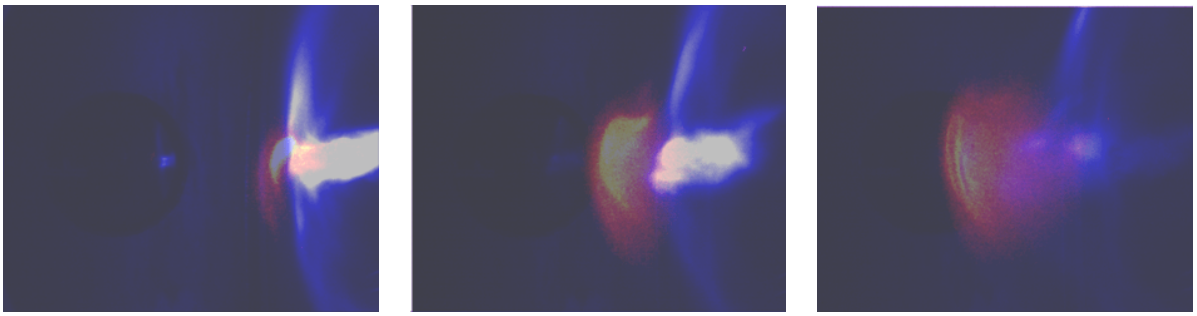

(a) $t = 8$ μs (b) $t = 10$ μs (c) $t = 12$ μs

Figure 3.10: Visible light images overlaid with filtered light images, both from the fast camera. The overlaid images are from two different experiments with the same settings; the blue image is unfiltered visible light and the red image is light filtered with an H-α optical filter, centered at 656.3 nm with a 1.2 nm bandwidth. These images show that the bright region ahead of the jet front is excited neutral hydrogen. Images are false-colored and intensity is scaled logarithmically for display clarity. Shot #9816 and 9818, $\Psi = 1.08$ mWb.

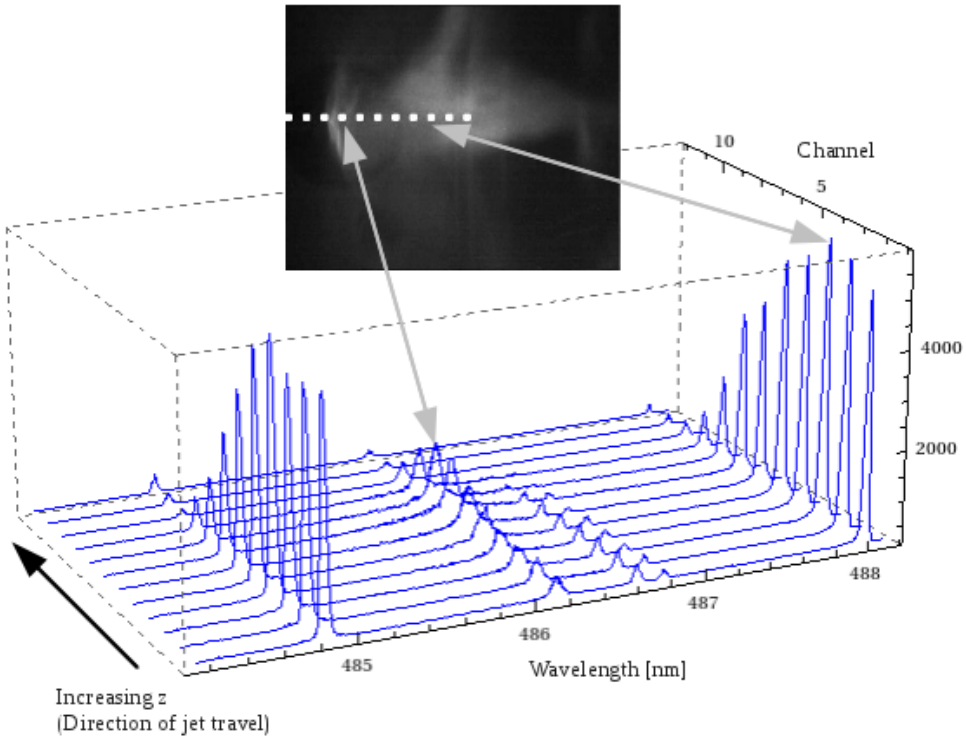

Figure 3.11: Spectroscopic data show some Stark broadening of H-β lines and bright ionized argon lines. Traces shown are from 12-channel array, time $t = 12$ μs with a 2 μs window; inset fast camera image is from same experiment, time $t = 13.5$ μs. Shot #9852

interface. In the frame in which the shock is stationary, the gas "downstream" of the shock (the shocked gas) has mass density ρ_1, pressure P_1, and flow velocity $u_1 = v_j - v_s$, and the gas "upstream" of the shock (the unshocked gas) has mass density ρ_2, pressure P_2, and flow velocity $u_2 = -v_s$. In this frame the jump conditions are:

$$\text{Conservation of mass:} \qquad \rho_1 u_1 = \rho_2 u_2 \tag{3.3}$$

$$\text{Conservation of momentum:} \qquad \rho_1 u_1^2 + P_1 = \rho_2 u_2^2 + P_2 \tag{3.4}$$

$$\text{Conservation of energy:} \qquad \frac{1}{2}\rho_1 u_1^3 + \gamma P_1 u_1 = \frac{1}{2}\rho_2 u_2^3 + \gamma P_2 u_2. \tag{3.5}$$

Combining the jump conditions to eliminate ρ_1 and P_1 and then using $c_s^2 = \gamma P_2/\rho_2$ gives us an expression relating u_1 and u_2 [31]:

$$(3\gamma - 1)u_1 = u_2 + \frac{(3\gamma - 2)c_s^2}{u_2}. \tag{3.6}$$

Substituting $u_1 = v_j - v_s$ and $u_2 = -v_s$ into Eq. (3.7) gives

$$(3\gamma - 1)v_j = (3\gamma - 2)\left(v_s - \frac{c_s^2}{v_s}\right). \tag{3.7}$$

For $v_j \gg c_s$, the shock is called a strong shock.

The velocity of the shock v_s in the hydrogen cloud can be estimated, using the strong shock approximation, as:

$$v_s \sim \left(\frac{3\gamma - 1}{3\gamma - 2}\right) v_j = \left(\frac{3(1.4) - 1}{3(1.4) - 2}\right) 16 \sim 23 \text{ km/s}.$$

The velocity of the shock front as measured in fast camera images is $\sim$ 25 km/s, in agreement with the estimate from this simple model.

3.2.2 Spectroscopic measurements

From Eq. (3.4) we expect a density downstream of the shock 3.2 times that upstream of the shock. Spectroscopic measurements of the hydrogen neutral cloud show a slightly Stark-broadened H-β line (Fig. 3.11). We observe H-β lines at low z, indicating that some hydrogen has been incorporated into the argon jet. Stark broadening analysis of lines of sight in the shocked hydrogen region gives a peak density of 2.4×10^{20} m^{-3}. At the time of this spectroscopic measurement (12–14 μs), the shock front travels from a distance of 10 cm from the gas inlet to 7 cm from the gas inlet. Based on fast ion gauge measurements, the neutral gas density at this location should be $\sim$1–2$\times 10^{20}$ m^{-3}. The Stark broadening measurements confirm that the density in the shocked gas is of the same order as the neutral gas just upstream of the shock, which is as

accurate as possible given resolution limits in the spectroscopic measurements and uncertainty in the neutral gas density.

3.2.3 Momentum analysis

We can again estimate the momentum change of the jet to verify that it is in agreement with an independent measurement of the total jet momentum made with the ballistic pendulum and that the collision interaction conserves momentum. This is a bit more challenging than in the hydrogen jet's collision with a neutral argon cloud case, as the interaction is less pronounced.

Using the fast camera method similar to that described in Section 3.1, we estimate the change in jet momentum to be $\Delta p_{jet} \sim 6 \times 10^{-4}$ kg m/s, about half the momentum of the jet measured by the ballistic pendulum [58].

We compare this momentum change to the momentum change in the initially neutral hydrogen target cloud. The hydrogen goes from effectively stationary to traveling at the final velocity of the plasma jet, 16 km/s. We estimate the change in momentum of the hydrogen cloud to be $\Delta p_{jet} \sim 1 \times 10^{-4}$ kg m/s which is less than, but of the same order as, the jet momentum change.

3.3 Critical ionization velocity (CIV) and its role in collision dynamics

As its name suggests, critical ionization velocity (CIV) is a velocity at which ionization effects become important in collision dynamics. The theory applies to neutral particles moving through a plasma in the presence of a magnetic field; if the magnetic field has a component perpendicular to the relative velocity of the neutrals and plasma, the neutrals will ionize when the relative velocity reaches a critical value,

$$v_c = \sqrt{\frac{2\phi_n}{m_n}}, \tag{3.8}$$

where ϕ_n is the ionization potential of the neutral gas. The magnetic field traps the now-ionized particles and the relative velocity drops to zero.

Alfvén first proposed the idea of a critical ionization velocity (CIV) in a model for solar system formation [1, 2]. Alfvén used this theory to predict bands of elements orbiting a central massive body at different radial positions. He hypothesized that elements with a larger v_c would fall in farther before ionizing and becoming trapped by the sun's magnetic field, leading to stratification in the disk. The theory as originally proposed simply balances kinetic and ionization energy, a simplification of a complicated interaction, but provides no mechanism by which the heavy ions transfer their kinetic energy to the plasma electrons to ionize the neutrals.

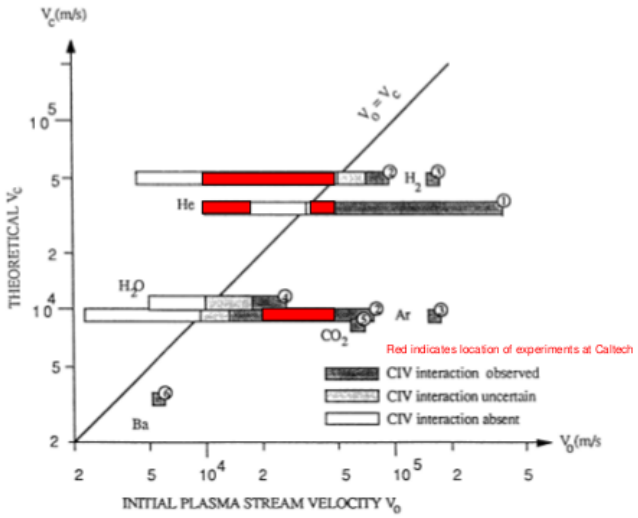

Fig. 26. The occurrence of CIV interaction as a function of the initial velocity in the impact experiments. The experiments are: (1) Danielsson, 1979; (2), (3) Venkataramani and Mattoo, 1980; (4) Chang, 1988; (5) Danielsson and Kasai, 1968; (6) Haerendel, 1982; Torbert, 1990.

Figure 3.12: A plot showing the parameter range and results of impact experiments studying CIV effects. Red boxes show collision experiments performed at Caltech. Original figure taken from Brenning, 1992 [12]

Nevertheless, the theory has proven fairly robust, with the effect identified in experiments over a wide range of magnetic field strengths and particle densities [12, 36]. More recent refinements to the theory attempt to address the energy transfer mechanism. Forerunners include the lower hybrid instabilities [36], specifically the modified two-stream instability [52, 59]. The requirements for the modified two-stream instability as a mechanism predict an effective range for the CIV interaction [11] shown in Fig. 3.13. As the critical ionization effect continues to be important in space applications, as well as in any laboratory experiment in which neutrals and plasmas interact, a greater understanding of the effect is desirable. Past experiments yielded mixed results, with laboratory experiments often seeing a CIV effect and space experiments rarely seeing a CIV effect [12, 36].

The interaction of the plasma jet and neutral cloud can be cast as a CIV interaction. As is required for a CIV effect, there is a magnetic field component perpendicular to the relative velocity of the neutral and plasma at the jet front, in this case B_r. The magnetic field moves with the plasma; hence, in the plasma frame, the neutral gas is moving into the stationary magnetized plasma at the jet velocity. In hydrogen jet/argon neutral cloud experiments the jet velocity of ~ 50 km/s is much faster than the critical velocity of argon, $v_c = 8.7$ km/s. In argon jet/hydrogen neutral cloud experiments the jet velocity of ~ 20 km/s is slower than the critical velocity of hydrogen, $v_c = 50.9$ km/s. The jet interaction with the neutral cloud is consistent with other CIV collision experiments.

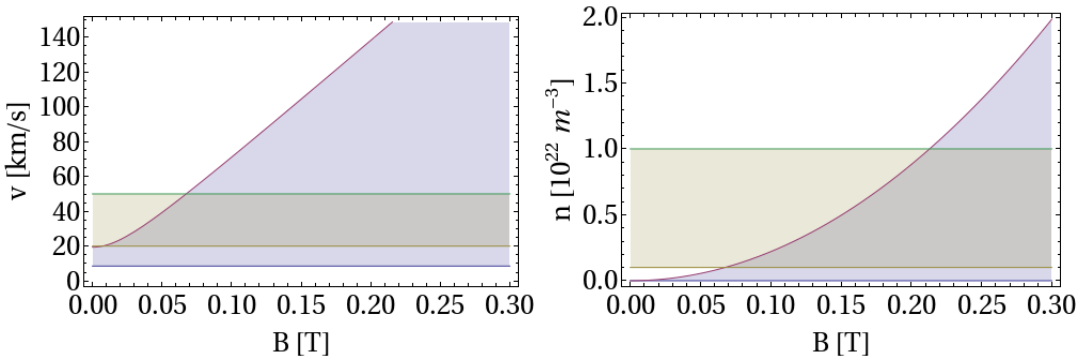

Figure 3.13: A proposed mechanism for CIV produces bounds on when the effect should be present. (a) Blue-shaded area represents the velocity range in which the CIV effect should be seen, as a function of magnetic field strength. The lower limit is the critical ionization velocity and the upper limit is $v = v_A\sqrt{1+\beta}$, the velocity at which electromagnetic modes are excited [11]. Tan-shaded region is the velocity range in the Caltech experiment. Values are determined for an argon neutral gas and a hydrogen plasma with density $n_e = 10^{21}$ m^{-3} and temperature $t = 2$ eV. (b) Blue-shaded area represents the plasma density range in which the CIV effect should be seen, as a function of magnetic field strength. The plotted range is determined by $\sqrt{m_e/m_n} < \omega_{pe}/\omega_{ce} < c/v\sqrt{(1+\beta)m_e/m_i}$. The upper velocity limit from (a) gives the upper limit for the density and the lower limit is set by the requirement that growth rate of the instability be much greater than ω_{ci} [11]. Tan-shaded region is the density range in the Caltech experiment.

3.4 Relevance to astrophysical jets

Astrophysical observations of jets, especially those associated with young stellar objects (YSOs), have recently reached a sufficiently long time lapse at a sufficiently fine spatial resolution to study the dynamical evolution of these systems in detail [22]. Comparisons of time-resolved images have shown that the interaction of YSO jets with the surrounding medium produces complex structures that evolve in time. Shocks occur where the YSO jets move into the surrounding medium; bow shocks, which have been seen in past observations [3, 24, 54] and faint "bubble" regions in front of these structures [22] that resemble the shock launched by the plasma jet into the neutral gas region in Caltech collision experiments. In addition, these time-resolved images show regions within the jet in which faster material overtakes slower material [22], much like the pile-up observed in collision experiments at Caltech. Based on experimental results, we would expect amplification of the jet magnetic field in these pile-up regions commensurate with the density increase.

Chapter 4

Breathing mode and two-dimensional behavior

This chapter describes a behavior seen in the jet experiment after the addition of the pulse forming network (PFN) power supply described in Chapter 5. Using the short duration power supply for plasma breakdown and the PFN for sustainment generates a current trace that fluctuates several times over the course of the experiment (see Fig. 4.1, and see Section 5.5 for more about the PFN current). This current fluctuation means a fluctuation in the toroidal magnetic field, which relates to the jet radius. By studying the nature of the changes in the jet we see that the jet behaves quasi-two-dimensionally.

4.1 Observations of jet and current channel radius

The magnetically driven plasma jet generated by the Caltech experiment can be unstable to the current-driven kink instability described in Section 1.4.2. The factor that determines jet stability is $\alpha = \mu_0 I/\Psi$; the jet is kink-unstable when $\alpha > 4\pi/\ell$. We can see from the form of α that a larger magnetic flux Ψ will make the jet more stable. The magnetic flux Ψ is the integral of the applied background magnetic field over the area of the inner electrode; hence, a large applied field makes the jet more stable against kinking.

The longer duration of the PFN current pulse produces physically longer jets than the short-duration power supply. Because the plasma jet stability also depends on the jet length ℓ, approaching instability as ℓ increases, the background magnetic field must be fairly strong to keep the longer jet in the stable regime. The stronger background magnetic field helps keep the jet stable both by keeping Ψ large and by keeping ℓ smaller: to expand in z the jet must fight against the tension of the magnetic field lines, and so it travels at a slightly lower velocity than lower background magnetic field plasma jets.

In straight jets created using only the short-duration capacitor bank, the jet gradually widens as the current drops, eventually becoming diffuse. With PFN sustainment, the jet forms, widens, recollimates, and then widens again, the radius changing in inverse proportion to fluctuating current amplitudes (Fig. 4.1).

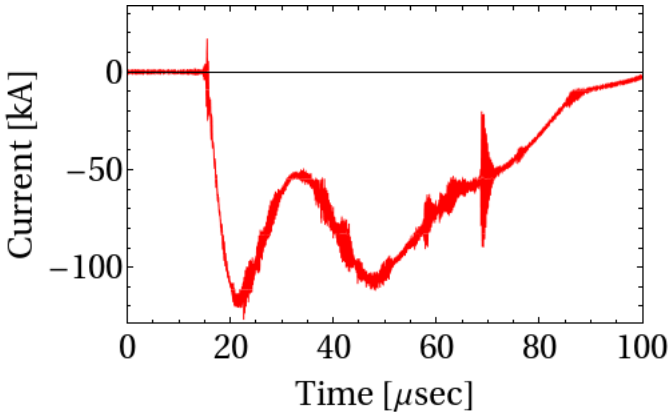

Figure 4.1: The current fluctuates over the course of a high bias magnetic field experiment with the PFN and capacitor bank. Shot #11200; corresponds to fast camera image in Fig. 4.2 below.

This effect is visible in both fast camera images and in current measurements.

Fast camera images show that, in early times, straight argon plasma jets resemble those generated using the short-time-duration power supply. Once fully formed, the radius of the column viewed in fast camera images expands, contracts, and expands again in a "breathing" manner, as seen in Fig. 4.2.

The plasma jet is a current-carrying plasma-filled flux tube, but the visible jet does not necessarily coincide exactly with the region through which the electrical current flows, called the current channel. For example, we know from previous experiments that the current channel in hydrogen plasmas has a larger diameter than the visible plasma jet, extending out to a $\sim$ 10 cm radius for a plasma jet, with a visible radius of $\sim$ 3 cm as measured from fast camera images [35].

We can measure the current channel as a function of time to verify the apparent "breathing" behavior. The current channel radius is calculated using data from the r-axis magnetic probe array (MPA). For a jet with cylindrical symmetry (i.e., not kinked), we measure B_θ and calculate the current enclosed at that radius using Ampere's law

$$\oint_C \mathbf{B} \cdot d\mathbf{l} = \mu_0 I_{enclosed}$$
$$\int_0^{2\pi} B_\theta r \, d\theta = \mu_0 I_{enclosed}$$
$$I_{enclosed}(r) = \frac{\mu_0}{2\pi r B_\theta}.$$

We plot the current enclosed at each radial measurement location at a specified time, and then determine the current channel radius as the r position at which the current has reached a certain fraction for the peak current value measured in the channel $0.65 I_{peak}$ (see Fig. 4.3). It is worth noting that in these argon experiments the jet radius, as measured from fast camera images, is essentially the same as the current

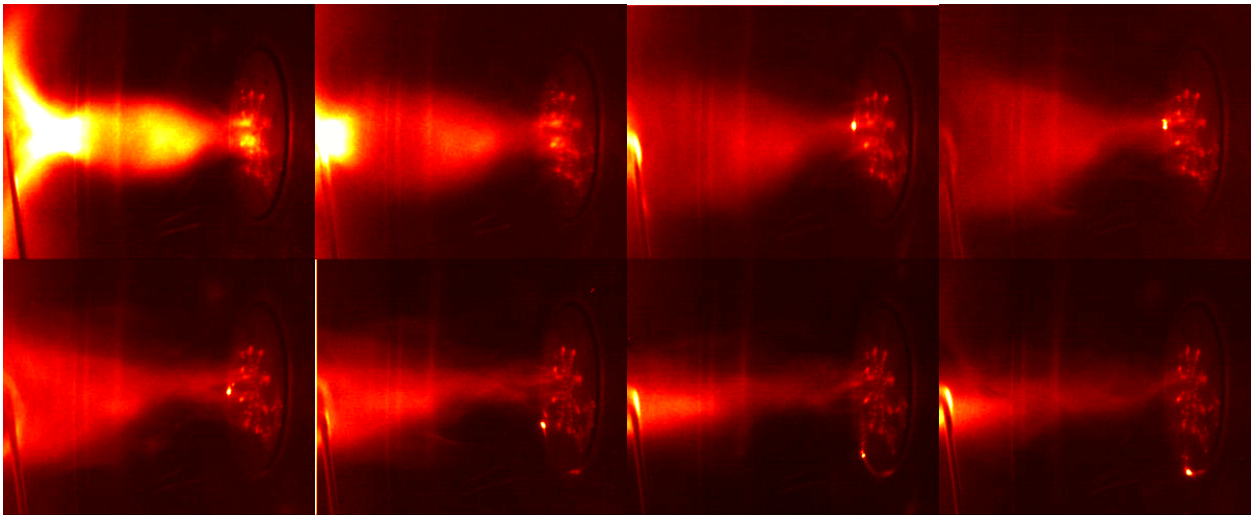

Figure 4.2: Fast camera images showing the plasma "breathing" with the fluctuating current. Images shown range from $t = 16$ μs to $t = 37$ μs. Shot #11200

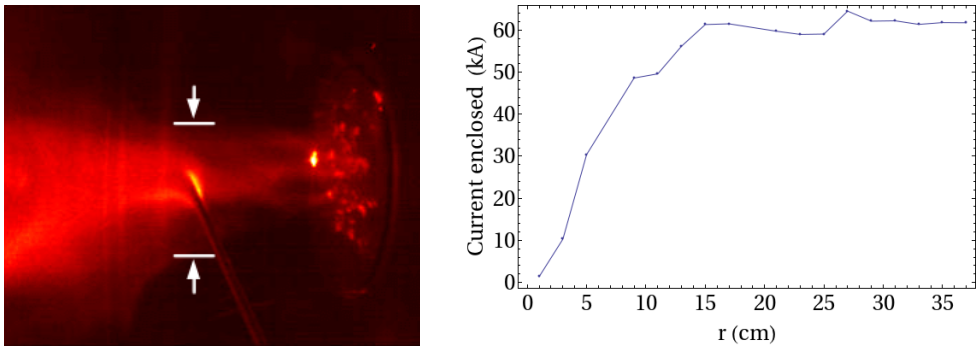

(a) Camera image showing jet diameter

(b) Enclosed current at $z = 14$ cm, $t = 30$ μs

Figure 4.3: Fast camera image of plasma jet indicating diameter and current channel measurement. (a) An argon jet at 30 μs after plasma breakdown. The arrows indicate the diameter at the z location of the r axis MPA, which measures the current channel. Radius estimated from the camera image is $r \sim 6$ cm. (b) Plot of the current enclosed within the jet as a function of radius, calculated from B_θ as described in the text. The enclosed current increases as a function of r in the jet and then levels off at the peak value once outside the jet (the return current is outside the measured radius). The radius of the current channel is $r = 0.65 I_{peak} \sim 7$ cm. Note that the peak enclosed current measured is ~ 62 kA, while the current measured at the electrode at this time is ~ 98 kA.

channel calculated from magnetic data, unlike hydrogen jets for which the current channel is significantly larger.

The time-changing current channel radius was measured at several z locations along the jet length, and the results are shown in Fig. 4.4. Current values are plotted for each time at which current channel radius was measured, allowing us to compare the fluctuations of the current in time with fluctuations in the current channel radius with time. Close to the electrodes, at a low z value, the radius of the current channel is inversely proportional to the current amplitude (Fig. 4.4a). The current starts high and the current channel radius low; then as the current drops the radius increases, reaching a peak radius at approximately the same time that the current amplitude reaches a minimum. The current channel radius then drops to a minimum at approximately the same time that the current amplitude reaches its second and final peak.

Measurements of current channel radius taken farther from the electrodes, at higher z, show a similar fluctuating form, but offset in time, so that the peak current channel radius occurs later than the minimum current amplitude (Fig. 4.4b). Taken together, the measurements of current channel radius at various z positions show the column expansion and contraction, as well as propagation of the disturbance up the jet, from electrode (low z) to jet front (high z). Comparing the time of the peak value in the three measurement curves, we estimate that the disturbance propagates at approximately 19 km/s. By noting that the jet front reaches the magnetic probe array position at $z = 28.5$ cm in about $t = 19$ μs, we measure an average jet velocity of approximately 15 km/s.

Rather than the radius of the entire jet fluctuating together in response to the changing current (and hence magnetic field), the disturbance propagates up the column at approximately the jet velocity, the toroidal field Alfvén velocity. The jet response to the current change does not happen simultaneously as might be expected; rather the jet responds closer to the electrodes and then the information propagates in z with the jet.

This behavior may be of interest for laboratory plasma experiments in which collimated flows are important [61, 37]. If the flows are magnetically driven, our observations suggest that any changes in the magnetic field driving the flow would take time to propagate up the flow, rather than taking effect throughout the flow immediately.

4.2 Balancing pressure: The Bennett relation

If a current-carrying column of plasma is in a state of pressure equilibrium, the current can be related to the column radius using the Bennett relation [6], which comes from balancing the magnetic pressure of the

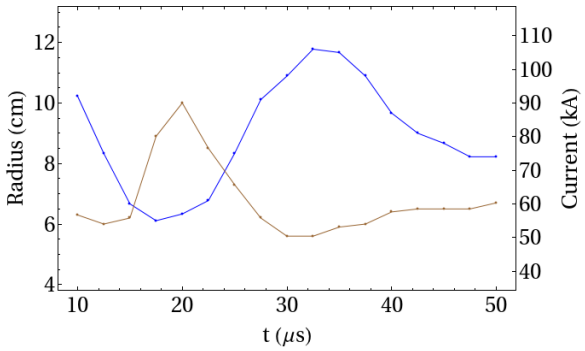

(a) Current channel at $z = 14$ cm

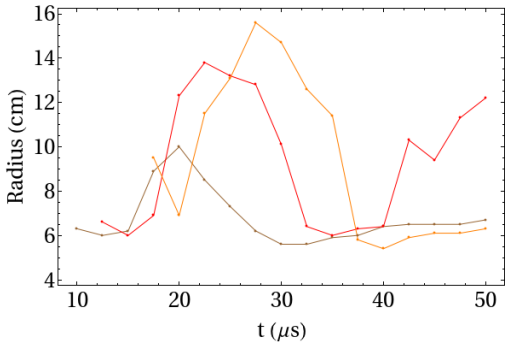

(b) Current channel at $z = 14$, 21, and 28 cm

Figure 4.4: Measurements of the current channel radius as a function of time. (a) The brown trace shows the current channel radius at $z = 14$ cm from the electrodes. Blue trace shows the current through the electrodes at the time of each measurement. Notice that the current varies approximately inversely with the current amplitude. (b) The brown, orange, and red traces show the current channel radius as a function of time at $z = 14$, $z = 21$, and $z = 28$ cm, respectively. At higher z values (orange and red traces), the peak radius appears later in time, offset from the current amplitude minimum.

current-generated magnetic field, $B_\theta^2/2\mu_0$ and the thermal pressure in the plasma column nkT:

$$\begin{aligned} \frac{B_\theta^2}{2\mu_0} &= nkT \\ \frac{1}{2\mu_0}\left(\frac{\mu_0 I}{2\pi r}\right)^2 &= nkT \\ I^2 &= \frac{8\pi NkT}{\ell\mu_0}, \end{aligned} \tag{4.1}$$

where $N/\ell = n\pi r^2$ is number of particles per length.

We would like to understand how the plasma jet radius varies with the current, and so would like to re-express Eq. (4.1) as a relation between I and r. To do so, let us consider a short segment of the plasma column having N particles, with initial radius r and length ℓ. If we assume that the change in the jet radius is adiabatic, then we know that PV^γ is constant, or $P \sim V^{-\gamma}$. Assuming the total number of particles N is constant, the ideal gas law $PV = NkT$ tells us that $T \sim PV$, and hence $T \sim V^{1-\gamma} \sim (r^2\ell)^{1-\gamma}$. Inserting this into the Bennett relation (Eq. (4.1)) gives us:

$$\begin{aligned} I^2 &= \frac{8\pi NkT}{\ell\mu_0} \\ &\sim \frac{T}{\ell} \\ &\sim \frac{(r^2\ell)^{1-\gamma}}{\ell} \\ &\sim r^{2(1-\gamma)}\ell^{-\gamma}. \end{aligned} \tag{4.2}$$

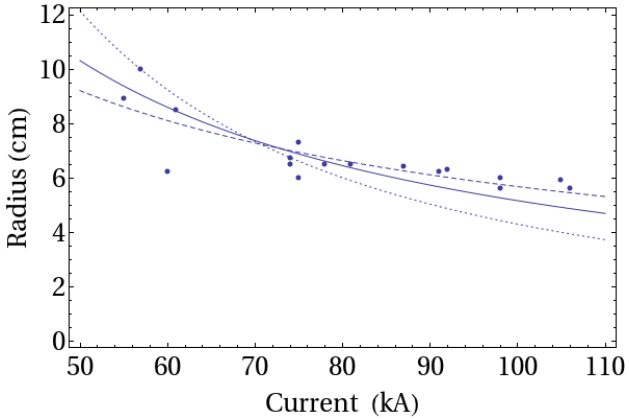

Figure 4.5: The current radius at $z = 14$ cm as a function of current. The data are shown with a $\gamma = 2$ fit (2D, solid line), a $\gamma = 5/3$ fit (3D, dotted line), and $\gamma = 2.4$ fit (best fit to data, dashed line).

If the plasma is compressible and volume compresses only in the radial direction, then the number of particles per length (and hence the ℓ of our N particles under consideration) remains constant. For a constant ℓ, Eq. (4.2) simplifies to

$$\begin{aligned} I^2 &\sim r^{2(1-\gamma)}\ell^{-\gamma} \\ &\sim r^{2(1-\gamma)} \\ \implies r &\sim I^{1/(1-\gamma)}. \end{aligned} \tag{4.3}$$

We would usually use $\gamma = 5/3$ for a monatomic ideal gas; however in this case, we have to be careful when determining the value of γ. We know that $\gamma = (m+2)/m$, where m is the degrees of freedom of the system. We have a monatomic gas, so there are no contributions from either rotation or vibration, and the degrees of freedom are simply the dimensionality of the system. Because we are assuming that the compression happens only radially and not along the length, compression is two-dimensional. This requires that $\gamma = (2+2)/2 = 2$ to be consistent with our assumption of constant length. So in this case, r as a function of I is:

$$r \sim I^{1/(1-\gamma)} = I^{-1}. \tag{4.4}$$

We can plot the current channel radius as a function of current at the position $z = 14$ cm (see Fig. 4.5). Figure 4.5 shows the fit to the data for Eq. (4.4) with $\gamma = 2$ for the two-dimensional compression case. The plot includes the fit using $\gamma = 5/3$, as well as the best fit, $r \sim I^{-0.7}$, which corresponds to $\gamma = 2.4$. The $\gamma = 2$ fit has an R^2 value (a measure of quality for which a value closer to one indicates a better fit) of $R^2 = 0.986$, as compared to the $\gamma = 5/3$ fit value $R^2 = 0.964$ and the best fit value $R^2 = 0.99$. This indicates that $\gamma = 2$ gives a fairly good fit, and supports the notion that the compression of the current channel is a

two-dimensional process.

4.3 Relevance to astrophysical jets

The quasi-two-dimensional behavior may be relevant to the dynamics of astrophysical jets. These jets are believed to be at least partially magnetically driven, and measurements of axial current have been made [30]. In addition, these jets are not homogeneous, but are observed to have structure along their length. If they behave in a manner similar to the magnetically driven jets in the Caltech experiment, any structure due to changes in the current or magnetic field at the disk may propagate up the jet at approximately the Alfvèn velocity. This could be related to structure such as "knots" seen in astrophysical jets like HH 47, which have been observed to travel along the jet length [24].

Chapter 5

Pulse forming network power supply

A pulse forming network (PFN) is a capacitor bank power supply that uses inductors and capacitors in parallel to produce a square voltage pulse. Experiments with the older short-duration power supply produce a plasma jet that exhibits a range of behaviors determined by current-driven instabilities, but the length of the current pulse limits the time duration of the experiment, as the current drops rapidly post-instability-onset. The PFN was designed to provide a current ~ 5 times longer than that previously provided to the plasma experiment, allowing us to study the plasma column post-instability-onset.

5.1 Theory of operation

The pulse forming network design is based on transmission line theory. A transmission line can be modeled as an arrangement of discrete capacitors and inductors. A PFN uses this model to take advantage of transmission line properties (compare Fig. 5.1 and Fig. 5.2); inductors and capacitors produce a square voltage pulse with a height of half the charging voltage and a duration of twice the individual segment LC rise time multiplied by the number of segments.

5.1.1 Review of transmission lines

We begin with a review of transmission line theory, using a coaxial transmission line as an example. A coaxial transmission line, with in inner conductor of radius a and an outer conductor at radius b, can be thought of as a long cylindrical capacitor with inductance. The transmission line has capacitance per length C' and inductance per length L' given by:

$$C' = \frac{2\pi\epsilon_0}{\ln\left(\frac{b}{a}\right)}, \qquad L' = \frac{\mu_0}{2\pi}\ln\left(\frac{b}{a}\right). \tag{5.1}$$

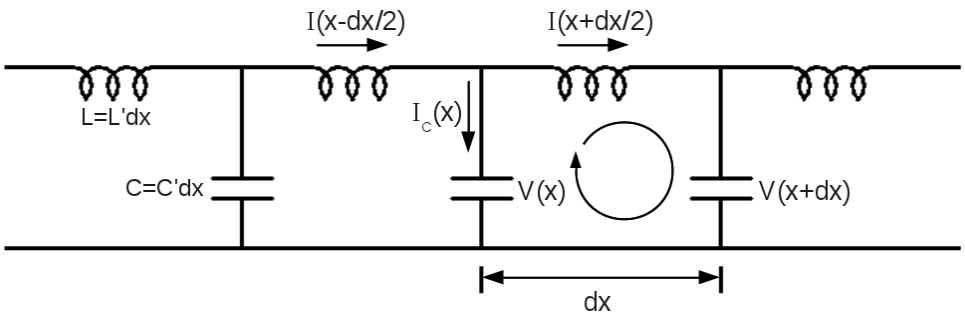

Figure 5.1: A transmission line with inductance per length L' and capacitance per length C' can be modeled as discrete capacitors and inductors. Each capacitor has $C = C'dx$ and each inductor has $L = L'dx$. Each segment loop must satisfy Kirchhoff's voltage law and the junctions must satisfy Kirchhoff's current law.

A transmission line can hence be modeled as discrete capacitors connected in parallel, along with inductors connected in series (see Fig. 5.1). In this model, an individual small segment will have an inductor with $L = L'dx$ and capacitor with $C = C'dx$, with the inductors separated by distance dx and the capacitors separated by distance dx.

The voltage in a segment loop must satisfy Kirchhoff's voltage law, which gives us:

$$\begin{aligned} V(x) - V\left(x + dx\right) &= L'dx\left(\frac{\partial I\left(x + \frac{dx}{2}\right)}{\partial t}\right) \\ -\frac{\partial V}{\partial x} &= L'\frac{\partial I}{\partial t}. \end{aligned} \tag{5.2}$$

The current at the junction must satisfy Kirchhoff's current law, which at this position x is:

$$\begin{aligned} I\left(x - \frac{dx}{2}\right) &= I\left(x + \frac{dx}{2}\right) + I_C(x) \\ I\left(x - \frac{dx}{2}\right) - I\left(x + \frac{dx}{2}\right) &= I_C(x) \\ -\frac{\partial I}{\partial x}dx &= I_C. \end{aligned} \tag{5.3}$$

We can express the current through the capacitor in terms of voltages using the capacitor equation:

$$\begin{aligned} Q &= CV \\ \frac{\partial Q}{\partial t} &= C\frac{\partial V}{\partial t} \\ I_C &= C'dx\frac{\partial V}{\partial t}. \end{aligned} \tag{5.4}$$

We can substitute Eq. (5.4) into Eq. (5.3) to get

$$-\frac{\partial I}{\partial x} = C' \frac{\partial V}{\partial t}. \tag{5.5}$$

Taking the partial derivative of Eq. (5.5) with respect to x gives

$$\begin{aligned} -\frac{\partial^2 I}{\partial x^2} &= C' \frac{\partial^2 V}{\partial x \partial t} \\ -\frac{\partial^2 I}{\partial x^2} &= C' \frac{\partial}{\partial t}\left(\frac{\partial V}{\partial x}\right); \end{aligned}$$

plugging in Eq. (5.2) for $\frac{\partial V}{\partial x}$ gives

$$\begin{aligned} -\frac{\partial^2 I}{\partial x^2} &= C' \frac{\partial}{\partial t}\left(-L' \frac{\partial I}{\partial t}\right) \\ \frac{\partial^2 I}{\partial x^2} &= L'C' \left(\frac{\partial^2 I}{\partial t^2}\right). \end{aligned} \tag{5.6}$$

This is a one-dimensional wave equation, for a wave with velocity $v = 1/\sqrt{L'C'}$.

We can do the same for the voltage, by taking the partial derivative of Eq. (5.2) with respect to x. This gives

$$\begin{aligned} -\frac{\partial^2 V}{\partial x^2} &= L' \frac{\partial^2 I}{\partial x \partial t} \\ -\frac{\partial^2 V}{\partial x^2} &= L' \frac{\partial}{\partial t}\left(\frac{\partial I}{\partial x}\right) \\ &\text{plugging in Eq. (5.5) for } \frac{\partial I}{\partial x} \text{gives} \\ -\frac{\partial^2 V}{\partial x^2} &= L' \frac{\partial}{\partial t}\left(-C' \frac{\partial V}{\partial t}\right) \\ \frac{\partial^2 I}{\partial x^2} &= L'C' \left(\frac{\partial^2 V}{\partial t^2}\right). \end{aligned} \tag{5.7}$$

This is also a one-dimensional wave equation for a wave with velocity $v = 1/\sqrt{L'C'}$.

We can determine the characteristic impedance using Eq. (5.5) and Eq. (5.2). Consider a voltage pulse with shape $V = f(x - vt)$ sent down the transmission line. If we take the partial derivative with respect to position we get

$$\frac{\partial V}{\partial x} = f'(x - vt), \tag{5.8}$$

where the prime indicates the derivative with respect to $x - vt$.

If we take the partial derivative with respect to time we get

$$\frac{\partial V}{\partial t} = -vf'(x - vt). \tag{5.9}$$

Substituting Eq. (5.5) into the above equation gives

$$\frac{1}{C'}\frac{\partial I}{\partial x} = vf'(x - vt). \tag{5.10}$$

Combining equations Eq. (5.8) and Eq. (5.10) to eliminate $f'(x - vt)$ shows that

$$\frac{\partial V}{\partial x} = \frac{1}{C'v}\frac{\partial I}{\partial x} \tag{5.11}$$

$$V = \frac{1}{C'v}I. \tag{5.12}$$

The voltage pulse form and the current pulse form differ only by a numerical constant, $1/C'v$. We know that $V = IZ$; using this equation along with $v = 1/\sqrt{L'C'}$ from the transmission line wave equations tell us that the characteristic impedance of the transmission line is

$$\begin{aligned} Z &= \frac{1}{C'v} \\ Z &= \frac{\sqrt{L'C'}}{C'} \\ Z &= \sqrt{\frac{L'}{C'}}. \end{aligned} \tag{5.13}$$

This transmission line is a waveguide with capacitance per length C' and inductance per length L', through which voltage and current waves propagate at a velocity of $v = 1/\sqrt{L'C'}$. The section time is $\tau = 1/v = \sqrt{L'C'}$ and the characteristic impedance is $Z = \sqrt{\frac{L'}{C'}}$.

5.1.2 PFN equations

A PFN is a transmission line-like power supply built using the model above. In this case, the capacitance per length is just the capacitance of the section capacitors, C, and the inductance per length is just the inductance of the segment inductors, L. For a PFN with N sections (see Fig. 5.2), the equation for the voltage in section j is

$$V_{C_j} - V_{C_{j+1}} = V_{R_j} + V_{L_j},$$

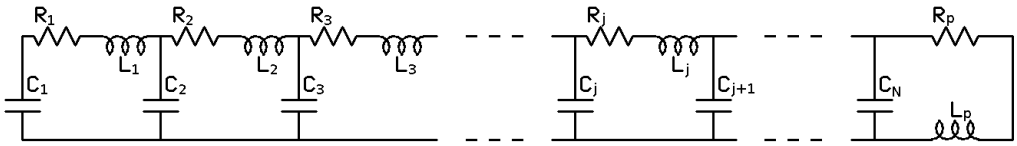

Figure 5.2: Circuit diagram of a pulse forming network with N capacitor, inductors, and resistors. In this diagram, the Nth inductor and resister correspond to the plasma, and so are labeled with a subscript p.

for $j = 1$ to $j = N - 1$. This can be rewritten

$$\frac{Q_j}{C_j} - \frac{Q_{j+1}}{C_{j+1}} = I_j R_j + L_j \frac{dI_j}{dt}. \tag{5.14}$$

For the last section, $j = N$, which includes the plasma modeled here as a resistor (R_P) and inductor (L_P) in series, the corresponding equation is

$$\frac{Q_N}{C_N} = I_P R_P + L_P \frac{dI_P}{dt}. \tag{5.15}$$

The current through the first resistor, I_1 satisfies

$$\frac{dQ_1}{dt} = I_1 \tag{5.16}$$

and the current through the jth resistor (for $j = 2$ to $j = N - 1$) satisfies

$$\frac{dQ_j}{dt} = I_{j-1} - I_j. \tag{5.17}$$

The current through the plasma, I_p, satisfies

$$\frac{dQ_N}{dt} = I_{N-1} - I_p. \tag{5.18}$$

To find the current through the plasma as a function of time we must solve this system of equations (Eqs. (5.14)–(5.18)). The numerical solution, computed in Mathematica for a 10 section PFN, is shown in Fig. 5.3.

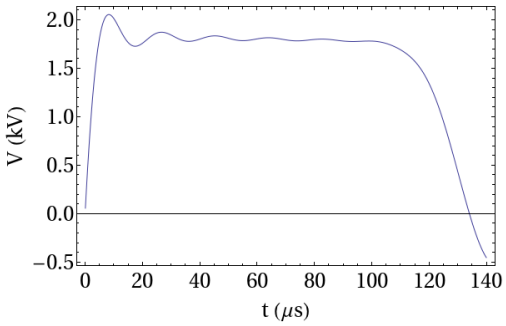

Figure 5.3: The numerical solution of Eqs. (5.14)–(5.18) for a 10 section PFN. PFN values used are $C = 120$ μF, $L = 0.3$ μH, $R = 0.3$ mΩ, with a charging voltage of 4 kV. Load resistance is matched to PFN impedance, $R = \sqrt{L/C} = 42$ mΩ. Note that the voltage pulse is approximately half the charging voltage and that the length is approximately $2 \times 10 \times \tau = 120$ μs, where $\tau = \sqrt{LC} = 6$ μs.

5.2 Design and construction

Known plasma parameters, a desired output voltage of 2–2.5 kV, and the availability of high-voltage, high-current capacitors dictated PFN design details. Our plasma jets draw a current of $I \sim 100$ kA for a voltage of $V = 2$–2.5 kV. The capacitors used are Maxwell Laboratories, Inc., castor oil capacitors with $C = 120$ μF, an effective series inductance $L = 0.03$ μH, a 10 kV maximum charging voltage, and 100 kA maximum current. To keep the current output safely under the capacitor current limit, the final PFN design uses 2 identical 5-capacitor segments arranged in parallel (Fig. 5.5).

Design parameters were based on two criteria, each discussed in detail below: impedance matching between the PFN and the plasma load, and a desired rise time of ~ 5 μs. For optimal power delivery and an output voltage of half the charging voltage, the PFN should be impedance-matched to the plasma load. The nominal plasma impedance is ~ 25 mΩ; experiments have shown that while the plasma has a resistance of ~ 2.5 mΩ, the entire circuit, including cables and ignitron, has an impedance of ~ 60 mΩ [35]. The PFN was designed to drive a load of approximately 25 mΩ; because it is composed of two parallel segments, this means a segment impedance of 50 mΩ. Transmission line theory gives a characteristic impedance of $Z = \sqrt{L/C}$, so the 50 mΩ requirement and 120 μF capacitors indicate a section inductance of

$$L = Z^2 C = (50\ \text{m}\Omega)^2\, 120\ \mu\text{F} = 0.3\ \mu\text{H}. \tag{5.19}$$

The final goal was to use the PFN with the short-duration power supply, which has a FWHM of ~ 10 μs. A ~ 5 μs rise time is short enough that the plasma has not yet decayed significantly by the time the PFN has reached full voltage. From transmission line analysis, we know that rise time is $\tau = \sqrt{LC}$; the existing

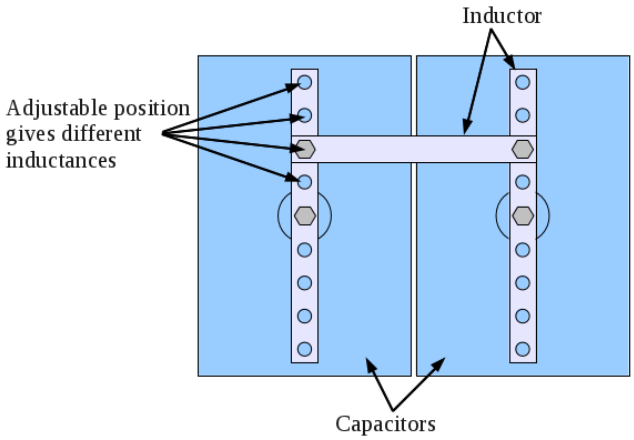

Figure 5.4: Diagram of the inductor geometry. The sketch shows a top-down view of two capacitors connected by a single inductor. The inductor is made of three independent pieces of silver-coated copper busbar. The two vertical bars in the sketch are bolted to the center pin of their respective capacitors. The cross bar can be bolted in place across the two vertical bars in 4 possible positions, each giving a slightly different inductance.

capacitors have $C = 120\ \mu$F, so a desired $\tau \sim 5\ \mu$s requires a section inductance of

$$L = \frac{\tau^2}{C} = \frac{(5\ \mu\text{s})^2}{120\ \mu\text{F}} = 0.21\ \mu\text{H}. \tag{5.20}$$

These two criteria, impedance matching (Eq. (5.19)) and rise time (Eq. (5.20)), indicate a section inductance of $L = 0.2$–$0.3\ \mu$H. This is a small inductance; a length of wire generally has an inductance of $\sim \mu$H. Metal straps are commonly used in applications requiring low inductances. The inductor choice was based on the need to ensure that the straps used to construct the inductors have a resistance that is small compared to the PFN impedance, $Z = \sqrt{L/C}/2 = 20$–$25\ \text{m}\Omega$. Resistance depends on skin depth, so our material choice requires analysis of skin depth at the two relevant timescales: the section rise time and the PFN pulse length. The skin depth is $\delta = 2\sqrt{\eta t/\mu_0}$ for a time t and material electrical resistivity η. For copper, which has an electrical resistivity of $\eta = 1.7 \times 10^{-8}\ \Omega$ m, the skin depths are $\delta = 5.2 \times 10^{-4}$ m for a timescale of 5 μs and $\delta = 1.6 \times 10^{-3}$ m for a timescale of 50 μs. The strap thickness will be of the same order as the skin depth. A width of 1 inch is standard for straps, and we know that the capacitors have a width of 8 inches. With turns, the inductor straps will be approximately a factor of two larger than this 8 inch width. This will give an approximate resistance of

$$R = \frac{\eta l}{w\delta} \sim \frac{(1.7 \times 10^{-8})(0.4)}{(.025)(1.6 \times 10^{-3})} = 0.2\ \text{m}\Omega$$

which satisfies the requirement of being small compared to the 20–25 mΩ impedance of the PFN.

Inductors between the capacitors are made of 1-inch-wide, 1/4-inch-thick silver-coated copper busbar, and were designed with each inductor comprising two parallel bars and a cross bar to allow for adjustment. A schematic diagram of the inductors is shown in Fig. 5.4, and the inductors are also visible in Fig. 5.5. To achieve the desired inductance, we installed the busbar between two capacitors and measured the inductance with the cross bar in each of the possible positions. This isolated LC circuit of two capacitors and one inductor was then inductively coupled to a driving circuit: coiled wires were placed on top of the inductor, and a square pulse sent through these wire loops by a pulse-generator caused the LC circuit of the PFN segment to ring. Inductance was estimated by measuring the frequency of the oscillations, $\omega = 1/\sqrt{LC}$, and using the known capacitance value to find L. The final arrangement has a measured inductance of $L \sim 280$ nH, giving a section rise time of $\tau = \sqrt{LC} \sim 6$ μs. The approximate resistance of the final arrangement is 0.3 mΩ.

The PFN circuit is switched by a General Electric GL-37207A size D mercury-vapor ignitron, and connected to the jet experiment electrodes with 8 Belden YK-198 low inductance coaxial cables, each about 8.5 m long. Each of the four copper clamps, based on the design of pre-existing coax clamps, connects two cables to the electrodes. These clamps are arranged to be radially symmetrically distributed between existing capacitor bank power supply connections.

Control circuitry charges the PFN with a high-voltage charging supply that uses standard 220 VAC power. Ross high-voltage relays detach the charging supply from the PFN before discharge, so that the PFN has a floating ground. A fiber optic output sends a signal when the PFN has charged to full voltage, and a fiber optic input accepts a signal from the timing system to trigger PFN discharge. The PFN control circuitry was designed and built by Dave Felt.

5.3 Testing the PFN

The PFN is approximately 0.9 m wide, 1.2 meters long, and 1.7 m high, and weighs almost a ton. The energy stored in the PFN at a 4 kV charge is equivalent to the approximate kinetic energy of a .44 magnum round, and is ten times the energy stored in the short-duration power supply at the same charging voltage. Before attaching such a large, new power supply to the spheromak experiment electrodes, a series of increasing voltage tests—initially low-voltage and eventually full-working-voltage—were performed with a specially designed dummy load.

The dummy load was built based on a previous design and had to satisfy several criteria: the metal must not heat up significantly under the energy load of the PFN, the support structure must be able to withstand any magnetic pressures from the high currents, and the inductance and resistance must be near that of the plasma.

The dummy load consists of 4 segments, each made of 8 strips of 0.003-inch-thick, 0.5-inch-wide, 1-

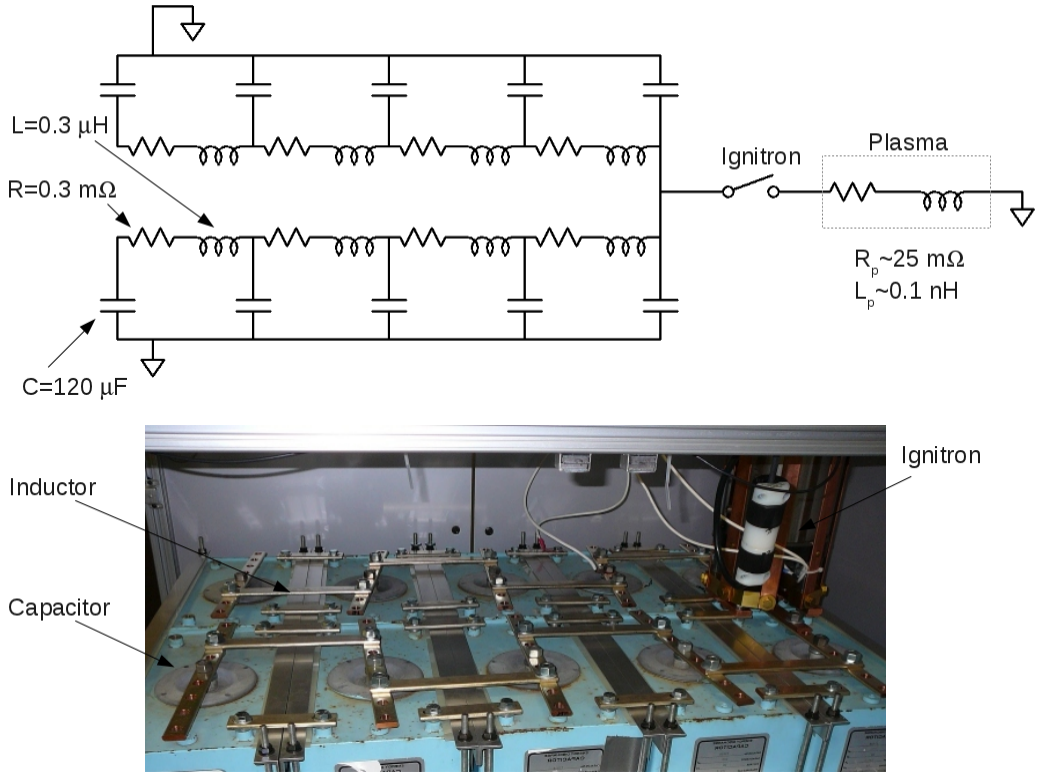

Figure 5.5: Simplified circuit diagram of the pulse forming network and corresponding photo

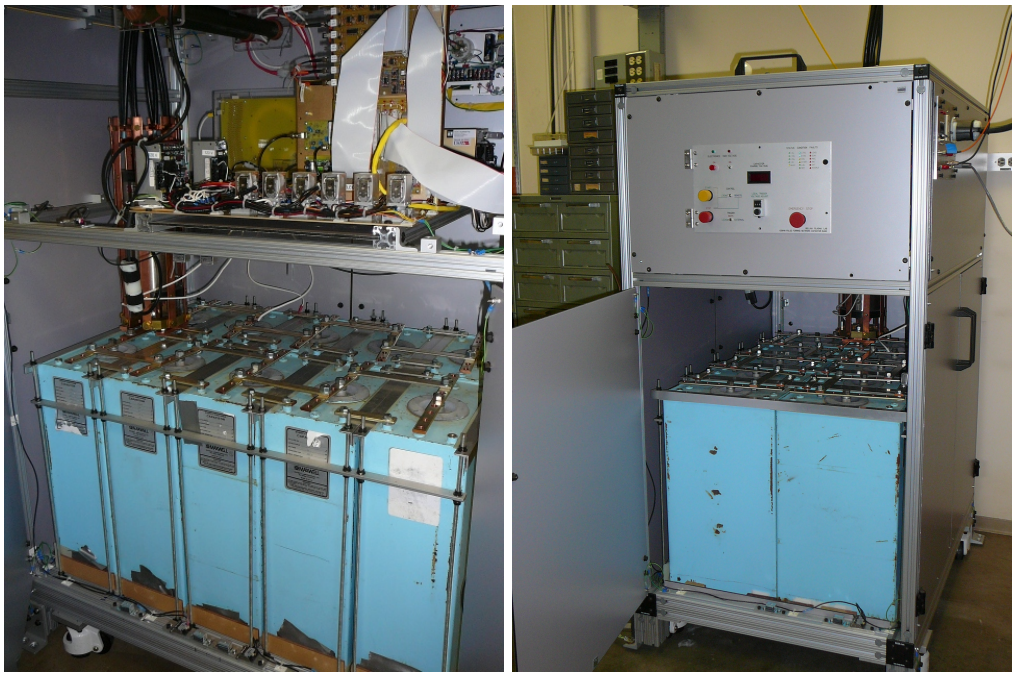

Figure 5.6: The pulse forming network in place. Left image is a side view with outer panels removed to show the capacitors, inductors, and control circuitry. Right image is a front view with lower door open to show capacitors and inductors. Also shown is the control panel, where charging voltage is set and displayed. PFN can be charged locally using this panel, or remotely with a remote control panel.

meter-long stainless steel ribbon (see Fig. 5.8). To keep inductance low, the ribbons are folded in half, with a 3-mil-thick Kapton sheet in between as electrical insulation. Each section of ribbons and Kapton is sandwiched between two pieces of 0.2-inch-thick polycarbonate, bolted together to withstand the magnetic pressure of the opposed currents in the two bends of the steel ribbon. These four segments are attached in parallel to two 10-mil-thick, 2.5-inch-wide, 24-inch-long strips of copper, which were adapted to use the cables and copper clamps designed for use on the experiment electrode.

As constructed, the dummy load has a measured inductance of $L \sim 250$ nH and a resistance of $R = 30$ mΩ, as compared to the $L \sim 35$ nH inductance and $R \sim 25$ mΩ resistance of the plasma. We tested the temperature increase in the dummy load with a 120 μF capacitor bank. Steel has a heat capacity of about $C_s \sim 0.5$ kJ/(kg K) and a density of 8000 kg/m^{-3}. The dummy load has a total mass of 250 g of steel. The temperature rise expected for the energy input of the capacitor charged to 4 kV is:

$$\Delta T = \frac{E}{C_s m} = \frac{\frac{1}{2}(120 \times 10^{-6} 4000^2}{.5 \times 10^{-3} 0.25} = 8 \text{ K}.$$

An infrared-to-mV converter measured a dummy load temperature increase of only 1 K. Heating of the metal did not appear to be a problem, even as we tested the PFN (with ten times the capacitance of this capacitor bank) up to 4 kV.

Visible and audible sparking started at a PFN charging voltage of about 2.5 kV. Fast camera images showed the sparking to be taking place not at the bolts connecting the steel ribbon to the copper, but rather between those connections and the plastic that clamped the ribbons together. The 3 mil Kapton is reported to have a dielectric strength of 5.2 kV/mil [17], more than sufficient for this application. The breakdown appeared to be not between the high voltage across the Kapton, but between the high voltage and the dielectric Kapton sheet. This is known as dielectric barrier discharge [27].

Dielectric barrier discharge occurs when the dielectric barrier between electrodes is separated from one or both of the electrodes by a gap, as we have in the dummy load connection. At sufficiently high pressures, like atmospheric pressure, there will be creation of electrons in the gap between the electrodes and the barrier, due to the electric field between the electrodes. This process, called the Townsend process, creates electrons (which cascade to create even more electrons) that are then accelerated to one side of the gap, where they build up. When a sufficiently high charge has accumulated, there will be an electrical breakdown across the gap between the barrier and the electrode. The whole process usually takes on the order of nanoseconds. The breakdown is governed by the Paschen criteria, which also governs plasma breakdown in our experiment. The minimum Paschen breakdown voltage for air is about 300 V, and corresponds to a separation of a few tens of microns. The steel ribbons do not lay flat in the region in which we saw sparking, and regions with separation of this size would not be unreasonable.

The dielectric barrier discharge breakdowns near the cable connections were reduced somewhat by filling

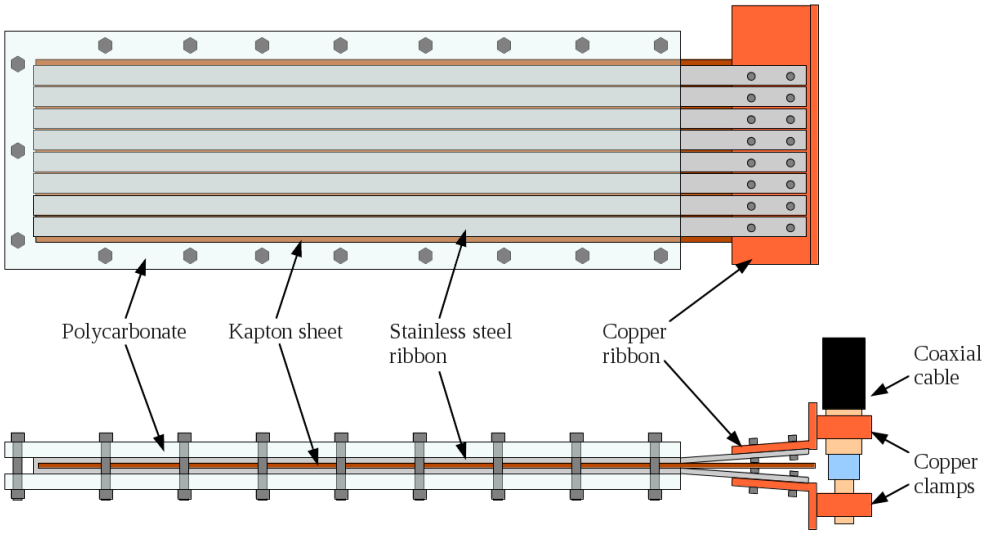

Figure 5.7: Sketch of one section of the dummy load. Top image is a top-down view of one section of the dummy load (approximately to scale), bottom image is side view (not to scale). Three additional sections would be attached in parallel to this one along the copper ribbon at right.

gaps with RTV 102 cement. Breakdowns were not eliminated entirely, because we could not fill the gaps between electrode and Kapton in the region where bolts connect the copper to steel. This kept us from testing the PFN on the dummy load at charging voltages over 4.25 kV. Nonetheless, the dummy load tests proved sufficient.

A voltage trace of PFN discharge through the dummy load is shown in Fig. 5.8. For a charging voltage of 4 kV, the voltage is slightly less than 2 kV: half the charging voltage, as expected. The slight drops in voltage at about 20 μs and 30 μs indicate dielectric barrier discharge activity. There were visible reflections of the pulse due to imperfect impedance matching between the PFN and dummy load, giving the falling side of the voltage trace a step-like appearance.

5.4 PFN-only experiments

The PFN was incorporated into the experiment in stages. First we attached the PFN cables across the electrodes and looked for interactions when generating a plasma using only the old power supply. When the connection produced no visible effect, we tried using the PFN only to break down the plasma, starting at low charging voltages. We gradually increased the charging voltage until we were making plasmas with the PFN at a charging voltage of $V = 4$ kV. The current trace is smoother than that expected from theory, using a constant L and R, Fig. 5.9.

While the ultimate goal of the PFN was to use it in concert with the existing short-duration capacitor

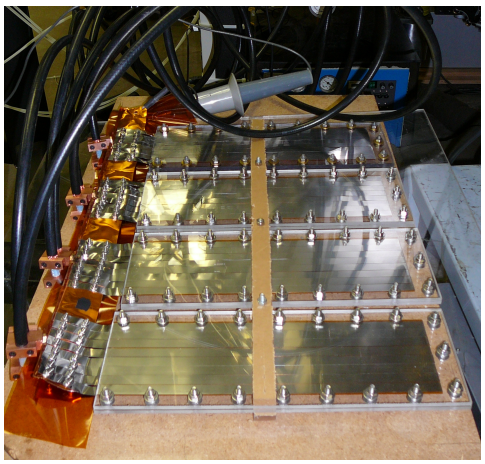

(a) The dummy load

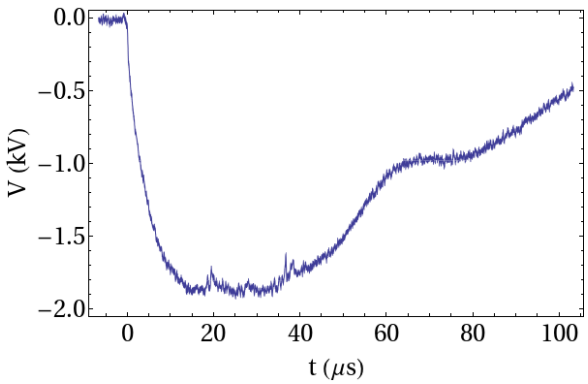

(b) Voltage trace for the PFN across the dummy load

Figure 5.8: A dummy load was designed to mimic the plasma for PFN tests. Photograph on the left is of the dummy load, attached to the PFN using the cables and clamps with which the PFN would later be attached to the experiment electrodes. Trace on the right shows the voltage across the dummy load for a PFN charging voltage of 4 kV. The voltage is slightly less than the expected 2 kV, and a reflection is visible after the primary voltage pulse. The drops in voltage seen at 20 μs, 28 μs, and 38 μs are dielectric barrier discharge activity.

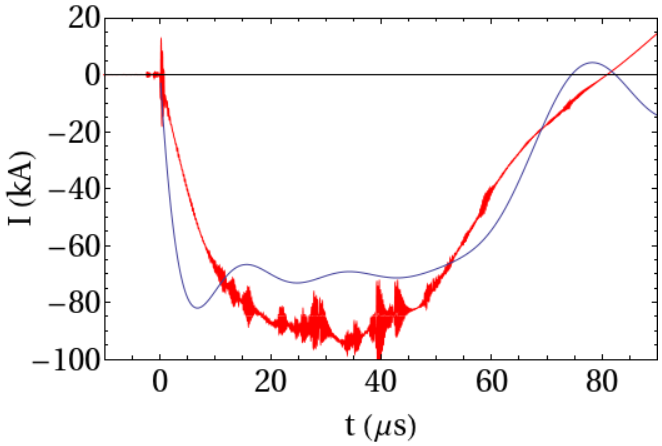

Figure 5.9: A comparison of the experimental current trace and the numerical solution. The experimental current trace (red trace) is for a charging voltage of 4 kV. The numerical solution (blue trace) uses two parallel segments of 5 capacitors each, as described in the next section. PFN values $C = 120$ μF, $L = 0.3$ μH, $R = 0.3$ mΩ, and a charging voltage of 4 kV, for plasma parameters $L_p = 265$ nH and $R_p = 62.5$ mΩ. These "plasma" values include the approximate inductance and resistance of the cables and ignitron in addition to the plasma.

bank power supply, we did perform approximately 350 experiments using only the PFN for plasma generation. Fig. 5.10 shows a comparison between fast camera images of a straight hydrogen jet produced with just the short-duration power supply and similar time images of a hydrogen jet produced with just the PFN. In general, plasma jets produced with the PFN are dimmer, more diffuse, and initially travel at a lower velocity than jets produced with the short-duration power supply.

As expected, plasma jets produced with the PFN do grow to a longer length than the short-duration power supply plasma jets; the significantly longer current pulse compensates for the initially slower velocity. Visible structure in fast camera images lasts for approximately the first 25–30 μs after plasma breakdown. Images show that the plasma front has extended to at least $z \sim 75$–80 cm by this time. Measurements made with the z axis magnetic probe array show that the jet front reaches the last channel, at $z = 66.5$ cm, at about time $t = 17.5$ μs, indicating an average velocity of 38 km/s. Maintaining this average velocity would suggest a final length of $\sim$ 100 cm at $t \sim 25$–30 μs. For comparison, a jet produced with just the short-duration capacitor bank reaches a length of 35–40 cm, as can be estimated from both fast camera images and magnetic data. Magnetic data from the z axis MPA shows that at 10 μs after plasma breakdown, when structure is beginning to fade, the jet front has reached channel 7 at $z = 40.5$ cm.

After $t \sim 30$ μs, no distinct structure is visible, but interferometer measurements of hydrogen jets indicate the presence of plasma at later times (Fig. 5.11). The slower velocity of the PFN jets is clear in both the fast camera images of Fig. 5.10 and interferometer measurements of Fig. 5.11. The leading edge of the interferometer signal indicates the time-of-flight for the jet front to reach the interferometer chord at $z = 29$ cm. The difference in the arrival time of the two jets shows the velocity of the short-duration power supply jet velocity, $v \sim 48$ km/s, to be about 1.5 times that of the PFN plasma jet, $v \sim 29$ km/s. The difference in velocity is due to the significantly longer rise time of the PFN current. This slowly rising current means that the current amplitude is much lower in the formation and launching stage of the jet, and a lower current means less toroidal field pressure to drive the jet.

The longer rise time/lower current amplitude also explains the difference in collimation between the plasma jets. The central column is visually more diffuse in PFN jets than it is in short-duration power supply jets, as seen in Fig. 5.10. The peak line-integrated density of PFN plasma jets is less than that in short-duration power supply experiments by a small numerical factor, a factor of about 2 in the examples shown in Fig. 5.11. Approximately the same amount of material is present in the jet column in each case, but the lower current means a smaller toroidal magnetic field to pinch the plasma column, and so the same amount of material is spread out in a larger-diameter, more-diffuse column. We can see that at later times, when the PFN current has increased, the PFN jet has become more collimated. The late-time ($t \sim 15$–30 μs) hydrogen jets have a more well-defined structure when produced with just the PFN than with the two power supplies together, as the current amplitude in the PFN-only case is larger in this time period. For a

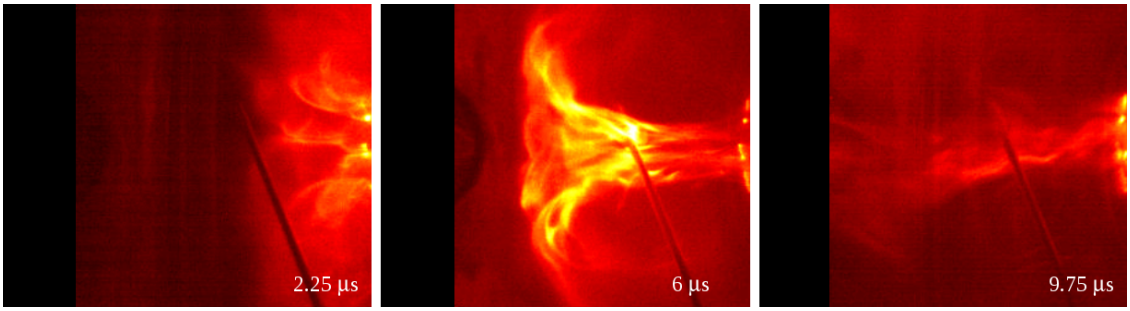

(a) Hydrogen plasma jet produced with short-duration power supply

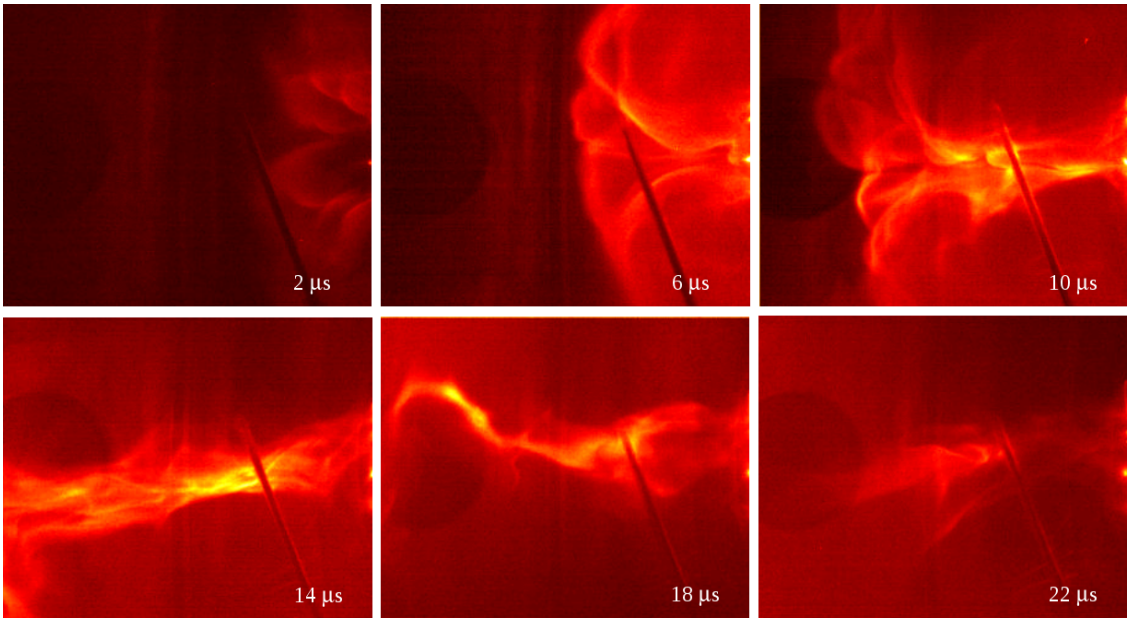

(b) Hydrogen plasma jet produced with PFN only

Figure 5.10: Comparison between hydrogen jet made with short-duration power supply (top) and with PFN only (bottom)

more detailed discussion of how a fluctuating current amplitude can affect the column width, see discussion in Chapter 4.

5.5 Experiments with both power supplies

The short-duration power supply provides a current pulse with a rise time of only $\sim$ 2–3 μs, and has a FWHM of only $\sim$ 10 μs. The pulse-forming network has a rise time of $\sim$ 5–10 μs, and a FWHM of $\sim$ 50 μs. We can use the two power supplies in concert and take advantage of the benefits of each (Fig. 5.12). The short-duration power supply is discharged first, for plasma breakdown; the PFN is discharged at the time of plasma breakdown, and reaches its peak current value starting at about the time the short-duration power

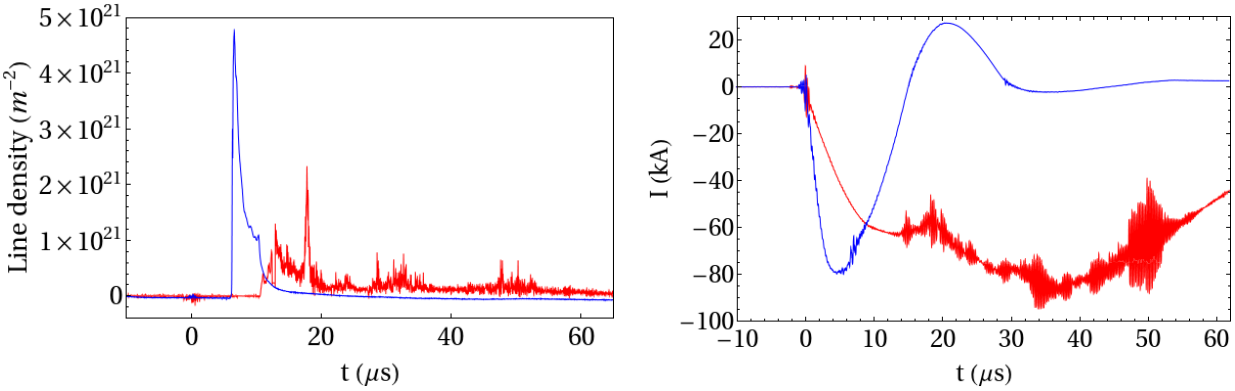

(a) Line-integrated density

(b) Current

Figure 5.11: Comparison between short-duration power supply and PFN. (a) Line-integrated density as a function of time. These data are from the HeNe laser interferometer built by Deepak Kumar (see Appendix A.2 for more details). The blue trace shows the density for a hydrogen plasma jet with the short-duration power supply (shot # 8153) and the red trace shows the density for a hydrogen plasma jet with the PFN. The density drops to zero relatively quickly in the short-duration case, but is sustained at a low level for tens of microseconds in the PFN case. The offset in the arrival of the peak density indicates that the jet produced by the short-duration power supply travels at a higher velocity, this is due to the longer rise time of the current in the PFN. (b) Current as a function of time for the same two plasma shots, again blue indicates short-duration power supply and red indicates PFN. Note that the longer rise time of the PFN means that, although peak current values are approximately the same, the current is significantly lower in the jet formation and launching time interval, leading to a slower-moving jet. Current traces shown here were smoothed using a running average over 15 data points. The power supply charging voltages were $V = 5.5$ kV for shot # 8153 (short-duration) and $V = 4$ kV for shot # 10127 (PFN).

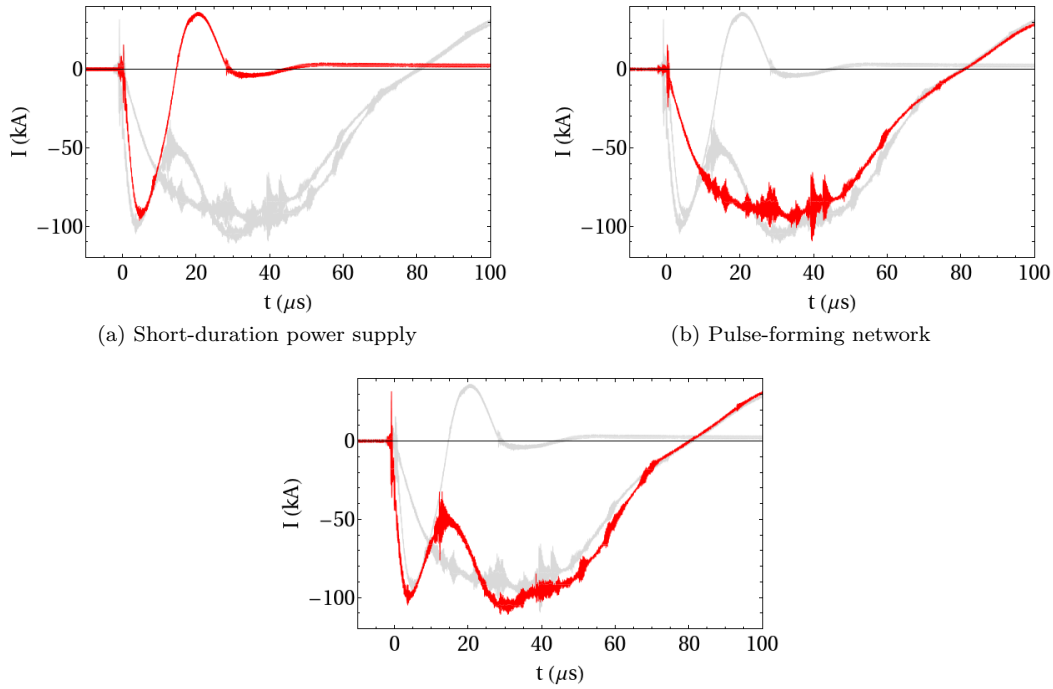

(a) Short-duration power supply

(b) Pulse-forming network

(c) Both power supplies together

Figure 5.12: Current traces of various power supply configurations. Each plot shows a single configuration current trace in red, and with the other two configurations shown in light gray for comparison. (a) Short-duration capacitor bank power supply current trace (shot #8908), (b) long-duration PFN power supply current trace (shot #10085), and (c) both power supplies used together (shot #10801). All current traces are from hydrogen experiments with power supply charging voltages $V_{CB} = 5$ kV and $V_{PFN} = 4$ kV, and a bias field setting of $V_{bias} = 200$ V.

supply current has dropped to zero. We therefore get the fast rise time of the short-duration power supply, and the longer time duration of the PFN. The combined power supply current pulse has a FWHM of ~ 60 μs, about 6 times the length of the current pulse from the short-duration power supply.

The extended current duration allowed us to see several new plasma behaviors. Most significantly, it allowed us to identify the instability cascade leading to magnetic reconnection described in Chapter 2. In addition we observed the behavior of the straight jet radius in response to a fluctuating current amplitude, the "breathing" behavior described in Chapter 4. Also observed for the first time after addition of the PFN was a kink-unstable plasma jet with two twists, as described in the next section.

5.6 Kink instability with two twists

With the addition of the PFN, we observed for the first time kink-unstable plasmas exhibiting two twists (see Fig. 5.13). This behavior is rare, seen only once in hydrogen plasma and in $\sim 4\%$ of argon plasmas in the relevant parameter range. In hydrogen plasma, the two twists were seen using the PFN without the short-

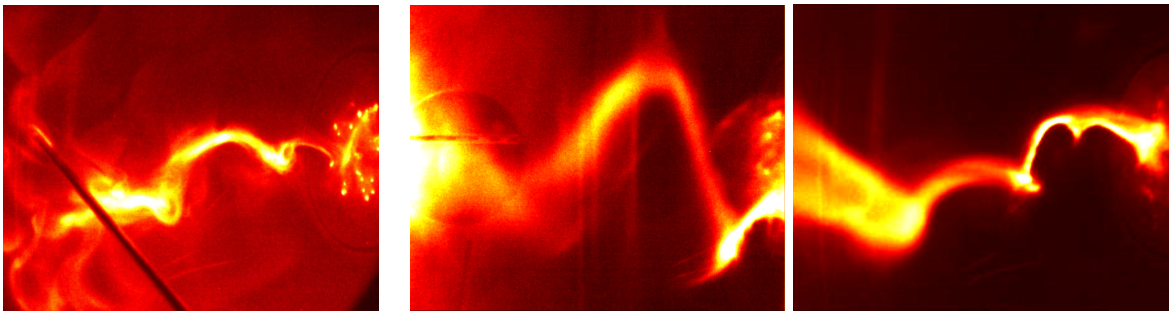

(a) Hydrogen, PFN only

(b) Argon, both power supplies

Figure 5.13: Fast camera images showing double-twist kink plasma jets. (a) A hydrogen jet formed using the PFN only. Two twists appear simultaneously. (b) Argon jets formed using both power supplies. One twist forms and moves with the jet away from the electrodes; a second smaller radius twist forms later, closer to the electrodes. Argon jets with two twists develop Rayleigh–Taylor instabilities later in time (the beginnings of Rayleigh–Taylor fine structure is visible in both cases argon jets shown here).

duration capacitor bank (see Fig. 5.13a). In argon plasma the two twists were seen with the short-duration capacitor bank for breakdown and the PFN for sustainment (see Fig. 5.13b). It should be noted that no experiments using only the PFN have been performed with argon, and relatively few have been performed using both power supplies with hydrogen. No double twists have been observed in nitrogen thus far, but many fewer nitrogen experiments have been performed than hydrogen or argon experiments.

In the hydrogen case, the plasma column becomes kink-unstable and the two twists appear simultaneously. In contrast, in most cases the argon plasma column appears to become kink-unstable and develop one twist. A second twist appears near the electrode at low z at a later time as the first twist translates in z. In only one argon double-twist example do the two twists appear to onset simultaneously, as in the hydrogen case. All double twists observed in argon experiments precede Rayleigh–Taylor instability formation (see Chapter 2 for more details on Rayleigh–Taylor instabilities).

The onset of the hydrogen double kink shown in Fig. 5.13a is consistent with the Kruskal–Shafronov kink instability onset criteria, using the column length rather than the kink wavelength as the value of ℓ. At time of kink-onset, $t = 13$ μs, the current is $I = 48$ kA and the flux is $\Psi = 1.62$ mWb, giving $\alpha = 37.2$. This implies that the column should be kink-unstable for $\ell > 33.75$ cm, and indeed the jet length is estimated to be about 33 cm at time of kink onset.

Chapter 6

Summary

This thesis reported the results of three sets of plasma experiments performed with the Caltech spheromak experimental apparatus. The three distinct topics are united as variations on a similar theme: the deformation of magnetically driven collimated plasma jets.

The magnetic reconnection experiments discussed in Chapter 2 demonstrate a new and unexpected behavior: the ideal MHD plasma undergoes a current-driven kink instability which then drives a finer-scale Rayleigh–Taylor instability. When growth of the Rayleigh–Taylor instability thins the plasma column to the necessary "microscopic" length scale, the plasma undergoes magnetic reconnection. Fast camera images clearly show the large-scale helical plasma jet developing the periodic fine-scale structure of the Rayleigh–Taylor instability, and show the plasma column breaking after Rayleigh–Taylor growth. The topology change of the magnetized structure indicates magnetic reconnection, and is accompanied by additional signatures of reconnection. This three-dimensional cascade of instabilities links the large scale of an MHD plasma system and the comparatively microscopic scale of the magnetic reconnection process, allowing the ideal MHD system to undergo reconnection. Magnetic reconnection underlies the dynamical evolution of plasma systems from tokamak fusion experiments to solar coronal loops, and the way in which large-scale MHD plasmas bridge the gap in length scales to access the microscale physics has been a topic of study for years. These results demonstrate one possible process by which this can be accomplished.

Collision experiments described in Chapter 3 were originally motivated by the interactions between collimated astrophysical jets and their surrounding media, but provide results that may also be of interest in laboratory experiments in which plasmas interact with neutral particles. In these experiments we studied the interaction between a plasma jet and neutral gas cloud with a combination of fast camera images, spectroscopic measurements, and magnetic measurements. We found that a hydrogen jet will deform upon collision with an argon (or nitrogen) neutral gas cloud, "piling up" as the front of the jet slows and the jet material behind it catches up. The density and magnetic field both increase in the pile-up region, but as the jet velocity does not transition from above to below the ion acoustic nor Alfvén velocities, no shock

wave is produced. An argon jet colliding with a hydrogen neutral gas cloud will also slow, but not enough to produce an observable pile-up. Instead, the argon jet acts like a piston, launching a shock wave into the hydrogen neutral cloud.

Use of a short-duration power supply for plasma breakdown together with a long-duration power supply for plasma sustainment supplies the experiment with a current whose amplitude fluctuates in time. Chapter 4 shows that this fluctuating amplitude causes a "breathing" mode in a straight plasma jet: the plasma column expands and contracts radially, and this disturbance travels along the jet. The radius is found to scale with current amplitude as $r \sim I^{-1}$, consistent with an assumption of two-dimensional compression.

A new pulse forming network (PFN) capacitor bank power supply is the long-duration power supply used in the "breathing" mode experiments in Chapter 4 and the magnetic reconnection studies presented in Chapter 2. Some of the details of the design and construction of the PFN were presented in Chapter 5. As shown in Chapter 5, the PFN extends the time duration of the plasma experiment five fold, a feature essential to the discovery of these new behaviors.

Appendix A

Caltech experimental apparatus

A brief overview of the experimental apparatus and diagnostic tools was given in Section 1.4. This appendix gives a more detailed description of plasma generation and diagnostic hardware that is helpful, but not strictly necessary, for understanding the work presented in this thesis. This includes equipment newly constructed and installed as part of this thesis research: the pulse forming network (PFN) power supply, the z-axis magnetic probe array, and the capacitively coupled probe.

A.1 Plasma generation hardware

The Caltech spheromak formation experiment uses a novel, coplanar, concentric electrode arrangement that enables direct observations of the early steps in the spheromak formation process, and matches accretion disk boundary conditions. The electrodes are 1/4-inch-thick copper, the cathode a 20.3-cm-diameter disk, and the anode a 50.8-cm-diameter annulus (see Fig. A.1). The anode is at chamber ground, and a ceramic break at the cathode mounting point isolates the cathode from ground. The two electrodes are separated by a 6.35 mm gap, but no electric breakdown occurs in this gap, as there is not enough gas density to satisfy the Paschen breakdown criteria [4]. The electrodes are mounted on one end of a 1.48-m-diameter, 1.58-m-long, cylindrical stainless steel vacuum chamber, as shown in Fig. A.1. The dimensions of the chamber are such that the ~ 25 cm plasma evolves with minimal wall interactions.

Our pulsed power system allows us to build up stored energy relatively slowly (~ 10 seconds) and then release it quickly ($\sim 10^{-6}$ seconds), achieving peak powers in the 100 megawatt range for total energies in the kilojoule range. The Caltech experiment uses two different pulsed power supplies: a short-duration capacitor bank power supply and a long-duration pulse forming network power supply.

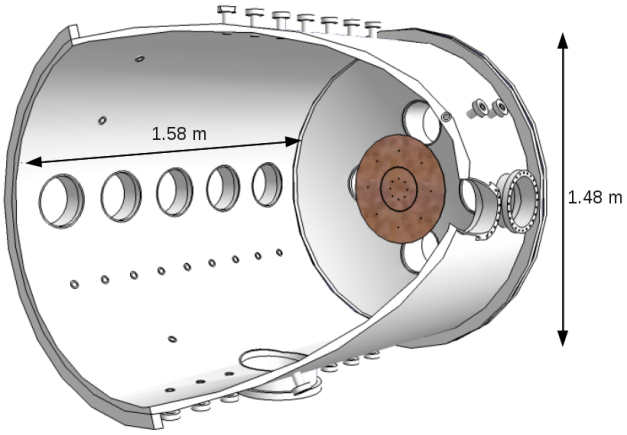

Figure A.1: A cut-through diagram of the experimental vacuum chamber, showing a view of the inner cathode and outer electrode mounted on one end dome. Numerous ports and windows allow diagnostic access.

A.1.1 Capacitor bank

The short-duration capacitor bank power supply provides the energy to break neutral gas down into a plasma. The 120 μF capacitor bank uses two 60 μF Aerovox Industries, Inc., capacitors, each switched by a GL-7703 size A mercury-vapor ignitron. Four Belden YK-198 low-inductance coaxial cables connect the capacitor bank across the electrodes. The capacitor bank provides a sinusoidal current trace, with a peak current of $\sim$ 100 kA for a 5 kV charging voltage and a full-width at half-maximum of $\sim$ 10 μs. The rise time is $\sim$ 3 μs.

A.1.2 Pulse forming network

The long-duration pulse forming network (PFN) can be used alone to break the neutral gas down into plasma, or together with the short-duration power supply. In the latter case, the short-duration power supply is used for breakdown and the PFN is discharged post-breakdown for sustainment. The PFN uses 10 Maxwell Laboratories, Inc., 120 μF capacitors connected with 0.3 μH inductors, and is switched by a General Electric GL-37207A size D ignitron. The PFN provides a roughly square pulse with a $\sim$ 100 kA peak current for a 4 kV charging voltage, and has a $\sim$ 50 μs FWHM. The nominal rise time is $\sim$ 7 μs. See Chapter 5 for more about the pulse forming network theory and design.

A.1.3 Bias magnetic field coil

A magnetic field coil mounted outside the chamber directly behind the electrodes produces a background magnetic field, that is, a magnetic field not produced by currents in the plasma itself. The background magnetic field is also called the bias field or vacuum magnetic field (and often "stuffing flux" in spheromak literature). The coil has an inner diameter of 13 cm, an outer diameter of 18.5 cm, and a total of 110 turns.

A small capacitor bank provides current to the coil; the relationship between the capacitor bank charging voltage and the magnetic flux through the inner electrode is $\Psi = 0.01 V_{bias}$ mWb/V. The bias field capacitor bank is fired 10 ms before the main capacitor bank, as this is the time required for the magnetic field to diffuse through the steel wall of the chamber and the copper electrodes. The bias field strength changes on a scale of milliseconds, and so is effectively constant over the tens of microseconds of the experiment.

A.1.4 Fast gas valves

Four fast gas valves provide the neutral gas for plasma formation. The valves use an aluminum gasket held in place by a spring to let in a measured amount of gas. A pulsed current in a coil produces an image current in the aluminum gasket, opening the volume of the valve to the gas line that connects it to the experiment. Adjusting the charging voltage of the capacitor bank that provides the pulsed current or changing the gas pressure gives rough control over the amount of neutral gas input, which is $\sim 10^{19}$ particles for a single gas valve. See Appendix B for more information on measuring the neutral gas density. The gas valves are arranged with each valve feeding 4 gas inlets: inner left and inner right, and outer left and outer right. This arrangement allows two different gases on the inner electrode and outer electrode, or the left and right sides.

A.1.5 Sidegas valve

A sidegas valve installed for collision experiments is visible in Fig. A.4. The fast gas valve that provides the neutral gas is of the same type used to provide gas for plasma breakdown at the electrodes, and is plumbed to allow use of any of the available gases. The sidegas uses gas system "B" and so can be independent of the gas used for a single species plasma. The valve is mounted on the side of the experimental chamber and delivers the neutral gas via a 1/4-inch-diameter stainless steel tube passing through a 1/4 inch compression port, at $z = 44$ cm from the electrodes. A 1/4-inch-diameter quartz tube connects to the stainless steel via Swagelok, and the open end of the quartz tube bends 90° to deliver gas towards the oncoming jet, directly on the z-axis. The tube end is at $z = 39$ cm and the neutral gas cloud diameter $\sim$ 10–15 cm, so the plasma jet forms completely and reaches a length of $\sim$ 25 cm before interacting with the neutral cloud.

A.2 Diagnostic hardware

A.2.1 Data acquisition

Most of the data are recorded by an array of fast digital data acquisition recorders. A VME crate houses 12 digital data acquisition (DAQ) boards (each with 8 channels), a clock module board, and a VME sequencer board. The DAQ boards are Struck Innovative Systeme model SIS3300, with 12-bit resolution and a sampling frequency of 100 MHz. The clock module is Struck Innovative Systeme model SIS3820, with 32 channels

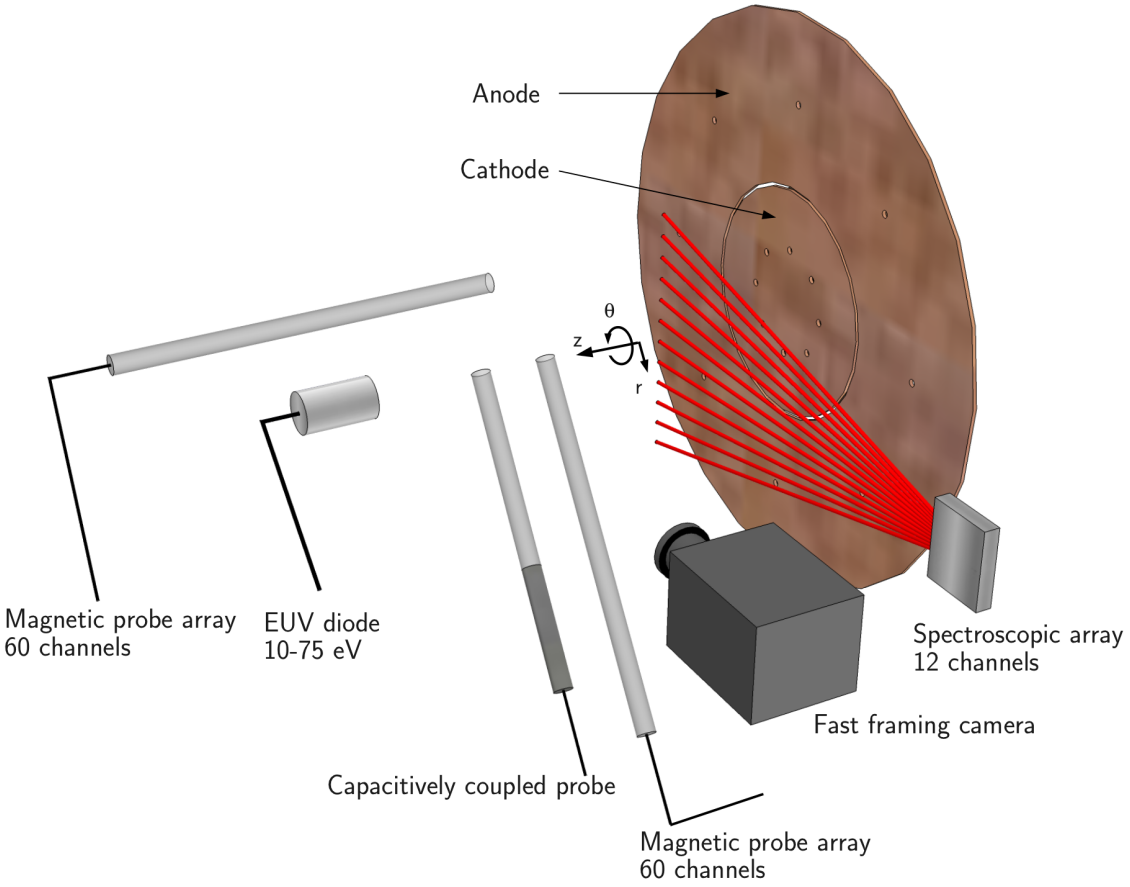

Figure A.2: An overview of some of the diagnostics, with a cutaway view of the electrodes. Not to scale

that send stop and start signals to the DAQ channels. Once initiated by an external signal from the control system, data are continuously acquired until the clock module receives a stop command from the timing system. The system is controlled by an IDL code that manages the timing and then reads and stores the experimental data.

A.2.2 Fast framing camera

A fast camera helps diagnose plasma behavior by providing visible spectrum images of plasma morphology, and in particular by allowing us to construct movies of plasma evolution. We currently use an Imacon 200 ultra-high-speed camera manufactured by DRS Technologies. The Imacon camera uses 8 CCDs that each record a 1360×1024 pixel image two times over the course of the experiment, giving a total of 16 frames. The minimum exposure time and minimum interframe time is 5 ns; a required 200 ns between exposures of an individual CCD gives an interframe time of about 25 ns, so that the Imacon can make a 16 frame movie spanning as little as 375 ns, or an 8 frame movie spanning just over 35 ns. When used with optical filters, the Imacon allows us to image specific wavelengths of visible light. This means that in the case of a two-element plasma we can use different filters to separate the behavior of each element (e.g. hydrogen and argon).

A.2.3 Rogowski coil

A hand-wound Rogowski coil measures the current flowing between the electrodes. The coil encircles the inner electrode, fitting just inside the 12 copper clamps that attach the two power supplies to the outer electrode. A passive integrator circuit between the coil and the VME data acquisition integrates the signal to give current, though calibration shows it gives a slight deviation from true signal at late times [66].

A.2.4 High-voltage probe

A Tektronix P6013A high-voltage probe measures the voltage across the electrodes. The probe has a rise time of 7 ns and measures voltages up to 12 kV, outputting a 1000× attenuated signal. Probe output impedance of 1 MΩ requires a buffer circuit to step down to the 50 Ω input requirement of the VME data acquisition system. The buffer circuit ground connects to VME (and hence chamber) ground; to avoid a ground loop, we never use the high-voltage probe ground clip, connecting the main voltage clip to the experiment inner electrode.

A.2.5 R-axis magnetic probe array

We measure the magnetic field vector at 20 different r locations with an r-axis magnetic probe array (MPA) designed and built by Carlos Romero–Talamás [56, 55]. The probe can be moved to different z-locations. The 60-channel probe array uses commercially available inductor chips to measure the time-changing magnetic field; the measured voltages are multiplied by the experimentally determined calibration constants and numerically integrated to give the magnetic field. See Appendix C for more information on MPA calibration.

A.2.6 Spectroscopic array

A gated 12-channel spectroscopic system, developed by Gunsu Yun, allows spectroscopic measurements with control over the resolution in both space and time [66]. The 12 channels are arranged linearly and span approximately 22 cm when focused on the plasma from the chamber side window. Gating gives us a time window adjustable in both location in time and time duration. The minimum time window allowing sufficient signal was found by Gunsu Yun to be ~ 0.3 μs, but a time of 1–3 μs is most common. Most results presented here use a time window of 3 μs. The spectroscopic array measures emission in the range 250 nm to 500 nm. The lower limit is determined by transmission of the chamber window and lenses used; the spectrometer range extends down to 200 nm. Spectrometer resolution varies with wavelength but is approximately picometers per pixel. This high resolution allows us to measure velocity via Doppler shifts, to estimate temperature via Doppler broadening, and in some cases to measure density via Stark broadening.

A.2.7 Interferometer

A heterodyne He–Ne laser interferometer, developed by Deepak Kumar, measures the line-integrated particle density at $z = 29$ cm [33, 32]. The interferometer has unequal path lengths, which sets it apart from most interferometers used in plasma experiments. This design allows much simpler setup and alignment.

A.2.8 Extreme ultraviolet-soft X-ray diodes

An array of 4 extreme ultraviolet-soft X-ray (EUV) diodes detect radiation in the 10–2000 eV energy range. The diodes are International Radiation Detectors, Inc., model AXUV-HS5, approximately 1 mm square and with a rise time of 0.7 ns. Three of the 4 diodes have thin metal foil filters to limit the detected energy range. In order of increasing energy range transmitted, these filters are: 50-nm-thick titanium, 200-nm-thick aluminum, and 500-nm-thick titanium. The 50-nm-thick titanium is extremely delicate, and was ruined after only a handful of experiments using both power supplies. The 500 nm titanium only transmits above ~ 150 eV, and thus far plasmas in the Caltech experiment have not been seen to emit at such a high energy. The 200 nm aluminum filter transmits in the $\sim$ 15–75 eV energy range, with a fairly constant transmission level

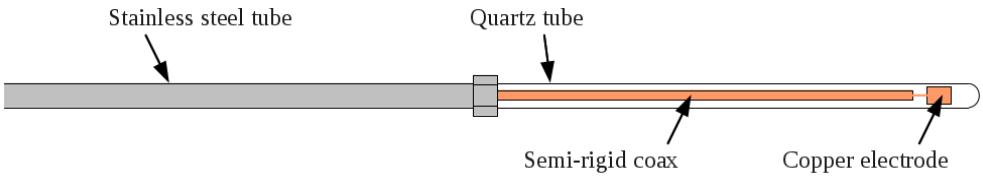

Figure A.3: A sketch of the capacitively coupled probe. Not to scale

in that range. (The diodes detect an energy range that spans EUV and soft X-ray, however the boundary between soft X-ray and extreme ultraviolet is usually defined to be at 124 eV, hence these diodes serve as EUV diodes in this experiment.)

A.2.9 Capacitively coupled probe

A capacitively coupled probe is an electrostatic probe separated from the plasma via insulating material. We built an electrostatic probe out of a 90.5 cm length of copper-jacketed, 3.6-mm-outer-diameter, semi-rigid coaxial cable. The semi-rigid coax has a 3.15-mm-diameter, 4-mm-long copper electrode soldered to the end of the inner conductor. A quartz tube with 1/4 inch outer diameter covers the final 45 cm of the probe, insulating it from direct contact with the plasma (see Fig. A.3). Torr seal vacuum epoxy joins the quartz tube to a standard Swagelok fitting, which connects to a 48-cm-long stainless steel tube inserted into the chamber through a 1/4 inch compression port. The installed probe is visible in the chamber in Fig. A.4. The probe is connected to a Tektronix TDS 3034B, 300 MHz oscilloscope, with a small isolation transformer in place to prevent ground loops.

The capacitively coupled probe measures electrostatic fluctuations at $z = 29$ cm from the electrodes. A fast Fourier transform of the probe data gives the frequency spectrum. Used with the plasma density and magnetic field strength, the frequency can determine the type of wave excited by determining the position in the CMA diagram, as explained in greater detail in Chapter 2.

A.2.10 Z-axis magnetic probe array

A second magnetic probe array (MPA) was built, in part to study the jet deformation over the course of a single collision experiment. The new MPA measures the time-changing magnetic field at 20 locations along the z-axis and can be moved in r. The design follows that of the r-axis MPA closely [56, 55], with adjustments to accommodate for the difference in geometry and improvements based on difficulties encountered in the r-axis probe construction and maintenance. These adjustments proved successful in design of the MPA on the solar experiment. A wider-diameter pipe was used for the 90° bend for ease of maneuvering the thin wires, the form with embedded inductor chips was not wrapped in a protective layer, and a slightly wider

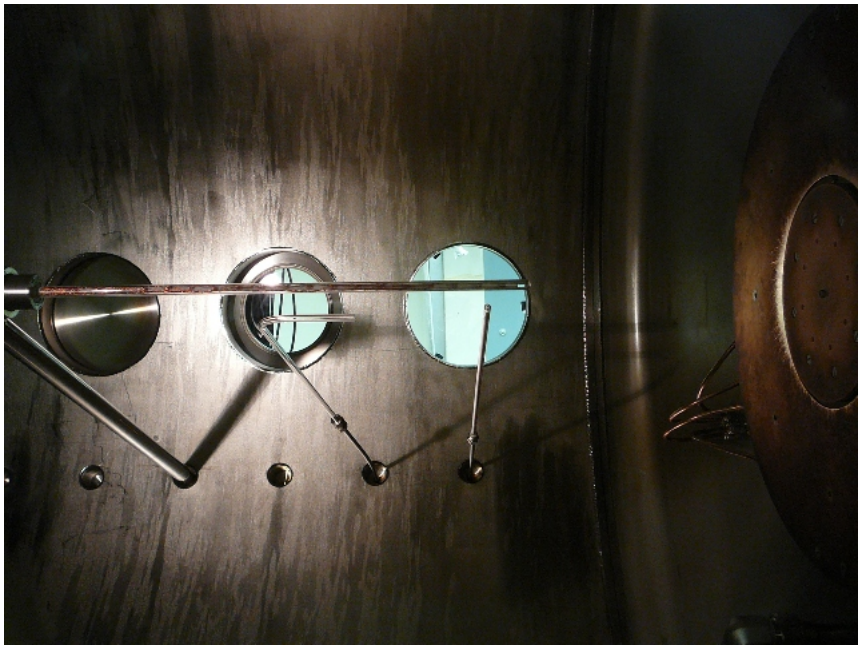

Figure A.4: The z-axis magnetic probe array (MPA) in place in the chamber. The experiment electrodes are visible on the far right; the bent quartz tube that delivers a neutral gas cloud for collision experiments and the capacitively coupled probe are also visible.

quartz tube was used to keep it from rubbing and possibly dislodging chips. The z-axis MPA is mounted on the fourth small vacuum port on the vacuum chamber west side, at $z = 75$ cm. Measurement channels are spaced 2 cm apart, with channel 1 at $z = 28.5$ cm and channel 20 at $z = 66.5$ cm. The r position of the MPA adjusts from a radius of $r \sim 70$ to the chamber center at $r = 0$ and an additional 10 cm past the center. Interference with the sidegas (first port) and capacitively coupled probe (second port) determine the maximum r position of the MPA in the current setup, as seen in Fig. A.4. Each channel consists of a commercially available inductor chip. The inductor chips, manufactured by Coilcraft, Inc., are small (2.8 mm $\times$ 2.9 mm $\times$ 2.00 mm), ~ 50 turn coils with an inductance of ~ 5 μH. Use of pre-made chips requires experimental measurement of the coil calibration factor. Calibration of the z-axis MPA was performed in situ, after installation. See Appendix C for details of the calibration process.

A.3 Control hardware

The fast time scales ($\sim$ microseconds) involved in the experiments require computer-controlled power supply discharging and diagnostic timing. For safety reasons, electrical control signals are converted to fiber optic signals, so that the control equipment is electrically isolated from high voltages. Two Berkeley Nucleonics Corporation model 565 pulse/delay generators are used to control experimental timing. Each unit has 8

channels, each channel sends a square voltage pulse to a lab-built pulse-doubler. The pulse-doubler both converts the electrical signal to an optical signal and doubles the number of pulses; it sends one optical trigger signal at the time determined by the input square pulse rising edge and a second optical trigger signal at the time determined by the input square pulse falling edge, giving a total of 16 timing channels per pulse doubler. One pulse/delay generator and associated pulse doubler controls the trigger time of all steps in the plasma formation (bias magnetic field, gas valves, power supplies) and the second pulse/delay generator and associated pulse doubler controls diagnostic equipment timing. The zero time of the diagnostic pulse/delay generator is set by plasma breakdown. A fiber optic cable and collimator lens pointed at one of the inner electrode gas inlets trigger the system from the light at first plasma breakdown.

Safe grounding is a concern in pulsed circuits. Due to the short time scale and large, time-changing currents, there can be significant voltages on parts of the experiment that are "grounded". Equipment must be grounded with care, as multiple connections to ground can form a closed loop. High-amplitude currents changing on a fast time scale generate time-changing magnetic flux through the closed loop, which can produce large induced voltages. This can make measurements inaccurate and can damage equipment, and so diagnostics are designed to be electrically isolated.

In the Caltech experiment, the power supplies disconnect from wall ground after charging and before discharging, and so have a "floating" ground for the duration of the experiment. Fiber optic signals isolate control equipment, as described above, and diagnostic equipment often connects to data acquisition equipment via isolation transformers.

Appendix B

Neutral gas density measurements

This appendix describes the hardware and method used to measure neutral gas density and corrects an error in previous measurements. The new measured value is confirmed via comparison to other measurement methods.

B.1 Fast ion gauge (FIG)

The fast ion gauge is a custom-built hot-cathode gauge that measures the neutral gas density. A negatively biased electrode is heated until it emits thermionic electrons, which are accelerated towards a positively biased electrode (Fig. B.1). As the electrons travel from the cathode to the anode, they interact with neutral gas particles, ionizing these initially neutral particles so that the number of ions produced is related to the number density of neutral particles present. The ions are attracted to a grounded collector electrode. By measuring the emission current I_e and the collector current I_c, the neutral gas pressure P can be calculated:

$$P = \frac{I_c}{I_e S R_g},$$

where S is the gauge sensitivity factor for air (or N_2) and R_g is the relative sensitivity factor of the gas being measured; the ideal gas law $P = nkT$ is then used to determine the particle density n. The relative sensitivity factor R_g is relative to air, and values can be looked up in commonly available charts [49]. The gauge sensitivity factor S can be determined by calibration, as described in the next section. This design allows measurement of neutral gas density as a function of time.

B.2 Calibration process

In situ, absolute calibration of the FIG provides a calibration factor $S = V_s/(I_e P)$. The calibration factor S relates the measured signal voltage (which is the collector current I_c measured across a resistor) and the

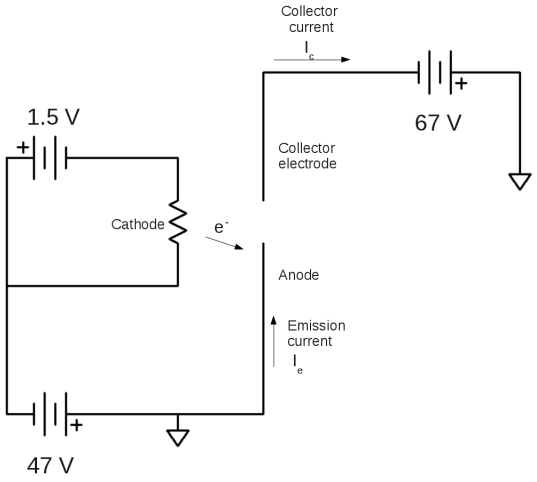

(a) Simplified FIG circuit diagram

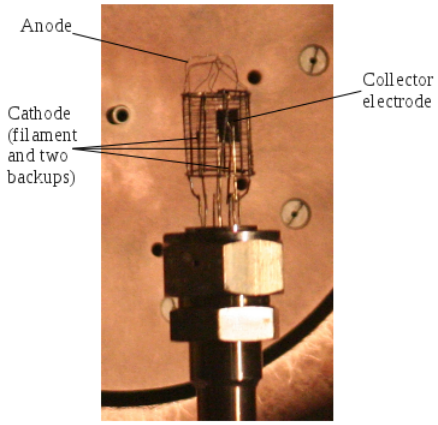

(b) Image of the FIG in place

Figure B.1: The fast ion gauge in schematic circuit diagram and constructed form

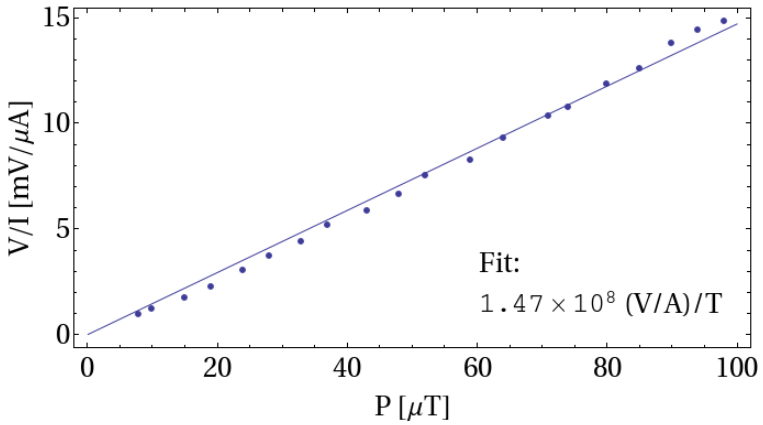

Figure B.2: Calibration of the FIG in situ. Points are measured values, line gives the calibration constant.

emission current I_e to the chamber pressure P, as measured by a commercial ion gauge. The ion gauge is a standard Bayard–Alpert type gauge [49], CHA Industries Ion Tube type IG 100K, used with a Granville-Phillips 307 Ion Gauge Controller. To perform the calibration, the gate valve between the cryo pump and the experimental chamber is closed so that the chamber pressure rises from $\sim 2 \times 10^{-7}$ T to $\sim 10^{-4}$ T over the course of approximately one hour. The signal voltage and emission current are recorded at different pressure values as the pressure slowly rises; the slope of the linear fit to these data gives the calibration constant for air, in our case $S = 1.5 \times 10^8$ (V/A)/T (Figure B.2).

The calibration was performed multiple times, once for each of several setups tested. The resulting calibration constants are within a numerical factor of each other; all are about two orders of magnitude off from the calibration constant from a previous calibration performed in the test chamber in 2004. The

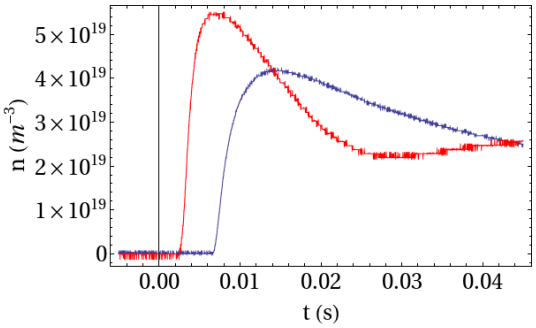

Figure B.3: Comparison between nitrogen at the electrodes (red trace) and nitrogen at the sidegas valve (blue trace)

difference may be attributable to a change in the filament surface over the years, to the difference in the measurement setup (lab notebooks indicate use of a multimeter in place of a oscilloscope for one of the measured values, and use of the test chamber in place of the main chamber), or to some unknown effect (perhaps adjustment of the probe during relocation from test chamber to experimental chamber).

B.3 FIG measurements of gas distribution

The FIG was used to measure the neutral density in front of the sidegas valve. The first measurement of sidegas neutral density used nitrogen, to enable comparison with measurements of nitrogen made at the electrodes. As seen in Fig. B.3, the nitrogen trace (neutral gas density as a function of time) measured in front of the sidegas has a slightly different shape (starts later in time, peak offset more from initial rise) but the same magnitude as a measurement made in front of an electrode gas inlet with a single gas valve fired using the same backline gas pressure and the same power supply.

Later measurements used argon, as that is the gas most often used in collision experiments. The neutral density in argon is calculated as described in Section B.1 above, then is divided by the sensitivity factor for argon ($R_{g,Ar} = 1.2$) taken from a published table of relative sensitivities for Bayard-Alpert gauges [49]. The argon measurements used the same capacitor bank used to pulse the sidegas valve and outer electrode fast gas valves in plasma experiments. The capacitor bank was charged to 400 V and a backline gas pressure of 75 PSI was used, the voltage and the pressure used most often in experiments.

Figure B.4a shows the dependence of density on z position. These data are from $t = 16$ ms after gas valve firing, the standard time between sidegas firing and plasma breakdown, and hence the relevant time for determining the density of the neutral cloud when impacted by the plasma jet. The gas inlet of the sidegas is at $z = 39$ cm. The line shown is a d^{-2} fit, where d is the distance from the gas inlet. The gas cloud has a Gaussian form $n \sim \exp{(r-\mu)^2/2\sigma^2}$ in the radial direction (Fig. B.4b) with $\sigma = \frac{2}{3}d$, where d is the distance

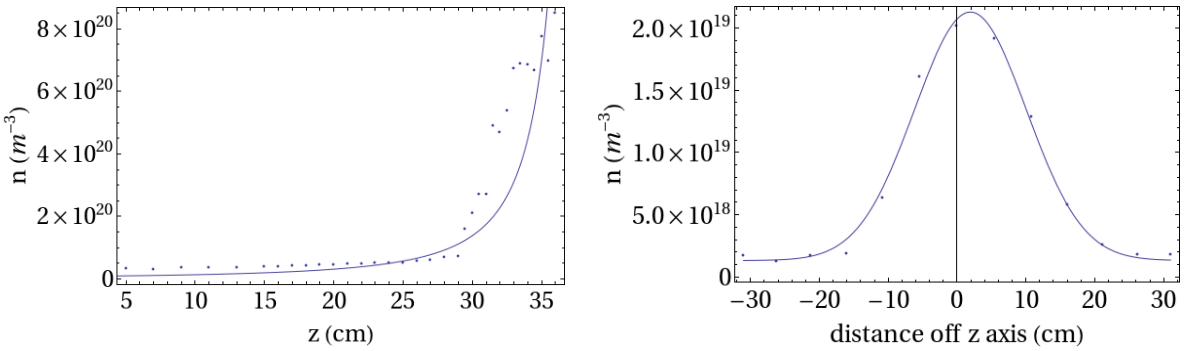

(a) Density axial profile

(b) Density radial profile

Figure B.4: (a) The axial density profile 16 ms after firing. (b) The density profile $d = 12$ cm from the gas valve ($z = 27$ cm) at 16 ms after firing. Line shows Gaussian fit, with center at 1.9 cm and $\sigma = 8.1 \sim \frac{2}{3}d$. Fit shown corresponds to $n(d) = 1.1 \times 10^{18}(d)^{-2}$, where d is distance from the gas inlet in m.

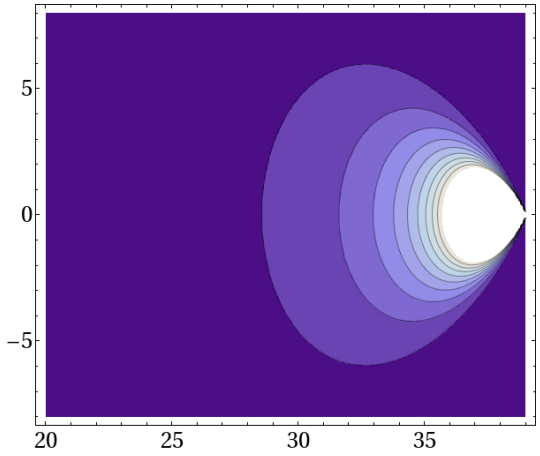

Figure B.5: Density contour plot of the Ar sidegas cloud, with contour lines from 1–10 $\times 10^{20}$ m^{-3}

from the gas inlet, and $\mu \sim 2$ cm off from center (a perfectly centered gas cloud would have $\mu = 0$). If we combine these, we get the contour density plot seen in Fig. B.5. The gas inlet is at the right of the image and the contour lines shown are 1–10 $\times 10^{20}$ m^{-3}.

B.4 Comparison with other measurements

Because the measured neutral gas densities were $\sim 10^2$ times higher than previously reported, it was desirable to confirm the values via comparison to other measurements.

B.4.1 Thermocouple vacuum gauge

A thermocouple vacuum gauge uses a hot filament and thermocouple temperature sensor to measure gas properties and so determine vacuum pressures in the milliTorr to Torr range. The vacuum chamber has a Varian type 0531 thermocouple mounted on a bottom port at the end of the chamber opposite the electrodes and sidegas. The thermocouple responds slowly and measures a steady pressure. The FIG responds quickly and measures a time-changing density. The two are not directly related, but they can be correlated.

For comparison purposes, we will consider the total particle number N input by a gas puff from a single fast gas valve. To start, we should keep in mind the total number of argon particles in the internal volume, or plenum, of the fast gas valve, as this provides an upper bound on the total number of particles in a single puff of gas. For a fast gas valve at a backline pressure of 75 PSI and using room temperature $T \sim \frac{1}{40}$ eV and a plenum volume of 2.3 cm^{-3}, the total number of particles is:

$$N_{plenum} = \frac{P\,V_{plenum}}{k\,T} = \frac{(75 \times 6895 + 101325)(2.3 \times 10^{-6})}{1.6 \times 10^{-19} \times \frac{1}{40}} = 3.5 \times 10^{20} \text{ particles.}$$

The following measurements used the same settings as the argon sidegas measurement discussed above. With the gate valve closed a single puff of argon gas from the sidegas valve raises the pressure in the chamber to 0.25 mT, as measured by the thermocouple. This gives a total number of particles in the chamber

$$N_{TC} = \frac{P\,V_{chamber}}{k\,T} = \frac{(0.25 \times 10^{-3} \times 133.3)(0.7^2\pi\,1.6)}{1.6 \times 10^{-19} \times \frac{1}{40}} = 2 \times 10^{19} \text{ particles.}$$

There are two ways to relate this value to the measurements made by the FIG.

The first method is to allow a long time window on the FIG measurement so that at late times the FIG-measured value asymptotically approaches the steady pressure measured by the thermocouple. With the gate valve closed, at late time ($t \sim 0.8$ s) the FIG-measured density has reached a steady $n = 6.7 \times 10^{18}$ m^{-3} (Fig. B.6). This gives a total number of particles in the chamber

$$N_{asymp} = nV_{chamber} = 6.7 \times 10^{18}(0.7^2\pi\,1.6) = 1.6 \times 10^{19} \text{ particles.}$$

This value is less than the upper bound provided by the total number of particles in the fast gas valve plenum, and is close to the number of particles in the chamber as measured by the thermocouple.

The second method is to assume that the gas travels at a constant velocity and then use the time-changing FIG density measurement to estimate the particle flux. The particle flux can then be integrated to estimate the total particle input.

Particle flux through an area A is $F = Avn$. To calculate the flux we assume that the argon gas enters the chamber at thermal velocity, $v \sim 200$ m/s, and that the gas cloud spreads out from the gas inlet in a

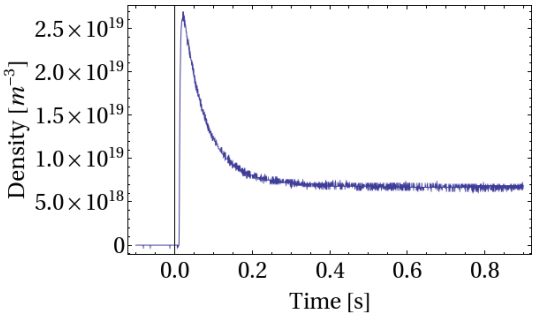

Figure B.6: A single puff of argon gas at 75 PSI in the sidegas valve, with the gate valve closed

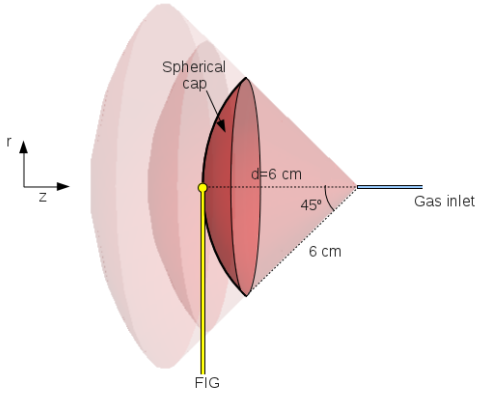

(a) The surface area used for calculating flux

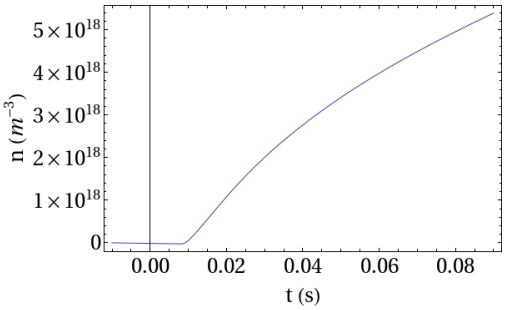

(b) Plot of total particle number N as a function of time

Figure B.7: The flux is calculated assuming that the value measured at $d = 12$ cm is constant over the spherical cap within 45° of the z axis and thermal velocity of 200 km/s. Plot shows total particles as a function of time, using the measurement at $z = 12$ cm and assuming $v = 200$. The half peak value of n is reached at 0.08 s; this is also approximately where the slope changes to become linearly increasing, corresponding to integration of the equilibrated pressure.

cone with an angle of 45° from the z axis (Fig. B.7a). We will choose the FIG measurement made at $d = 12$ cm from the gas inlet, and assume that the density measured at that distance is constant over the area of a spherical cap at 12 cm from the gas inlet. This spherical cap surface area, multiplied by the thermal velocity multiplied by the particle density measured by the FIG, gives the flux into the chamber. Time-integrating the flux gives the total particle input:

$$
\begin{aligned}
N_{flux} &= \int Av\, n(t)\, dt \\
&= Av \int n(t)\, dt \\
&= \left(\int_0^{2\pi} d\phi \int_0^{\pi/4} (0.06)^2 \sin\theta d\theta \right) \int_0^{0.1} 200\, n(t)\, dt \\
&= 3.5 \times 10^{18} \text{ particles.}
\end{aligned}
$$

This value is also less than the upper bound provided by the total number of particles in the fast gas valve plenum, and is less than, but close to, the number of particles in the chamber as measured by the thermocouple.

The three values of N—$N_{TC} = 2 \times 10^{19}$ particles calculated from the thermocouple measurement, $N_{asymp} = 1.6 \times 10^{19}$ particles calculated from the asymptotic value of the FIG measurement, and $N_{flux} = 3.5 \times 10^{18}$ particles calculated from the particle flux at $d = 6$ cm—are all of the same order, $\sim 10^{19}$. This value is also consistent with the upper bound on the total number of particles in the plenum, $N_{plenum} = 3.5 \times 10^{20}$ particles. It should be noted that although these measurements show $\sim 1/20$ of the particles in the plenum entering the chamber, similar measurements of hydrogen gas indicate that a larger fraction of the hydrogen particles enter the chamber.

B.4.2 Paschen breakdown

An independent order of magnitude calculation of the necessary neutral density can be performed by noting that the Paschen criteria must be met at plasma breakdown [4]. The Paschen curve shows breakdown voltage as a function of Pd, the pressure multiplied by the distance. We know from past experiments that plasma breakdown in hydrogen can happen in our experiment at a voltage as low as 2 kV. Using the Paschen breakdown curve for H_2 (Fig. B.8), we can see that this value of breakdown voltage corresponds to $Pd \sim 1$ T cm and $Pd \sim 60$ T cm. The path length of a single spiderleg just after breakdown is ~ 10 cm, which implies a necessary pressure of $\frac{1}{10}$ T $< P <$ $\frac{60}{10}$ T, or, using $n = P/kT$ at room temperature, a particle density of

$$2.5 \times 10^{19} \text{ m}^{-3} < n < 1.5 \times 10^{21} \text{ m}^{-3}.$$

The neutral density value used for the Caltech experiment in the past is $n \sim 10^{17}$ m^{-3}, which implies $Pd \sim 4 \times 10^{-3}$ T cm, a value too small to be represented on the Paschen curve shown in Fig. B.8. Although only providing an order of magnitude estimate, the Paschen breakdown analysis method allows us to see that the previously used density value would require an unattainably high voltage for plasma breakdown.

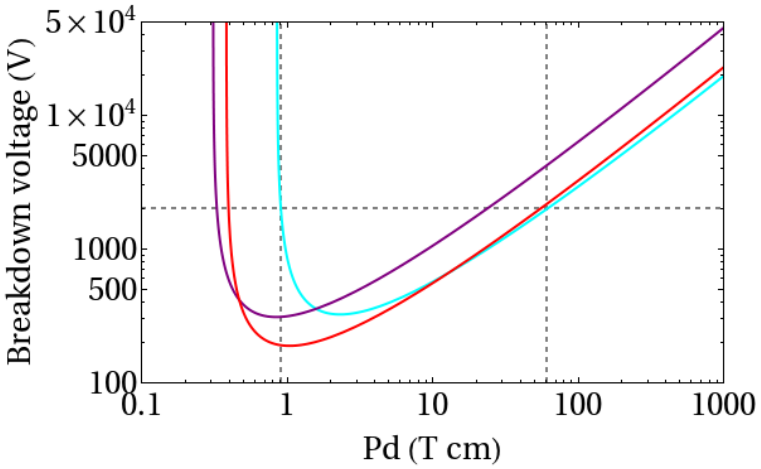

Figure B.8: Paschen curves showing voltage required for breakdown as a function of the pressure times the distance. The horizontal dashed gray line indicates 2 kV, the lowest breakdown voltage confirmed for H_2 in our experiment. Vertical dashed gray lines indicate possible Pd values based on the intersection of this horizontal line with the H_2 Paschen curve. The Pd values imply a possible density range of $\sim 10^{19-21}$ m^{-3}.

Appendix C

Magnetic probe array (MPA) calibration

The experimental chamber currently has 3 magnetic probe arrays: a 12-channel array on the solar side, and both a 60-channel r-axis array and a 60-channel z-axis array on the spheromak side. The probes are calibrated in place at initial installation, and then again in the case of replacement of the outer quartz tube (or any other change that could alter alignment). The general method is described in Romero–Talamás [56], but an assumption made in that calculation makes the calibration accurate only when the coils are near alignment with system axes. A more exact calibration is presented here.

The MPA measures the time-changing magnetic field using Faraday's law. For each coil, we measure

$$V_{coil} = -\frac{d\Phi}{dt} = -NA\left(\frac{dB_{measured}}{dt}\right)$$

$$\frac{dB_{measured}}{dt} = \frac{V_{coil}}{-NA} \tag{C.1}$$

$$B_{measured} = \frac{1}{-NA}\int V_{coil}dt \tag{C.2}$$

where N is the number of turns in the coil and A is the area of the coil, both unknown in the case of our commercial inductor chips. We can calibrate the MPA using a known magnetic field to calculate the compound calibration constant NA. For our known field, we use a specially designed and constructed Helmholtz coil with n turns of radius a, through which we run a current I (see Fig. C.1). We know that the field in the center of the Helmholtz coil is

$$B_{applied} = \left(\frac{4}{5}\right)^{3/2}\frac{\mu_0 nI}{a},$$

so that the time-changing magnetic field is

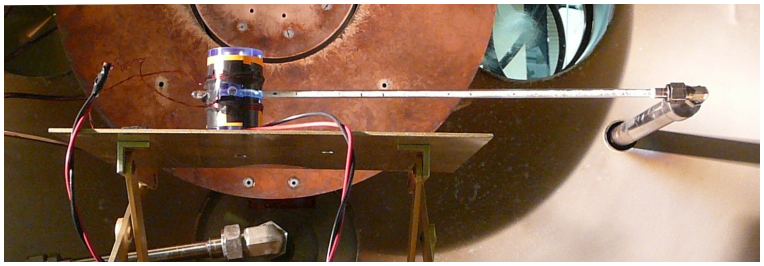

Figure C.1: A photo showing the Helmholtz coil being used to calibrate the r axis MPA. The Helmholtz coil is wound on a solid, 2-inch-radius acrylic cylinder. Three holes drilled in the cylinder intersect at the center of the coil, allowing the Helmholtz coil to be centered on the small inductor coil of interest. For example, in this image the ϕ coil is being calibrated; the quartz tube of the probe passes through the coil so that the magnetic field is in the appropriate direction (vertical in this image), and the other axis directions drilled in the acrylic give lines of sight to allow centering (one in the cylinder top and the other visible on the cylinder front). The Helmholtz coil is supported by a jack to prevent coil motion or breaking of the MPA quartz tube covering.

$$\frac{dB_{applied}}{dt} = \left(\frac{4}{5}\right)^{3/2} \frac{\mu_0 n}{a} \frac{dI}{dt}. \tag{C.3}$$

Equating $dB_{measured}/dt$ (Eq. (C.1)) and $dB_{applied}/dt$ (Eq. (C.3)) gives us

$$\left(\frac{4}{5}\right)^{3/2} \frac{\mu_0 n}{a} \frac{dI}{dt} = \frac{V_{coil}}{-NA}.$$

We can rearrange, integrate, and then solve for the calibration constant NA:

$$\begin{aligned} NA\left(\frac{dI}{dt}\right) &= -\frac{aV_{coil}}{\left(\frac{4}{5}\right)^{3/2}\mu_0 n} \\ NA\int dI &= -\frac{a}{\left(\frac{4}{5}\right)^{3/2}\mu_0 n}\int V_{coil}dt \\ NA &= -\frac{a}{\left(\frac{4}{5}\right)^{3/2}\mu_0 n}\frac{\int V_{coil}dt}{\int dI}. \end{aligned} \tag{C.4}$$

If the coils were perfectly aligned along the r, θ, and z axes, it would be sufficient to calculate the calibration constant NA according to Eq. (C.4) for each coil. However, the coils are not necessarily perfectly aligned along the r, θ, and z axes. This means that, for example, a field applied purely in the z direction should be measured only by the "z" coil, but misalignment of coils may cause a signal to be measured in the "r" and "θ" coils. To correctly measure the field we must construct a calibration constant matrix $\mathbb{C}$ for

which $\mathbf{B}_{applied} = \mathbb{C}\mathbf{B}_{measured}$. The value of $\mathbb{C}$ given in Romero–Talamás is

$$\mathbb{C} = \begin{pmatrix} 1 & -C_{r\theta} & -C_{rz} \\ -C_{\theta r} & 1 & -C_{\theta z} \\ -C_{zr} & -C_{z\theta} & 1 \end{pmatrix} \tag{C.5}$$

with the components C_{ij} defined as

$$C_{ij} = \frac{NA_j^{perp}}{NA_i}$$

and using $B_{measured} = -1/NA \int V_{coil} dt$ as given in Eq. (C.2). This calibration matrix is sufficient for coils nearly aligned with the axes. Coils far out of alignment require a more exact calibration matrix. The form of the exact calibration matrix is much more complicated, but can be used for any alignment of the coils with respect to the axes, as long as the three coil directions are linearly independent, so that they form a basis.

For clarity, we will work with a calibration matrix $\mathbb{M}$ that includes NA explicitly. This means that rather than the equation used by Romero–Talamás, $\mathbf{B}_{applied} = \mathbb{C}\mathbf{B}_{measured}$, we will instead use $\mathbf{B}_{applied} = \mathbb{M}\mathbf{A}$, where A_j is just the integrated voltage measured in the coil aligned with the j axis,

$$A_j = \int V_{coil,j} dt, \qquad \text{so} \qquad \mathbf{A} = \begin{pmatrix} \int V_{coil,r} dt \\ \int V_{coil,\theta} dt \\ \int V_{coil,z} dt \end{pmatrix}. \tag{C.6}$$

First, note that $\mathbb{M}^{-1}\mathbf{B}_{applied} = \mathbf{A}$. The vector $\mathbf{A}$ is measured and $B_{applied}$ is known, so we can construct $\mathbb{M}^{-1}$. We construct $\mathbb{M}^{-1}$ by first applying a known field in a single axial direction, say $\mathbf{B}_{applied} = B_z \hat{z}$. This gives us

$$\mathbb{M}^{-1}\mathbf{B}_{applied} = \mathbb{M}^{-1} B_z \hat{z} \tag{C.7}$$

$$= \begin{pmatrix} -M_{rr}^{-1} & -M_{r\theta}^{-1} & -M_{rz}^{-1} \\ -M_{\theta r}^{-1} & -M_{\theta\theta}^{-1} & -M_{\theta z}^{-1} \\ -M_{zr}^{-1} & -M_{z\theta}^{-1} & -M_{zz}^{-1} \end{pmatrix} \begin{pmatrix} 0 \\ 0 \\ B_z \end{pmatrix} \tag{C.8}$$

$$= \begin{pmatrix} M_{rz}^{-1} B_z \\ M_{\theta z}^{-1} B_z \\ M_{zz}^{-1} B_z \end{pmatrix}. \tag{C.9}$$

Equating this with **A** (Eq. (C.6)) gives:

$$\begin{pmatrix} M_{rz}^{-1} B_z \\ M_{\theta z}^{-1} B_z \\ M_{zz}^{-1} B_z \end{pmatrix} = \begin{pmatrix} \int V_r^z dt \\ \int V_\theta^z dt \\ \int V_z^z dt \end{pmatrix}. \tag{C.10}$$

Subscripts in the voltage integrals specify the coil direction and superscripts in the voltage integrals specify the applied field direction. We know the value of the applied field B_z, and so can solve for each of the three components M_{iz}^{-1} in terms of known quantities:

$$\begin{aligned} M_{iz}^{-1} &= \frac{1}{B_z} \int V_i^z dt \\ &= \left(\frac{5}{4}\right)^{3/2} \frac{a}{\mu_0 n \int_{t_1}^{t_2} I_z dt} \int_{t_1}^{t_2} V_i^z dt \\ &= \left(\frac{5}{4}\right)^{3/2} \frac{a}{\mu_0 n \Delta I_z} \int_{t_1}^{t_2} V_i^z dt \end{aligned}$$

where $\Delta I_z = I_z(t_2) - I_z(t_1)$. We can repeat this process twice more, using a field applied only in the r direction and then only the θ direction. This gives us M_{ir} and $M_{i\theta}$, thereby constructing the inverse of the calibration matrix $\mathbb{M}^{-1}$.

$$\mathbb{M}^{-1} = \left(\frac{5}{4}\right)^{3/2} \frac{a}{\mu_0 n} \begin{pmatrix} \frac{1}{\Delta I_r} \int_{t_1}^{t_2} V_r^r dt & \frac{1}{\Delta I_\theta} \int_{t_1}^{t_2} V_r^\theta dt & \frac{1}{\Delta I_z} \int_{t_1}^{t_2} V_r^z dt \\ \frac{1}{\Delta I_r} \int_{t_1}^{t_2} V_\theta^r dt & \frac{1}{\Delta I_\theta} \int_{t_1}^{t_2} V_\theta^\theta dt & \frac{1}{\Delta I_z} \int_{t_1}^{t_2} V_\theta^z dt \\ \frac{1}{\Delta I_r} \int_{t_1}^{t_2} V_z^r dt & \frac{1}{\Delta I_\theta} \int_{t_1}^{t_2} V_z^\theta dt & \frac{1}{\Delta I_z} \int_{t_1}^{t_2} V_z^z dt \end{pmatrix}$$

We can then invert $\mathbb{M}^{-1}$ to get the calibration matrix $\mathbb{M}$. Note that $\mathbb{M}^{-1}$ is a change-of-basis matrix and hence is guaranteed to be invertible. We perform each measurement three times and average the measured M_{ij}^{-1} values, and this process is repeated for each of the 60 channels. Note that calibrating an MPA requires $3 \times N$ measurements, or 180 for the 60-channel spheromak MPA.

The difference in the calibration values depends on the alignment of the channels. The closer the r, θ, and z coils are to being correctly aligned with the r, θ, and z axes, the closer the Romero–Talamás values are to the values in the matrix given above. However, the plastic fixture housing the coils tends to rotate slightly with the tightening of the Swagelok fitting that seals the outer quartz tube, making it difficult to ensure the correct alignment.

We can compare the matrices yielded by the two methods by using the measurements from a calibration performed in 2009. These matrices are for channel one of the r-axis MPA; $\mathbb{M}_M$ is the matrix generated using the process described here and $\mathbb{M}_{R-T}$ is the matrix generated using the method described by Romero–

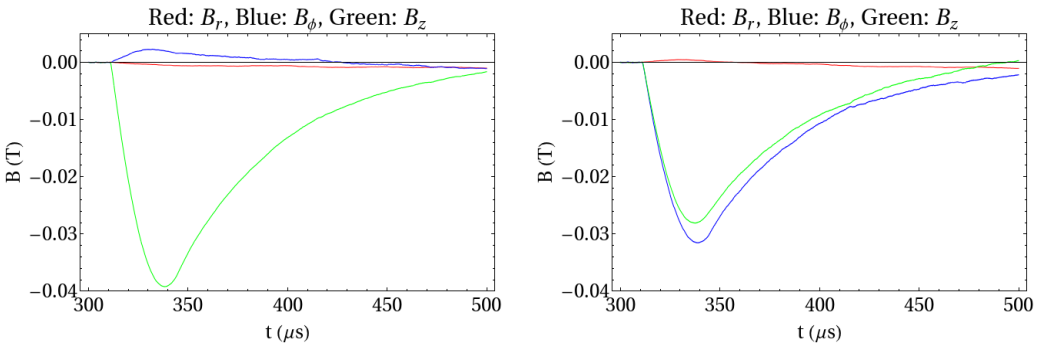

(a) Magnetic traces using calibration matrix $\mathbb{M}_M$ (b) Magnetic traces using calibration matrix $\mathbb{M}_{R-T}$

Figure C.2: Left-hand plot shows the three components of the magnetic field using the calibration method described above, right-hand plot uses Romero–Talamás's calibration matrix. The magnetic field was applied in the z direction with a Helmholtz coil used for calibration; the field should be entirely in the z direction.

Talamás (an adjusted version of $\mathbb{C}$ (Eq. (C.5)) that includes NA so that the matrix is that which would be multiplied by the same vector):

$$\mathbb{M}_M = \begin{pmatrix} -9050.71 & -58.76 & -86.52 \\ -527.85 & 7048.44 & 4201.28 \\ 200.16 & 4230.34 & -8932.68 \end{pmatrix} \quad \& \quad \mathbb{M}_{R-T} = \begin{pmatrix} -9057.43 & 434.63 & 408.79 \\ 99.62 & 9042.86 & -4280.29 \\ -65.16 & -6834. & -11457.1 \end{pmatrix}.$$

For a magnetic field applied in only the z direction using the calibration Helmholtz coils, these matrices give the measured magnetic fields plotted in Fig. C.2. The total field strength in each case is shown compared to the field calculated from the current measured in the Helmholtz coil as shown in Fig. C.3. We see that the total field strength is about the same in each case, but that when the coils are not aligned with axes the method described in Romero–Talamás gives $B_\phi \sim B_z$ for an applied $\mathbf{B} = B_z\hat{z}$, whereas this method gives the desired $B \sim B_z \gg B_\phi$.

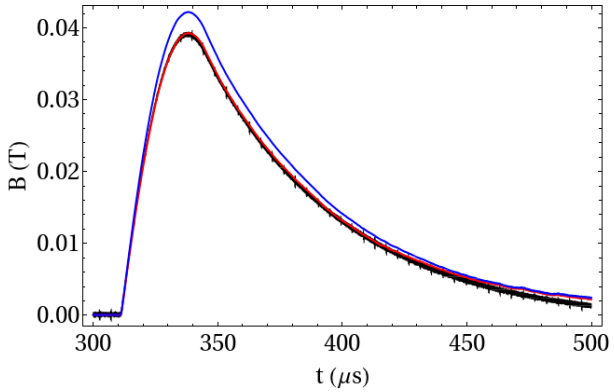

Figure C.3: The total magnetic field using each of the two calibration matrix methods. The red and blue traces show the total field calculated from the traces shown in Fig. C.2; the red using the calibration method described above and blue using the calibration method described in Romero–Talamás. The black trace shows the field calculated from the current through the Helmholtz coil, as measured by a current monitor.

Bibliography

[1] H. Alfvén. *On the Origin of the Solar System.* Oxford University Press, 1954.

[2] H. Alfvén. Collision between a nonionized gas and a magnetized plasma. *Reviews of Modern Physics*, 32(4):710–713, 1960.

[3] J. Bally et al. *Hubble Space Telescope* observations of proper motions in Herbig-Haro objects 1 and 2. *The Astrophysical Journal*, 123:2627–2657, 2002.

[4] P. M. Bellan. *Spheromaks.* Imperial College Press, 2000.

[5] P. M. Bellan. *Fundamentals of Plasma Physics.* Cambridge University Press, 2006.

[6] W. H. Bennett. Magnetically self-focussing streams. *Physical Review*, 45(12):890–897, 1934.

[7] T. Berger et al. Magneto-thermal convection in solar prominences. *Nature*, 472:197–200, 2011.

[8] R. Blandford. Quasar jets and their fields. *Philosophical Transactions of the Royal Society of London A*, 358.

[9] R. D. Blandford and D. G. Payne. Hydromagnetic flows from accretion discs and the production of radio jets. *Monthly Notices of the Royal Astronomical Society*, 199:883–903, 1982.

[10] R. D. Blandford and M. J. Rees. A 'twin-exhaust' model for double radio sources. *Monthly Notices of the Royal Astronomical Society*, 169.

[11] N. Brenning. Limits on the magnetic field strength for critical ionization velocity interaction. *Physics of Fluids*, 28(11):3424–3426, 1985.

[12] N. Brenning. Review of the CIV phenomenon. *Space Science Reviews*, 59:209–314, 1992.

[13] M. Brown. Experimental studies of magnetic reconnection. *Physics of Plasmas*, 6:1717–1724, 1999.

[14] S. Chandrasekhar. *Hydrodynamic and Hydromagnetic Stability.* Dover Publications, 1961.

[15] H. Che, J. F. Drake, and M. Swisdak. A current filamentation mechanism for breaking magnetic field lines during reconnection. *Nature*, 474:184–187, 2011.

[16] Francis F. Chen. *Introduction to plasma physics and controlled fusion.* Plenum Press, 1984.

[17] DuPont. Kapton hn technical data sheet. `http://www2.dupont.com/Kapton/en_US/assets/downloads/pdf/HN_datasheet.pdf`.

[18] J. Egedal, W. Fox, N. Katz, M. Porkolab, K. Reim, and E. Zhang. Laboratory observations of spontaneous magnetic reconnection. *Physical Review Letters*, 98:015003, 2007.

[19] A. Ferrari. Modeling extragalactic jets. *Annual Review of Astronomy and Astrophysics*, 36.

[20] W. Geckelman and R. L. Stenzel. Magnetic field line reconnection experiments: 6. Magnetic turbulence. *Journal of Geophysical Research*, 89:2715–2733, 1984.

[21] D. A. Gurnett and A. Bhattacharjee. *Introduction to plasma physics: With space and laboratory applications.* Cambridge University Press, 2005.

[22] P. Hartigan et al. Fluid dynamics of stellar jets in real time: Third epoch *Hubble Space Telescope* images of HH 1, HH 34, and HH 47. *The Astrophysical Journal*, 736:29–49, 2011.

[23] P. Hartigan, A. Frank, P. Varnière, and E. G. Blackman. Magnetic fields in stellar jets. *The Astrophysical Journal*, 661:910–918, 2007.

[24] P. Hartigan, S. Heathcote, J. A. Morse, B. Reipurth, and J. Bally. Proper motions of the HH 47 jet observed with the *Hubble Space Telescope*. *The Astrophysical Journal*, 130:2197–2205, 2005.

[25] P. Hartigan and J. Morse. Collimation, proper motions, and physical conditions in the HH 30 jet from *Hubble Space Telescope* slitless spectroscopy. *The Astrophysical Journal*, 660:426–440, 2007.

[26] J. J. Hester et al. WFPC2 studies of the Crab Nebula. III. Magnetic Rayleigh–Taylor instabilities and the origin of the filaments. *The Astrophysical Journal*, 456:225–233, 1996.

[27] R. Hippler, H. Kersten, M. Schmidt, and K. H. Schoenbach, editors. *Low Temperature Plasmas.* Wiley-VCH, 2008.

[28] S. C. Hsu and P. M. Bellan. Experimental identification of the kink instability as a poloidal flux amplification mechanism for coaxial gun spheromak formation. *Physical Review Letters*, 90(21):215002, May 2003.

[29] A. Königl and A. R. Choudhuri. Force free equilibria of magnetized jets. *The Astrophysical Journal*, 289:173–187, February 1985.

[30] P. P. Kronberg, R. V. E. Lovelace, G. Lapenta, and S. A. Colgate. Measurement of the electric current in a kpc-scale jet. *Astrophysical Journal Letters*, 741:L15, 2011.

[31] R. M. Kulsrud. *Plasma Physics for Astrophysics*. Princeton University Press, 2005.

[32] D. Kumar. *Experimental Investigations of Magnetohydrodynamic Plasma Jets*. PhD thesis, California Institute of Technology, 2009.

[33] D. Kumar and P. M. Bellan. Heterodyne interferometer with unequal path lengths. *Review of Scientific Instruments*, 77:083503, 2006.

[34] D. Kumar and P. M. Bellan. Nonequilibrium alfvénic plasma jets associated with spheromak formation. *Physical Review Letters*, 103:105003, 2009.

[35] D. Kumar, A. L. Moser, and P. M. Bellan. Energy efficiency analysis of the discharge circuit of Caltech spheromak experiment. *IEEE Transaction on Plasma Science*, 38(1):47–52, 2010.

[36] S. T. Lai. A review of critical ionization velocity. *Reviews of Geophysics*, 39(4):471–506, 2001.

[37] S. V. Lebedev, A Ciardi, D. J. Ampleford, S. N. Bland, S. C. Bott, J. P. Chittenden, G. N. Hall, J. Rapley, C. A. Jennings, A. Frank, E. G. Blackman, and T. Lery. Magnetic tower outflows from a radial wire array Z-pinch. *Monthly Notices of the Royal Astronomical Society*, 361:97–18, 2005.

[38] R. P. Lin et al. *RHESSI* observations of particle acceleration and energy release in an intense solar gamma-ray line flare. *The Astrophysical Journal*, 595:L69–L76, 2003.

[39] C. Liu et al. The eruption from a sigmoidal solar active region on 2005 May 13. *Astrophys. J.*, 669:1372–1381, 2007.

[40] M. Livio. Astrophysical jets: a phenomenological examination of acceleration and collimation. *Physics Reports*, 311.

[41] R. V. E. Lovelace. Dynamo model of double radio sources. *Nature*, 262.

[42] R. V. E. Lovelace, H. Li, A. V. Koldoba, G. V. Ustyugova, and M. M. Romanova. Poynting jets from accretion disks. *The Astrophysical Journal*, 572.

[43] R. V. E. Lovelace and M. M. Romanova. Magnetohydrodynamic origin of jets from accretion disks. In *PLASMAS IN THE LABORATORY AND IN THE UNIVERSE: New Insights and New Challenges*, 2003.

[44] D. Lynden-Bell. Magnetic jets from swirling discs. *Monthly Notices of the Royal Astronomical Society*, 369.

[45] D. Lynden-Bell. On why discs generate magnetic towers and collimate jets. *Monthly Notices of the Royal Astronomical Society*, 341.

[46] D. L. Meier, S. Koide, and Y. Uchida. Magnetohydrodynamic production of relativistic jets. *Science*, 291.

[47] G. Mellema and A. Frank. Outflow collimation in young stellar objects. *Monthly Notices of the Royal Astronomical Society*, 292.

[48] R. Mundt and J. W. Fried. Jets from young stars. *The Astrophysical Journal*, 274.

[49] J. F. O'Hanlon. *A User's Guide to Vacuum Technology.* Jon Wiley & Sons, 1980.

[50] G. Pelletier and R. E. Pudritz. Hydromagnetic disk winds in young stellar objects and active galactic nuclei. *The Astrophysical Journal*, 394.

[51] R. E. Pudritz. Jets from accretion discs. *Philosophical Transactions of the Royal Society of London A*, 358.

[52] M. A. Raadu. The role of electrostatic instabilities in the critical ionization velocity mechanism. *Astrophysics and Space Science*, 55:125–138, 1978.

[53] B. Reipurth and J. Bally. Herbig-Haro flows: Probes of early stellar evolution. *Annual Review of Astronomy and Astrophysics*, 39.

[54] B. Reipurth, S. Heathcote, J. Morse, P. Hartigan, and J. Bally. *Hubble Space Telescope* images of the HH 34 jet and bow shock: Structure and proper motions. *The Astrophysical Journal*, 123:362–381, 2002.

[55] C. A. Romero-Talamás. *Investigations of Spheromak plasma dynamics: High-speed imaging at the Sustained Spheromak Physics Experiment and magnetic diagnostics at the Caltech Spheromak experiment.* PhD thesis, California Institute of Technology, 2005.

[56] C. A. Romero-Talamaś, P. M. Bellan, and S. C. Hsu. Multielement magnetic probe using commercial chip inductors. *Review of Scientific Instruments*, 75(8):2664–2667, 2004.

[57] D. D. Ryutov, R. P. Drake, and B. A. Remington. Criteria for scaled laboratory simulations of astrophysical MHD phenomena. *The Astrophysical Journal Supplement Series*, 127:465–468, April 2000.

[58] Franz Sauer. A ballistic pendulum to measure plasma jet momentum on the Caltech spheromak formation/astrophysical jet experiment. Technical report, California Institute of Technology, Summer Undergraduate Research Fellowship final technical paper, 2009.

[59] J. C. Sherman. Review of the critical velocity of gas-plasma interaction, II. Theory. *Astrophysics and Space Science*, 24.

[60] K. Shibata and S. Tanuma. Plasmoid-induced-reconnection and fractal reconnection. *Earth Planets Space*, 53:473–482, 2001.

[61] U. Shumlak et al. Equilibrium, flow shear and stability measurements in the Z-pinch. *Nuclear Fusion*, 49:075039, 2009.

[62] A. Siemiginowska et al. *CHANDRA* discovery of a 300 kiloparsec X-ray jet in the gigahertz-peaked spectrum quasar PKS 1127–145. *The Astrophysical Journal*, 570.

[63] A. K. Srivastava, T. V. Zaqarashvili, P. Kumar, and M. L. Khoachenko. Observation of kink instability during small B5.0 solar flare on 2007 June 4. *The Astrophysics Journal*, 715:292–299, 2010.

[64] X. Z. Tang. Self-organization of radio lobe magnetic fields by driven relaxation. *The Astrophysical Journal*, 679:1000–1017, 2008.

[65] M. Yamada, R. Kulsrud, and H. Ji. Magnetic reconnection. *Reviews of Modern Physics*, 82:603–664, 2010.

[66] G. S. Yun. *Dynamics of Plasma Structures Interacting with External and Self-Generated Magnetic Fields*. PhD thesis, California Institute of Technology, 2007.

[67] G. P. Zhou et al. Two successive coronal mass ejections driven by the kink and drainage instabilities of an eruptive prominence. *The Astrophysics Journal*, 651:1238–1244, 2006.